École doctorale « Ondes & Matière » n° 288

THESE DE DOCTORAT

présentée par

Anton Leontyev

pour l'obtention du

GRADE DE DOCTEUR DE L'UNIVERSITE PARIS SUD XI EN PHYSIQUE

Specialité: Sciences physiques

Laser decontamination and cleaning of metal surfaces: modelling and experimental studies.

---

date prévue de soutenance le 8 novembre 2011

M. Alain SARFATI	Président du jury
M. Philippe DELAPORTE	Rapporteur
Mme Tatiana ITINA	Rapporteur
M. Christian GRISOLIA	Examinateur
M. Edward MANYKIN	Membre invité
M. Stephane SARRADE	Examinateur
M. Alexandre SEMEROK	Directeur de thèse

Thèse préparé au Commissariat à l'Énergie Atomique et aux Énergies Alternatives
Direction de l'Énergie Nucléaire – Centre de Saclay

Abstract

Metal surface cleaning is highly required in different fields of modern industry. Nuclear industry seeks for new methods for oxidized surface decontamination, and thermonuclear installations require the cleaning of plasma facing components from tritium-containing deposited layer. The laser ablation is proposed as an effective and safe method for metal surface cleaning and decontamination. The important factor influencing the laser heating and ablation is the in-depth distribution of laser radiation. The model of light propagation in a scattering layer on a metal substrate is developed and applied to analyse the features of light distribution. To simulate the contaminated surfaces, the stainless steel AISI 304L was oxidized by laser and in a furnace. Radioactive contamination of the oxide layer was simulated by introducing europium and/or sodium. The decontamination factor of more than 300 was demonstrated with found optimal cleaning regime. The decreasing of the corrosion resistance was found after laser cleaning. The ablation thresholds of ITER-like surfaces were measured. The cleaning productivity of 0.07 m^2/hour·W was found. For mirror surfaces, the damage thresholds were determined to avoid damage during laser cleaning. The possibility to restore reflectivity after thin carbon layer deposition was demonstrated. The perspectives of further development of laser cleaning are discussed.

Keywords: decontamination, cleaning, laser ablation, fiber laser, metal, stainless steel, oxide layer, tungsten, carbon, four-flux model, ITER, tokamak, deposited layer, diagnostic mirror, plasma-facing components

Résumé

Le nettoyage des surfaces métalliques est nécessaire dans différents domaines de l'industrie moderne. L'industrie nucléaire cherche de nouvelles méthodes de décontamination des surfaces oxydées, et les installations thermonucléaires nécessitent le nettoyage des composants face au plasma pour enlever la couche déposée contenant tritium. L'ablation laser est proposée comme une méthode efficace et sûre pour le nettoyage des surfaces métalliques et leur décontamination. Le facteur important influençant le chauffage et l'ablation laser est la distribution en profondeur de l'intensité laser. Le modèle de propagation de la lumière dans une couche diffusant sur un substrat métallique est développé et appliqué pour analyser les caractéristiques de distribution de lumière. Pour simuler les surfaces contaminées, l'inox AISI 304L a été oxydé par laser et chauffé dans un four. La contamination radioactive de la couche d'oxyde a été simulée par l'introduction d'europium et / ou de sodium. Un facteur de décontamination de plus de 300 a été démontré avec le régime de nettoyage optimal trouvé. Une diminution de la résistance à la corrosion a aussi été montrée après un nettoyage laser. Les seuils d'ablation des surfaces ITER-like (représentatives d'ITER) ont été mesurés. Une vitesse de nettoyage de 0,07 m^2/W·h a été trouvée. Pour les surfaces miroir, les seuils de dommages étaient déterminés pour éviter les dommages lors du nettoyage au laser. La possibilité de restaurer la réflectivité après le dépôt d'une couche mince de carbone a été démontrée. Les perspectives de développement ultérieur de nettoyage laser sont discutées.

Mots clés: décontamination, nettoyage, ablation laser, laser à fibre, métal, inox, couche d'oxyde, tungstène, carbone, modèle à quatre flux, ITER, tokamak, couche déposée, miroir diagnostic, composants face au plasma

Résumé de thèse

Introduction

La plupart des centrales nucleaire actuellement utilisées ont été construits en années 1960 – 1970. A l'heure actuelle, ils ont atteint leurs limites de service et doivent subir le déclassement. Après l'arrêt de ces réacteurs et avant leur démantèlement, les réacteurs sont maintenus inactifs depuis plusieurs années. Durant cette période, tous les radionucléides à courte période se divisent et la radioactivité résiduelle est causée par la présence de cobalt-60. Pour réduire la quantité de déchets radioactifs et l'exposition du personnel globale et aussi que pour séparer les matériaux réutilisables et des déchets ultimes, la décontamination est réalisée.

Dans les réacteurs nucléaires refroidi par l'eau, la partie principale de la contamination radioactive se forme lorsque les produits de corrosion sont libérés des matériaux du circuit primaire, transporté dans le cœur des et activé pour devenir radioactifs. Une partie de ces produits de corrosion se dépose sur la surface oxydée de tubes de recirculation et d'autres composants. En conséquence, la contamination est principalement concentrée dans la couche d'oxyde sur une surface de composants métalliques.

Les principaux radionucléides qui contribuent au champ de rayonnement dans le circuit primaire sont ^{60}Co, ^{58}Co, ^{51}Cr, ^{54}Mn, ^{59}Fe et ^{110m}Ag. Parmi ces derniers, ^{60}Co est d'une importance particulière en raison de sa quantité prédominante, sa demi-vie longue (plus de 7 ans) et la production des γ**-photons à haute énergie.**

Les objectifs de la thèse peuvent être résumés comme suit:

- la modélisation du chauffage laser de surface métallique avec une couche;
- développement et l'application des équipements expérimentaux pour des études sur le chauffage laser de surface et de nettoyage par ablation laser;
- détermination du seuil d'ablation pour des surfaces de métaux différents (couche d'oxyde sur l'acier inoxydable, ITER comme des échantillons, de Mo-miroir);
- études expérimentales sur l'efficacité d'ablation laser (facteur de décontamination, le taux d'ablation, endommagement de substrat métallique) pour le nettoyage des surfaces métalliques avec une couche contaminée;
- nettoyage des miroirs diagnostiques d'ITER pour reconstruire leur réflectivité initiale.

Modèles de chauffage laser des surfaces métalliques

Pour le nettoyage au laser de miroirs métalliques (molybdène et des miroirs en acier inoxydable), il est nécessaire de choisir les paramètres laser pour éviter des dommages irréversibles sur la surface du miroir. Ainsi, dans la première partie de ce chapitre, nous considérons l'interaction de l'impulsion laser gaussien avec un substrat métallique.

Les expressions pour la température de chauffage laser sur la surface au centre du faisceau laser ont été trouvées. Nous présentons le modèle pour calculer le seuil d'endommagement pour les métaux. Dans les calculs, nous supposons que le dommage se produit à la fluence lorsque la température maximale due au chauffage laser atteint le point de fusion.

Ensuite, le chauffage laser d'un substrat avec une couche est considéré. Les équations de conduction de la chaleur dans la couche et du substrat sont correctement adimensionnées et la température de chauffage est obtenu pour la distribution arbitraire de sources de chauffage. Cette solution générale tient compte de l'imperfection de contact thermique entre la couche et le substrat ainsi que l'échange de chaleur à la surface de la couche. Plusieurs cas limite, comme le chauffage par des impulsions Dirac et le chauffage par un laser continu, sont considérés.

Comme couches déposées dans tokamaks et les couches d'oxyde formées dans les installations nucléaires ne sont pas homogènes, l'interférence du faisceau laser et de diffusion dans la couche doit être envisagée. Pour calculer la distribution des sources de chaleur pour les surfaces complexes avec des couches semi-transparentes inhomogène, un modèle théorique pour la propagation de la lumière dans la couche a été développé. Le modèle est basé sur le transfert de la lumière de quatre flux et prend en compte les interférences, l'absorption et la diffusion de la lumière laser cohérente dans la couche.

Le code de calcul a été écrit pour résoudre le BVP numériquement en utilisant la méthode des différences finies. Le modèle a été validé en comparant ses résultats avec ceux obtenus par les modèles développés précédemment au CEA de Saclay, qui décrivent les cas limites des approximations cohérentes et 3-flux.

Ainsi, avec ce modèle développé, il devient possible de calculer la répartition des sources de chaleur et des températures en profondeur de la couche.

Etudes expérimentales

Deux installation lasers sont utilisées dans notre étude: le système DetriLaser pour l'ablation laser et une installation de mesure de température pour les études de chauffage laser.

Le système DetriLaser comprend un laser à fibre pulsé ytterbium (IPG YLP-1/120/20), une tete galvanométrique (Scanlab SCANcube 10) et une lentille de focalisation (Linos F-

Theta Ronar, λ = 1064 nm, f = 420 mm) . L'air aspiré est filtré par PUREX LASEREX 400iPVC pompe. L'installation a été correctement ajusté et le profil de faisceau laser a été mesurée avec la caméra CCD Pulnix TM-6AS et le système d'acquisition SPIRICON pour différentes puissances laser.

L'installation de mesure de température se compose de porteur d'échantillon avec chauffage électrique, une unité de contrôle de température, une laser à fibre IPG YLR-100, une photodiode rapide et pyromètre Kleiber KGA 740-LO avec un temps de réponse (t_{95}) de 6 ms. Le pyromètre a été étalonné en utilisant la source de rayonnement du corps noir. Pour éliminer l'influence du rayonnement laser réfléchi sur le détecteur, un filtre optique est utilisé.

Les profils de la surface avant et après le traitement au laser ont été mesurées avec le profilomètre optique MicroXAM 100 basée sur l'interféromètre Mirau et le profilomètre mécaniques Mahr. Les profils 2D ont été traités en utilisant le logiciel Gwyddion.

Pour effectuer les mesures d'épaisseur de couche pour échantillons « ITER-like », ils ont été coupés, incorporé dans une résine et polies mécaniquement avec papier 4000 SiC (2,5 μm taille de particule médiane) et ensuite avec des chiffons de polissage. Après le polissage, coupe de l'échantillon ont été analysés avec un microscope électronique à balayage.

La réflectivité de miroirs métalliques soumis à un nettoyage laser est contrôlé par un spectromètre. Un accessoire spécial est utilisé pour permettre des mesures de coefficient de réflexion à 10° d'angle d'incidence. Spectres obtenus avec le spectromètre donnent l'information sur la restauration du coefficient de réflexion dans la gamme de longueur d'onde de 250 à 2500 μm. Avec le spectromètre, qui ne mesure que le coefficient de réflexion spéculaire, un montage basé sur la sphère intégrante est appliquée pour mesurer le coefficient de réflexion totale d'une surface sous d'intérêt à 543,5 nm et 1064 longueurs d'onde.

Pour mesurer l'ablation et le seuil d'endommagement un soi-disant technique « papier brûlé » a été utilisée. Avec cette méthode, le seuil peut être déterminé à partir des mesure de diamètres de taches / cratères formés après l'action des impulsions laser d'énergie différente avec le profil gaussien spatiale. Pour bien mesurer les températures de chauffage au laser, une procédure permettant de trouver l'émissivité d'échantillon inconnue a été appliquée.

Résultats expérimentales

Décontamination des surfaces oxydées

Décontamination par ablation laser des surfaces métalliques oxydées (en acier inox AISI 304L échantillons) a été étudiée.

L'oxydation de l'acier inoxydable par chauffage laser et dans un four à 1273 K dans l'air a été appliquée. De ces expériences, nous pouvons conclure que l'épaisseur de la couche d'oxyde ne pas augmenter fortement avec le nombre effectif des impulsions laser, mais augmente avec la fluence mono-impulsion. Avec technique d'oxydation par laser on peut obtenir des couches d'oxyde d'épaisseur (profondeur où la concentration atomique de l'oxygène tombe presque à zéro) jusqu'à ~3 – 4 μm. En four l'oxygène pénètre jusqu'à ~ 10 μm. Les couches formées dans un four ont été choisis pour des investigations.

Différents régimes de balayage ont été testés pour trouver un régime optimal pour le nettoyage laser. Le régime de balayage suivante a été choisie: $\Delta x = 100$ μm, $\Delta y = 25$ μm, $v_x = 2000$ mm/s. Pour ce régime, il a été constaté que la fluence laser haute ~10 J/cm^2 donne la meilleur efficacité de nettoyage. Pour la couche d'oxyde formée dans le four, le taux d'ablation est égale à ~ 1,2 μm/pass et pour la couche d'oxyde formée par le laser, elle est égale à ~ 3 μm/pass.

Le artificiellement contaminés avec l'Eu et de l'échantillon oxydé Na ont été préparés en plongeant dans la solution d'eau de $Eu(NO_3)_3$ ou de NaCl pendant 24 heures. Le montant total d'europium a été déterminé avec la méthode d'attaque chimique et égale à 32 g/cm^2 ($1{,}26 \cdot 10^{17}$ atomes/cm^{-2}) avant des tests de nettoyage. Les essais de nettoyage ont été effectués en utilisant le régime de balayage choisi avec 10 passes de nettoyage (372 J/cm^2 de fluence déposé au total), ce qui correspond à la profondeur d'ablation ~ 6 μm. Après le nettoyage, la concentration d'europium est tombée en dessous du seuil de mesure (<0,1 g/cm^2) qui correspond au facteur de décontamination (concentration de contaminant avant et après nettoyage) de plus que 300 pour l'échantillon contaminé par Eu. Pour l'échantillon contaminé par Na, facteur de décontamination a été DF = 1500 après le dépôt de 186 J/cm^2. Ces facteurs de décontamination sont considérés comme suffisants pour nettoyer les déchets radioactifs.

Régime de nettoyage utilisé correspond à la productivité du nettoyage egale à ~ 0.001 m^2/heure×W. Ainsi, avec le laser à fibre de 1 kW puissance moyenne, 1 m^2 de surface contaminée peut être nettoyée en 1 heure.

Il a été constaté que, après nettoyage au laser, la résistance à la corrosion de la surface de l'acier inoxydable avait considérablement dégradée. Cela est arrivé parce que plusieurs micromètres en profondeur de la surface métallique est devenue appauvri en chrome à cause de l'oxydation et le nettoyage au laser.

L'ablation laser et le chauffage laser d'échantillons ITER-like

Dans cette section, on étudie l'ablation laser et chauffage laser d'échantillons ITER-like, qui ressemblent des surfaces face au plasma de future installation ITER. Echantillons ITER-like constituent d'un substrat métallique (généralement en acier inoxydable ou en tungstène) et d'une couche déposée. Couche déposée peut contenir de tungstène, de

béryllium, d'hydrogène et de carbone dans la phase amorphe (DLC, diamond-like carbon). Dans nos études de deux échantillons a été utilisée:

- SS/W/W+DLC(H). La couche de tungstène et DLC avec la concentration d'hydrogène sur le substrat en AISI 304 acier inoxydable avec la couche de marquage en W de 10 nm d'épaisseur. Epaisseur de couche: 1,5 – 2 μm. L'épaisseur du substrat: 10 mm. Diamètre d'échantillon: 45 mm.
- W/W+αCH. La couche séquentiellement déposé, composée de tungstène et de carbone amorphe. Epaisseur de couche: 1 – 2 μm (selon la zone).

Les tests d'ablation ont été effectués avec le premier échantillon. Il a été montré que, à faibles fluences, la couche contenant du carbone se déforme mécaniquement en raison des contraintes thermomécaniques induites par chauffage laser rapide. Aux fluences $F > 2$ J/cm^2, la couche commence à s'ablater. Cet effet peut être utilisé pour enlever la couche sans sa destruction.

Pour l'échantillon W/W+αCH, il était possible d'enlever la couche par une seule impulsion laser. Le seuil d'ablation de la couche sur échantillon W/W+αCH est seulement 0,27 ± 0,03 J/cm^2. Et à 1,33 ± 0,19 J/cm2 l'enlèvement complète de la couche déposée commence. Après détermination des seuils, les tests de nettoyage ont été effectués avec cet échantillon, qui montrent les productivités du nettoyage jusqu'à 0.071 m^2/heure par W de puissance de laser.

Toutefois, si la couche ne contient pas de carbone, mais seulement un métal (tungstène, l'aluminium) avec un peu d'hydrogène / deutérium, son seuil d'ablation augmente grâce à la haute réflectivité de la couche. Ces couches, en particulier en tungstène, ne peut être enlevée par ablation laser sans endommager/ablater le substrat. La méthode de détritiation par chauffage laser peut être appliqué dans ce cas.

Les températures de chauffage laser d'échantillons ITER-like ont été mesurés. La comparaison des températures de chauffage mesurées expérimentalement avec ceux qui étaient obtenues théoriquement est effectuée pour la validation du modèle de chauffage laser.

Nettoyage de miroirs métalliques

Essais de nettoyage ont été effectués avec des miroirs en molybdène polycristallin et en acier inoxydable. La rugosité initiale et le coefficient de réflexion spectrale des miroirs ont été mesurés.

Dans un premier temps, la détermination des seules d'emdommagement mono-impulsion et multi-impulsions de miroirs vierges a été effectuée. Ils ont été comparés avec des seuils d'endommagement théoriques obtenus avec les modèles présentés plus haut et avec d'autres résultats expérimentaux. On a constaté que sous l'action de plusieurs impulsions laser, la «bosse» de hauteur ~ 4 – 5 μm est formée sur la surface du miroir Mo.

Cela confirme le modèle d'accumulation des déformations plastiques lors d'un dommage laser multi-impulsions des métaux.

Ces résultats ont démontré que des seules d'emdommagement mono-impulsion et multi-impulsions peut être prédit assez précisément si les variations de réflectivité avec la température et l'accumulation de déformation plastique sont pris en compte dans le modèle.

Puis l'oxydation de la surface après plusieurs impulsions a été étudiée en utilisant l'analyse EDX. Pas d'oxygène supplémentaire a été trouvé à la «bosse» formée sur la surface du miroir Mo. Cependant, l'oxydation forte se produit lorsque faisceau laser balaye la surface.

Les tests d'endommagement ont été répétées dans une atmosphère d'argon. Pour cela, le miroir a été mis en place dans une cellule cylindrique remplie d'Ar. Les fenêtres de la cellule ont un revêtement dialectique de haute transmission à la longueur d'onde de laser λ = 1064 nm. L'absence totale d'oxydation a été trouvé en ce cas. Ainsi, l'oxydation de l'échantillon peut être supprimée en effectuant un traitement dans une atmosphère inerte.

Pour les test de nettoyage, la couche de carbone a été déposé sur la surface polie du miroir Mo en utilisant un évaporateur de carbone Technologies Quorum Q150R ES. L'épaisseur moyenne du revêtement d = 31 ± 1 nm a été déterminée avec un profilomètre mécanique en analysant les bords de la zone revêtue. Le coefficient de réflexion totale du miroir avec une couche de carbone a été trouvé comme R_p = 0,29 ± 0,02 à 1064 nm.

Régimes de nettoyage différentes ont été testées afin de déterminer un régime optimal avec le meilleur efficacité d'ablation, mais sans dommage de miroir. Dans ces tests, la fluence laser a été choisie pour être inférieure ou égale au seuil d'endommagement du miroir. Un régime de nettoyage optimale a été déterminée: la fluence F = 7 J/cm^2, les pas $\Delta x = \Delta y$ = 50 μm. La réflectivité miroir a été restaurée à plus de 90% de sa valeur initiale pour les longueurs d'onde λ > 800 nm. Dans le spectre visible, la restitution a été de 60 - 80%.

Cependant, les dommages du substrat s'est déroulée dans une forme de petits défauts (quelques micromètres de diamètre) qui pourrait être attribuée à la nature polycristalline d'échantillons. Ainsi, pour éviter des dommages irréversibles sur la surface du miroir, les paramètres du laser appropriés doivent être choisis pour le nettoyage laser.

Ainsi, des études théoriques et expérimentales sur le nettoyage laser des surfaces métalliques ont démontré la possibilité de nettoyer les surfaces miroir sans leurs endommagement.

Études complémentaires et perspectives

Afin de poursuivre le développement de cette application, on donne ici les perspectives de travail qui pourraient être envisagées :

- Les tests de nettoyage laser sur un miroir de molybdène monocristallin doit être fait pour élucider la nature des défauts qui apparaissent sur le miroir après le nettoyage laser.
- Pour améliorer encore le modèle de propagation de la lumière dans une couche inhomogène, la rugosité des bords doit être prise en compte. Si la source ne peut pas être considéré comme monochromatique, puis l'intégration sur toutes les longueurs d'onde doit être faite.
- L'effet de la décontamination sur résistance à la corrosion est très important pour les substrats en acier inoxydable. Si l'on connaît certaines fonctionnalités de nettoyage au laser qui offrent une résistance à la corrosion sans détérioration affecte indésirables, le nettoyage au laser pourrait offrir un avantage supplémentaire pour son application. Par ailleurs, les expériences avec de vrais échantillons oxydés sont nécessaires pour étudier la possibilité d'éviter les changements de surface indésirables résultant de l'oxydation artificielle, qui peut être trop importante.

Acknowledgements

This thesis would not have been accomplished without the encouragement, advice and assistance of a number of people.

First and foremost, I thank my scientific supervisor, Alexandre Semerok, who gave me the opportunity to work on this theme. I appreciate his intensive support and excellent guidance and mentorship. In the past years, through countless discussions, he helped me to become more productive and more self-confident in my work. I believe that my growth as a scientist is due much in part to him, and I hope that his level of professionalism will continue to influence me for years to come. I sincerely thank him for being a wonderful mentor and a friend.

I owe thanks to Pierre-Yves Thro who helped me in scientific and everyday life. I am grateful to Daniel Farcage for the help in all that concerns laboratory equipment. Special thanks to Michel Tabarant for his sincere interest in the theme of this work that allow me to perform a lot of experiments on oxidized steel. I esteem the work of Cecile Blanc who helped me with SEM and EDS analysis.

I would like to thank specially Pacquentin Wilfried. He taught me the polishing techniques and the corrosion tests methodology. And I'm thankful to people at SCCME – Jérôme Canel, Leonel Sejourné and Daniel Besnard for assisting with sample oxidation in the furnace. I also thank Peycelon Hugues, Faure Sylvain and Causse Jérémy from LPAD, CEA Marcoule for the discussion of methods, problems and prospects of nuclear decontamination. This is by no means a complete list of contributors, but I have tried to acknowledge those who were most instrumental in helping with my dissertation research.

I would like to thank all the people I met at SCP during the past few years, they are providing a great environment and it is a pleasure to work with them.

The ultimate thank goes to my wife Polina to whom I dedicate this thesis for her care and belief in me. She walked the journey by my side and my experience was greatly enriched by her presence.

Contents

Chapter 1. Introduction

Contents

At present, many industries and technological processes face a rapid breakthrough which is accompanied by a growing demand in energy sources. To satisfy the growing demand in energy, modern technologies are under constant study, development and improvement. As the natural sources of energy are quite limited with time, nuclear industry may be regarded as practically unlimited source of energy for the future.

1.1 Nuclear reactors

Figure 1 presents a general scheme of a pressurised water reactor. Most of the power plants were constructed in 1960-1970s. At present, they have reached their service life limits and should undergo decommissioning. After the shutdown of these reactors and before decommissioning, the reactors are kept inactive for several years. During this period, all short-living radionuclides decay and the residual radioactivity is caused by the presence of cobalt-60 isotope.

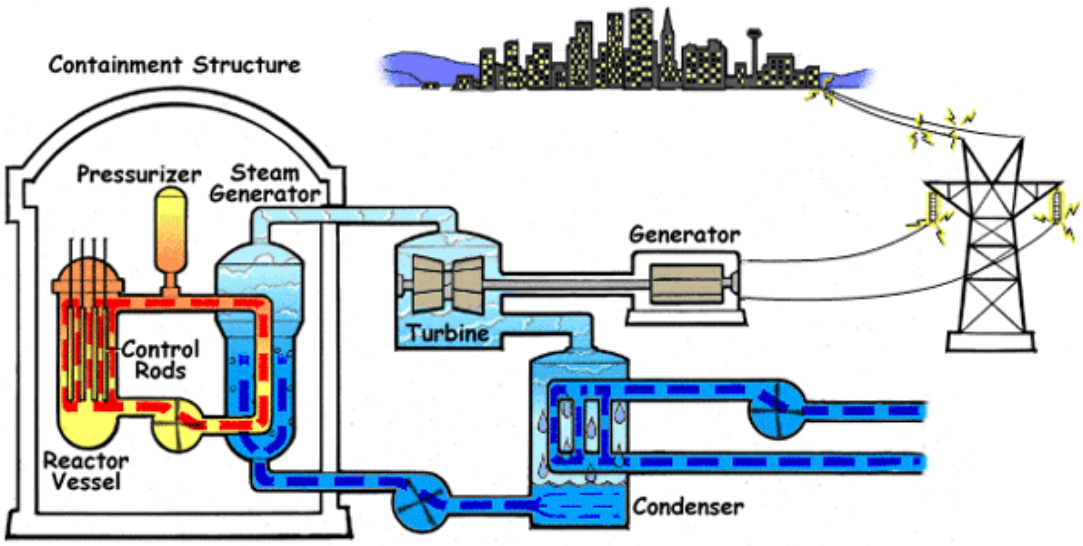

Figure 1: Scheme of a Pressurized Water Reactor.

During decommissioning, the reactor is dismantled and all contaminated metal components, many of which are made of high-quality steels and alloys, are treated as radioactive wastes and transported to the temporary repositories to be disposed sometime later into the permanent geological repositories.

To reduce the amount of radioactive wastes and overall personnel exposure and also to separate the reusable materials from ultimate wastes, decontamination is performed.

In water cooled nuclear reactors, the main part of radioactive contamination is formed when corrosion products are released from primary structural materials, transported to in-core regions and activated to become radioactive [1]. A part of these corrosion products is deposited on the oxidized surface of recirculation pipes and other components. As a result, a surface dose rate is increasing and the contamination is concentrated mainly in the oxide layer on a surface of metallic components.

The main radionuclides which contribute to the radiation field in primary side coolant are ^{60}Co, ^{58}Co, ^{51}Cr, ^{54}Mn, ^{59}Fe, and ^{110m}Ag. Among these, ^{60}Co is of a special importance due to its predominant amount, long half-life period (more than 7 years) [2] and high energy γ-photons. Cobalt formation and accumulation on different surfaces were under study in [3], [4].

1.1.1 Problem of metals contamination

For water-cooled reactors, stainless steel AISI 304L is used as the most common pipe construction material. For efficient decontamination, one should know the structure and properties of the oxide layer. In [5], [6], a comprehensive analysis of morphology, corrosion rate, structure and composition of the oxide layer formed on the heat exchanger tubes of steam generators of VVER-type nuclear reactors were performed with 22 austenitic stainless steel specimens (type: 08X18H10T "GOST 5632-61" which correspond to AISI 321 and DIN 1.4541) originating from different steam generators. Some specimens have been previously decontaminated by AP-CITROX technique (AP: alkaline permanganate, CITROX: citric and oxalic acids [7]), while the other ones were not.

Scanning Electron Microscope (SEM) images of different oxide surfaces are shown in **Figure 2**. One can see the deposits of large crystals (up to about 10 μm) on the oxide surface of the specimens which have never been decontaminated (**Figures 2a** and **2b**). In contrast, on the surface of the specimens which have been previously decontaminated, no crystal deposits but only cracks are observed (**Figures 2c** and **2d**). The presence of crystal deposits was also revealed in [8], [9].

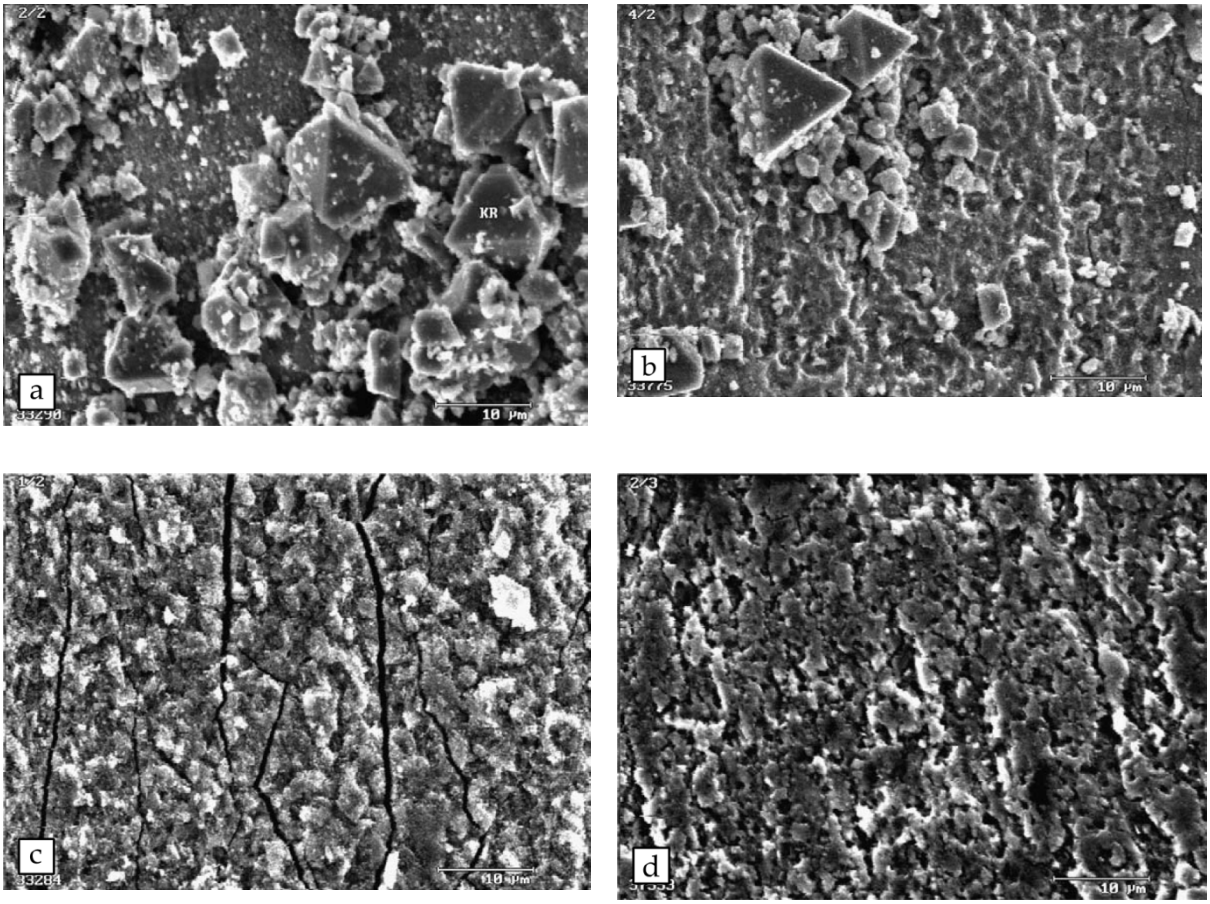

Figure 2: SEM images of oxide layer formed on the surface of steam generator tubes [5]

Conversion Electron Mössbauer Spectroscopy analysis revealed the presence of lepidocrocite (γ-FeOOH), amorphous iron (III)-hydroxide ($Fe(OH)_3$), magnetite (Fe_3O_4) and hematite (Fe_2O_3) in the oxide film.

It was also revealed that corrosion rates measured at the decontaminated samples have been subjected to conventional chemical cleaning are notably higher and the oxide layer grown on their inner surfaces is thicker. Thus, following chemical cleaning of surface, it becomes less resistant.

The structure of the oxide layer formed under normal operating conditions on the surface of stainless steel is shown in **Figure 3**. This layer consists of two sub-layers: the inner dense layer of Cr and Ni rich phase and the porous outer onr with amorphous $Fe(OH)_3$ and/or FeOOH, crystalline deposits of magnetite and hematite.

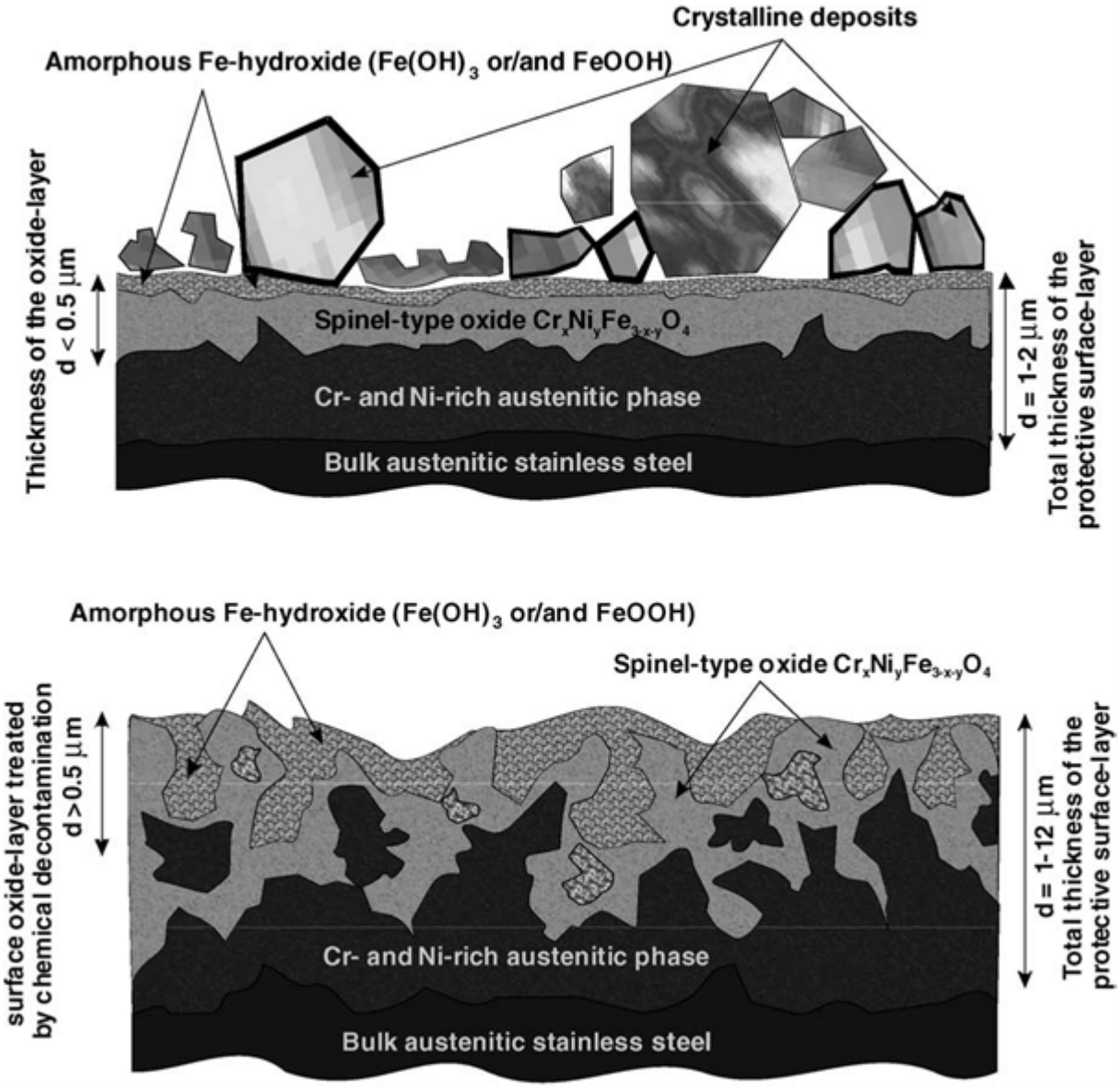

Figure 3: Structure of the oxide layer on the stainless steel: top - not decontaminated; bottom - subjected to chemical decontamination [6]

The process of formation of such layers can be described as follows. Under normal operating conditions (high pressure and temperature, reductive water chemistry) of the primary circuit of VVER-type reactors, the thermodynamically less stable alloying elements (mainly, Fe) are dissolved into the primary coolant and partially form a more or less stable oxide layer (mainly, magnetite and hematite) at the outermost surface. As a result of the selective dissolution, the bulk steel within the range of few microns becomes Fe-depleted and, consequently, Cr- and Ni-enriched. Cr- and Ni-enrichments are applied not only to the austenitic phase, but also to the magnetite. Thus, the mixed spinel-type oxides formation is considered as predominant in protective surface films.

To determine in-depth distribution of cobalt on the artificially contaminated samples, the experimental study was made in [3]. In this study, the exposure test was made on type 304 stainless steel samples placed in high-temperature and high-pressure experimental loop with demineralised water with below 5 ppb of dissolved oxygen content at 561 K and with 3 ppb non-radioactive cobalt. The corrosion film of the samples after 1000-hour exposure was analysed with Electron Probe MicroAnalysis (EPMA), X-Ray Diffraction (XRD), X-ray Photoelectron Spectroscopy (XPS) and Glow Discharge Spectroscopy (GDS) methods.

The element distributions obtained by GDS are shown in **Figure 4**. From this figure, one can see that the corrosion film consists of two layers: the outer one with a higher content of iron and the inner one with a higher content of chromium. The most content of cobalt is in the outer layer. This means that the removal of the thick outer layer of the oxide film will result in significant decrease in the surface contamination.

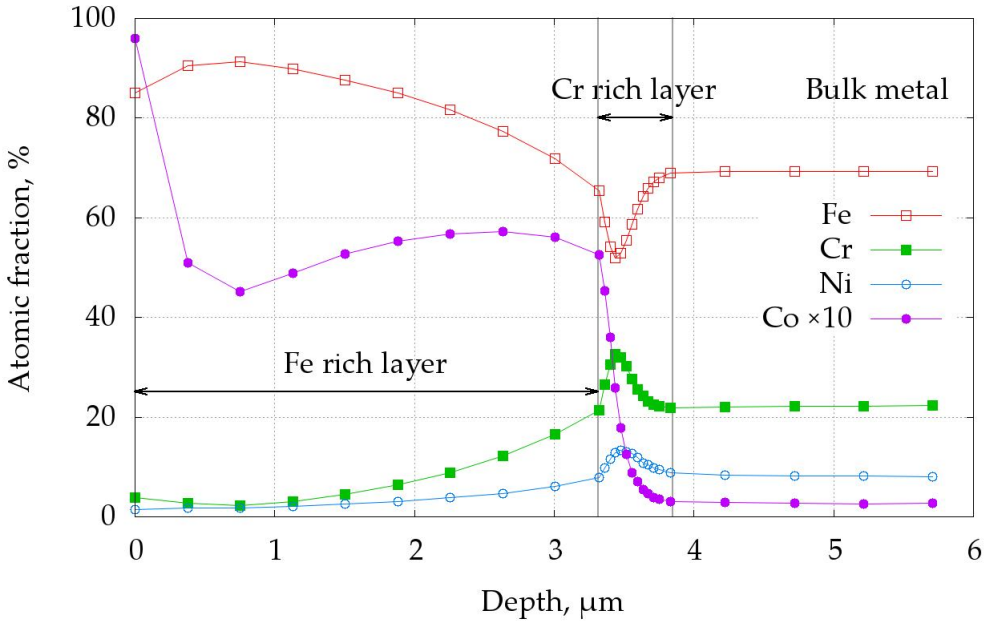

Figure 4: The elements distribution in the oxide film on type 304 stainless steel [3]

1.1.2 Decontamination techniques

At present, a number of cleaning and decontamination methods may be applied in nuclear industry. Wiping/dusting and flushing with water may be mentioned as conventional decontamination methods. Wet techniques, such as steam cleaning, wet abrasive cleaning, wet ultrasonic cleaning and chemical cleaning are also applied

despite the production of secondary liquid wastes, which are seen as a main disadvantage of these methods. Moreover, chemical cleaning is known to reduce corrosion resistance of stainless steel constructions [5], thus making this method not suitable for maintenance decontamination.

Different blasting methods (grit, sand, sponge and CO_2 blasting techniques) may be mentioned among the most applied techniques, though a large amount of secondary wastes is also seen as disadvantage. In addition, grinding and vacuuming methods are very labour-consuming and additional care should be taken to avoid unsafe exposure for personnel.

Decontamination by gels and foams has been under study in [10], [11]. The liquid phase of the decontamination foams makes not more than 10% of the total foam volume, thus decreasing the amount of chemicals required for decontamination and of the secondary wastes volume. In addition, as the foam penetrates the given volume of the contaminated devices quite well, it is easier to decontaminate some hard-to-reach parts. For gel-decontamination, the gel is applied on the contaminated surface where it reacts with the surface and absorbs contamination. When the gel is dried up, it is aspirated away. Some methods with combined application of gels and laser treatment are presented in [12].

The detailed description of these and some other decontamination techniques with the analysis of their advantages and disadvantages is presented in [13].

For nuclear industry, decontamination technique should be provided with some additional and important considerations of nuclear safety. Firstly, it should be a dry method to avoid any liquid resulting from decontamination procedure. If not, the resulting liquid should be treated as secondary radioactive waste, thus making liquid radioactive waste treatment as an additional difficult and costly problem. Automation of nuclear decontamination is seen as the second consideration. This requirement is needed to minimise the personal exposure to dangerous nuclear radiation. In certain cases, decontamination technique should not affect or change in this or that way the surface under cleaning, especially if it may result in material degradation. This may be the case of operational decontamination of nuclear power plants and the cleaning of nuclear containers which should be constantly leak-proof under possible aggressive environmental conditions. Cleaning efficiency (measured in terms of decontamination factor DF which is the ratio of initial/residual activity) should also be considered in choosing the appropriate and suitable decontamination method.

1.2 Thermonuclear reactors

The problem of exhaustion of available mineral resources, the growing concern about the ecological pollution resulted from the burning of fossil fuels and possible nuclear power plant accidents have attracted worldwide attention to the alternative sources of energy, such as solar and wind energy and modern nuclear fusion reactors (tokamaks). At present, the International Thermonuclear Experimental Reactor (ITER), which is the next-generation experimental nuclear fusion reactor, is under construction at Cadarache (France) by the international joint efforts of different teams from the European Union, India, Japan, People's Republic of China, Russia, South Korea, and the United States. The current ITER design includes Be main chamber wall and tungsten divertor.

The main principle of nuclear fusion reactor (or thermonuclear reactor) is as follows. The reactor consists of a toroidal chamber where hot plasma of hydrogen and helium isotopes is confined by means of axial magnetic field (see **Figure 5**). This chamber is referred to as «tokamak», which is a Russian acronym for "toroidal chamber with magnetic coils". When the plasma is heated enough, two nuclei can overcome substantial energy barrier arising from the mutual repulsion due to the positive charges of the nuclei which then join together to form a heavier nuclei. This is a so-called «fusion reaction».

The lower the nuclei charge is, the less kinetic energy is necessary to overcome the Coulomb barrier and initiate the reaction. Therefore, the hydrogen isotopes are used to initiate fusion reaction. The $^{2}D - ^{3}T$ reaction has the highest cross-section among all reactions with hydrogen isotopes. Thus, tritium (radioactive isotope of hydrogen) is used as « fuel » in thermonuclear reactors.

The fusion reaction between hydrogen isotopes is always accompanied by the release of high-energy neutrons. The neutrons are not affected by the magnetic field and they leave plasma volume. Then, the energy carried by the neutrons can be transformed into electric energy.

However, it is not possible to completely confine plasma and there is always a particle flux striking the wall of a chamber. This flux results in the erosion/deposition of material on the surface of chamber walls. As plasma contains tritium, it is trapped into the deposited layer. Thus, the problems of nuclear control and, consequently, nuclear decontamination and safety should be regarded as being of a highest priority and importance and should be under special consideration.

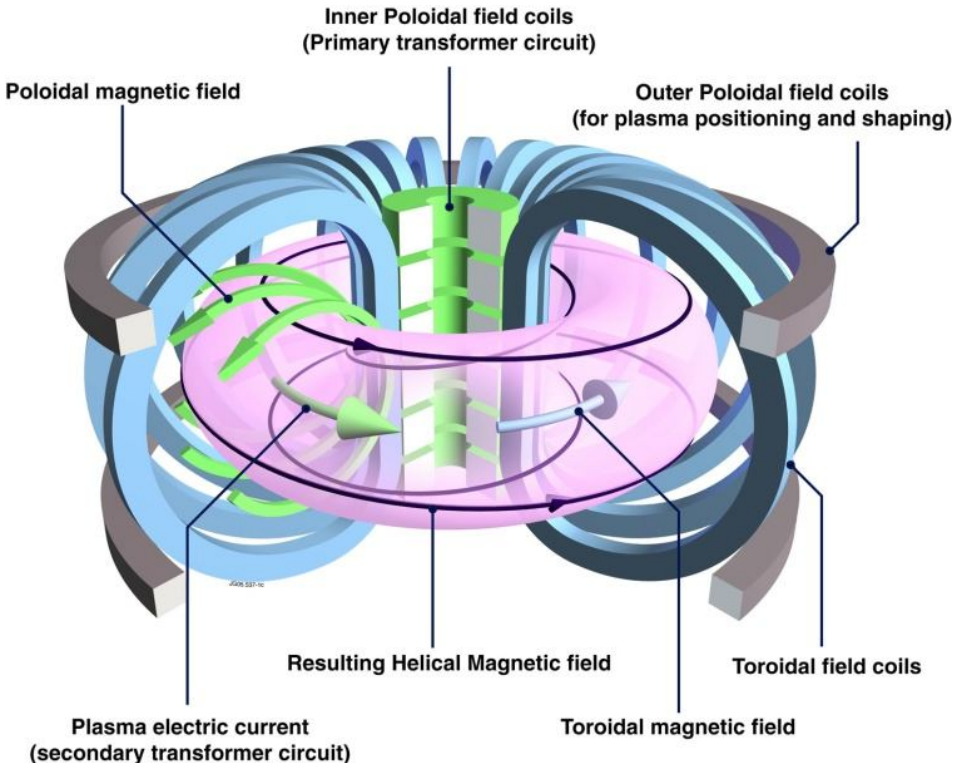

Figure 5: Scheme of a tokamak.

To provide efficient and safe nuclear decontamination without damage of the plasma facing surfaces, a great number of complex interrelated phenomena, physical processes, surface features and appropriate cleaning parameters (such as the layer and substrate physical and chemical properties and structure, the damage threshold, the shape of contaminated surface and its accessibility for cleaning, specific cleaning parameters of the cleaning device or method, and so on) should be taken into account.

1.3 Laser ablation as a decontamination technique

Thus, surface cleaning may be required in different fields of modern technologies and industry. In fusion thermonuclear installations (tokamaks), the deposited layers with a high amount of tritium are formed on the surfaces of Plasma Facing Components (PFC). To satisfy safety requirements, they should suffer cleaning and decontamination. For nuclear industry, chemical cleaning methods (for example, AP-CITROX [7]) are quite common and conventional techniques for metal components cleaning and decontamination. However, they result in a large amount of secondary wastes and protective layer damage on the stainless steel surface, thus resulting in a strong decrease in corrosion resistance. For tokamak vacuum vessel, they may hardly be regarded as suitable as well. Laser cleaning may be regarded as a

supplementary alternative for the known decontamination methods due to the possibility of its automatisation, remote handling and reduced secondary wastes.

1.3.1 Physical principle

Laser cleaning is based on contaminated surface ablation or tritiated surface heating which results in contamination desorption. Laser ablation, as a process of matter removal under high energy laser pulses, has been proposed as in-situ method for metal surface cleaning. For industrial surface decontamination and cleaning, the application of modern reliable powerful fiber lasers (100 – 1000 W mean power) of a simple maintenance should be regarded as quite reasonable and efficient.

The term "laser ablation" may be referred to some interrelated physical processes which result in the matter removal from a solid body. In the majority of papers, laser ablation is referred to solid material damage, similar to evaporation or sublimation, which usually results in the occurrence of a condensed phase in disintegration products. Sometimes, a narrowed interpretation of this term is referred to a far beyond threshold regime of material removal which is accompanying the matter ejection as drops and pieces in a liquid and solid state. In this case, the near threshold regime is referred to as "evaporation under laser irradiation".

Among physical mechanisms which may result in laser ablation, one may mention evaporation/sublimation, phase explosion, mechanical breakdown and photochemical reaction [14]. Laser radiation wavelength, laser pulse duration, laser radiation intensity, and material under treatment are the main parameters which determine laser ablation properties.

For metals, the light absorption coefficient α is of the order of several tens 1/μm and the total laser radiation absorbed by free electrons in a thin layer is of the order of several hundreds of nanometres. This hot electron gas transmits the absorbed energy to the crystal lattice by the electron-phonon interaction with characteristic time of the order of several picoseconds. Therefore, at the nanosecond time scale, the electron gas and the crystal lattice can be described by the unique temperature which follows the thermal conduction equation.

Under the action of short laser pulses, the temperature of a surface layer of a solid body increases rapidly. The high temperature gradient exists in the body. This leads to high mechanical stresses which can cause the mechanical destruction of a target. The increase in temperature body results also in a rapid expansion of a surface layer and in formation of shock wave propagation in-depth of the sample. This shock wave can enhance the mechanical breakdown of matter.

If the laser pulse energy is high enough, the temperature reaches the material melting and evaporation temperature.

For the laser pulses of several dozens of nanoseconds, the heating and evaporation of material can happen before the end of a laser pulse. The evaporated material is heated up by absorbing laser radiation. At high temperatures, the ablated material dissociates (breaks down) into excited ionic and atomic species forming the laser-induced plasma plume. The optical emission of the plasma plume can be analysed to retrieve the information about the target composition [15]. As the plasma plume absorbs some part of laser pulse energy, the efficiency of laser-induced material removal is decreasing [16].

In the case of further increase of the pulse energy, the target material can be heated closer to the spinodal, and the phase explosion may occur [17]. In this regime, the major part of material is removed as liquid droplets.

Laser ablation may be applied in:

- laser cutting, drilling;
- cleaning of silicon wafers; dry laser cleaning;
- restoration and cleaning of artworks and historical monuments;
- cleaning from organic oils;
- cleaning from radioactive contamination (paints, concrete, oxides).

For the latter case, decontamination is achieved by removing contaminated surface layers by laser ablation while capturing the ejected material before matter redeposition or spreading might occur. Laser ablation as a method of nuclear decontamination may offer the following advantages:

- the method automation (minimal risk for personnel, no manual labour);
- small amount of secondary wastes in a solid state (simplifying the compacting and preparing for disposal);
- low impact on the environment.

However, among certain disadvantages, one may mention the necessity of precise laser beam focusing on the surface under treatment. Also, as the shape of the components for cleaning may be very different, the appropriate system design may be quite difficult. In this case, a mechanical system which may provide positioning of the focusing system at a required distance and scanning over the irregular surface may be suggested as a solution [18], [19]. Or else, the design of a relatively simple device for the particularly chosen type of components (for example, pipes) may be suggested in this case. This may help to simplify the mechanical part of the system and to increase efficiency.

1.4 Review of experimental works on laser decontamination

The investigations on laser ablation decontamination with a Q-switched Nd:YAG laser system of 100 ns pulse duration were performed in the USA [20]. The repetition rate of laser system could be varied as 100 Hz – 30 kHz. The maximal output power of 200 W was reached when the repetition rate exceeded 9 kHz. Such pulses were applied to reduce the physical strain of optical fibres (1 mm core diameter) which were used to deliver beam to the surface. These fibres were also tested by γ-radiation exposure. No significant degradation of transmittance was observed. Typically, 92% of the laser output power was delivered to the target with the fibre optics delivery system. The experiments were performed with simulated contaminants and radioactively contaminated samples. The cleaning quality was determined as percent of contamination remained after cleaning. For simulated contaminations, cleaning quality of Zr was about 100% in most of the cases. Cleaning quality of Cs was about 93%. It was demonstrated that most of the contamination was removed in the first pass. Two types of real samples (Haynes 25 samples and lead samples) were also investigated. For hard alloy Haynes 25, decontamination stopped at DF = 3.46 after 4 passes (150 W, 5 kHz and 10 cm/s). This happened because only one surface of the sample was treated. The dependence of residual activity on the number of passes is presented on **Figure 6.**

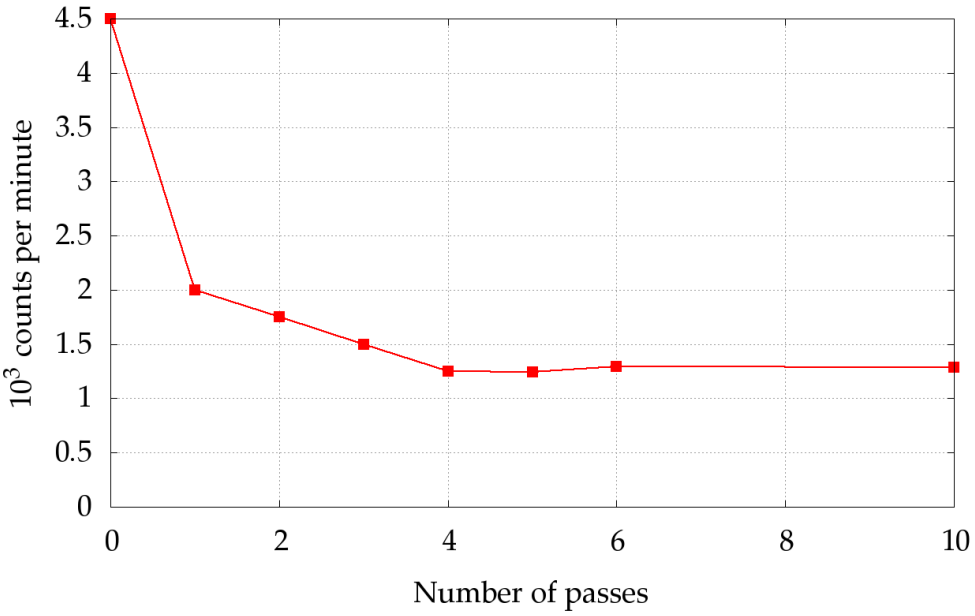

Figure 6: Decrease in radioactivity of the flat surface of the Haynes 25 sample as a function of the number of laser passes across that surface [20].

For the lead brick, contamination dropped to almost a background level after one pass. For a certain zone, DF was only 2 and it did not increase with more passes.

One may suggest that in that zone the contamination was penetrated deeply within the lead brick under study. A high power Q-switched Nd:YAG laser was demonstrated as being very efficient in removing fixed metal surface contamination. The results of this study were patented in the USA in [21].

In France, where about 80% of electric energy is produced by nuclear plants, the problem of nuclear decontamination of metal components is of a special importance. Among the most interesting studies on decontamination by laser ablation, one may mention the investigations in [22], [23]. In these studies, four different wavelengths of available industrial lasers with the following parameters were used:

1. Nd:YAG laser: 1064 nm, 7 ns, 700 mJ, 30 Hz, 21 W
2. Frequency doubled Nd:YAG laser: 512 nm, 7 ns, 250 mJ, 30 Hz, 7.5 W
3. XeCl excimer laser: 308 nm, 30 ns, 300 mJ, 5 Hz, 1.5 W
4. KrF excimer laser: 248 nm, 30 ns, 400 mJ, 1 Hz, 0.4 W

Three types of samples were studed:

- Steel 304 samples "PIVER". Contaminant: ^{137}Cs. No data on the initial activity.
- Samples of vapour generator tubes of 304 steel. Contaminant: ^{60}Co. A_{init}=105 Bq/cm^2. Oxide film thickness of 5 - 20 μm.
- Samples of vapour generator tubes of Inconel. Contaminant: ^{60}Co. A_{init}=20500 Bq/cm^2.

Different types of contaminated surfaces and ablated matter collecting systems were used. Cleaning was performed in air under flowing water film and under film containing nitric acid with 86 m^3/h aspiration speed. The results of this work are presented on Figure 7 and Figure 8. For ablation in air with aspiration, the decontamination factor does not exceed 10 even for very high incident fluences. For ablation under a water film, in contrast, the decontamination factor increases rapidly with the incident fluence. For ablation under diluted nitric acid, the decontamination factor can as be achieved as 300. Moreover, there is no saturation in decontamination factor in this case.

This behaviour can hardly be attributed to the oxide layer, where the contamination is localized. Rather, one should suppose that the density of contamination is of a continuous profile in-depth of the sample under study.

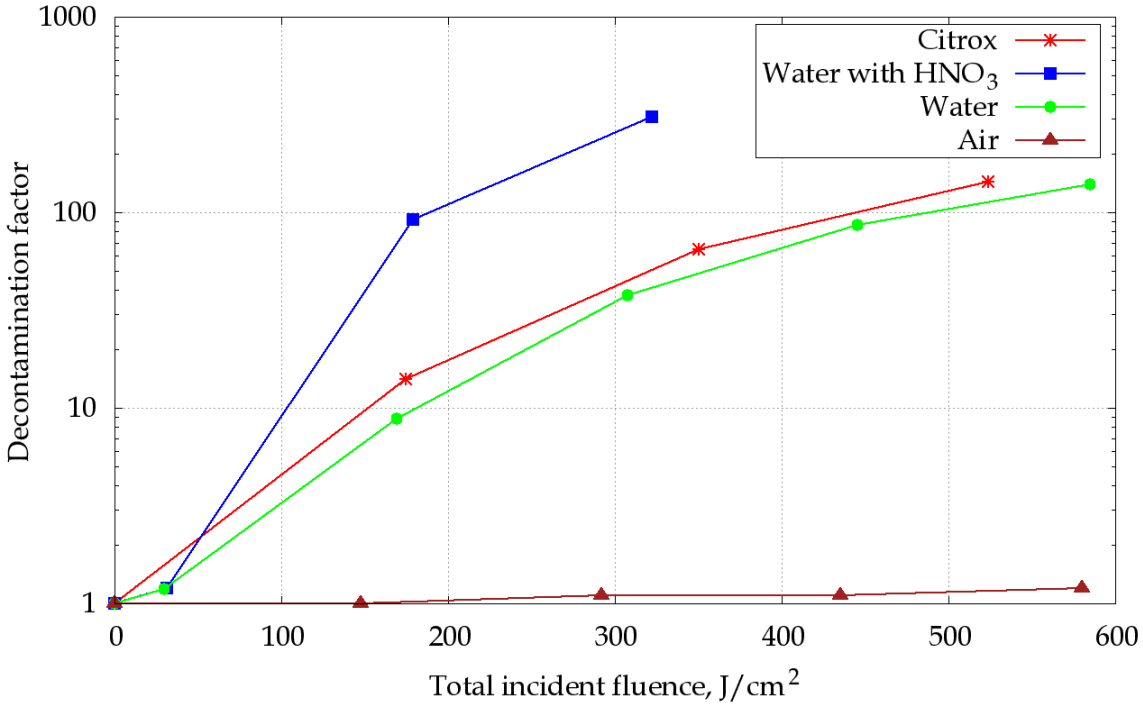

Figure 7: Factor of decontamination of vapour generator tube sample as a function of total incident fluence for different irradiation conditions [22]

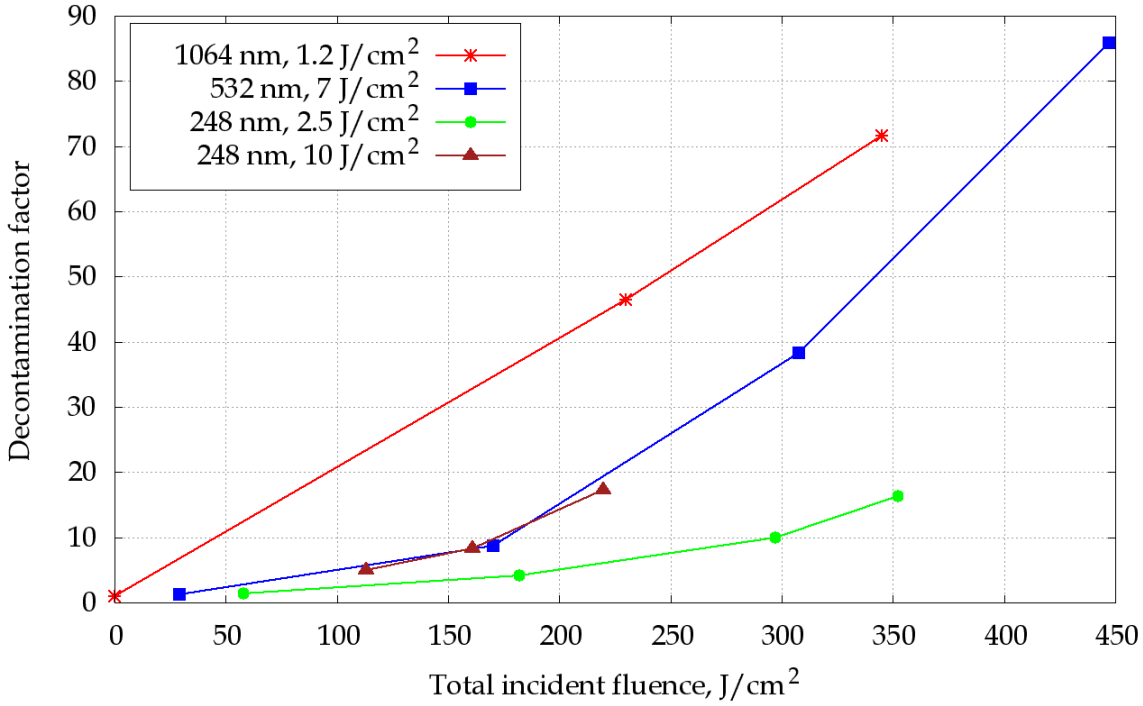

Figure 8: Factor of decontamination of vapour generator tube samples under water as a function of the total incident fluence for different irradiation wavelengths [22]

In almost all the cases mentioned above, the "best wavelengths" were 1064 nm and 532 nm (see **Figure 8**).

For decontamination of a hard alloy (such as Inconel) in air and water, the obtained results were hardly regarded as very optimistic. However, when the sample was covered by HNO_3, the decontamination factor has significantly increased. It was also demonstrated that with the increase in the acid concentration, the decontamination factor was increasing for the same total incident fluence.

To improve laser cleaning efficiency, a number of investigations on liquid-assisted laser treatment have been made since the 1970s. Under laser pulse action, water can turn into vapour and initiate a shock wave, which can expulse particles from the surface. In [24] it was demonstrated that the particle removal from the surfaces by laser light was more efficient with the presence of water on the surface than in ambient air. This water-assisted surface cleaning from particles is also referred to as "Steam Laser Cleaning (SLC)". In case of steam cleaning, a liquid film or capillary condensed water on the surface is superheated by a laser pulse and, subsequently, results in its explosive evaporation. The expanding vapour ejects the particles from the surface.

In contrast to "dry ablation", the pressure in the liquid film was 4-10 times greater and was maintained 2 times longer. With high laser beam intensity, the pressure has saturated and the pressure pulse duration was decreasing due to parasitic breakdown in the liquid [25–28]. The presence of a liquid film has increased the ablated volume per pulse. However, for polymethyl-methacrylate samples, further increase in layer thickness has resulted in decrease in ablation efficiency [29].

In [22], [23], a significant increase in decontamination factor for laser ablation under water flow was also reported. In [30], [31], optimistic results associated with liquid-assisted laser treatment were also presented.

In 2000, a French project focusing on excimer XeCl laser for decontamination of metal components was launched in CEA Saclay. Within the framework of this project, the laser cleaning system was designed and created [18], [32]. The system was applied for decontamination of real samples from vapour generator tubes made of stainless steel and Inconel. Aluminium samples from the fuel waste retreatment facility were also under study in [33], [34]. In these experiments, the XeCl laser (80 W mean power) and optical fibre transport of the laser beam to the sample was used.

For stainless steel and aluminium, the results were quite satisfactory. However, for Inconel, the decontamination factor did not exceed 2. This result may be associated with the presence of deep cracks on the surface of the Inconel sample under study. For the stainless steel, these cracks filled with the oxide were less important than for Inconel where they were deeper than 150 μm.

In Russia, the most important experimental studies on laser decontamination were performed in the Bochvar Research Institute (VNIINM, Moscow) [35–37]. The first experiments on artificially contaminated samples of stainless steel, carbon steel and brass were made in a glove box with a pulsed Nd:YAG laser of the following parameters:

- Power: 100 – 150 W
- Pulse energy: 1.1 – 1.5 J (total over a burst)
- Duration:
  - Monopulses: 100 – 500 μs, 50 Hz
  - Pulse bursts: 100 ns, 100 kHz (full duration of bursts: 100 – 500 μs)
- Fluence and intensity:
  - Monopulses: 8 – 100 J/cm^2 (80 – 200 kW/cm^2)
  - Bursts: 0.8 – 1 J/cm^2 (80 – 100 MW/cm^2)
- Light spot: narrow line of 0.1 − 0.2 mm in length and 3 − 5 mm in width, S = 0.3 − 1 mm^2
- Scanning speed: 10 – 40 mm/s

The tests on these artificially contaminated samples demonstrated that the decontamination factor was about 20. The experiments on real samples (the pieces of Raschig rings) revealed decontamination factor in the range of 20–82 after three passes.

Along with the decontamination factor measured in this study, the size distribution of the ejected particles was also determined. The particles size distribution for a stainless steel sample is presented on **Figure 9**. From this figure, the most part of contaminated layer is ejected as very small particles of a size less than 1 μm.

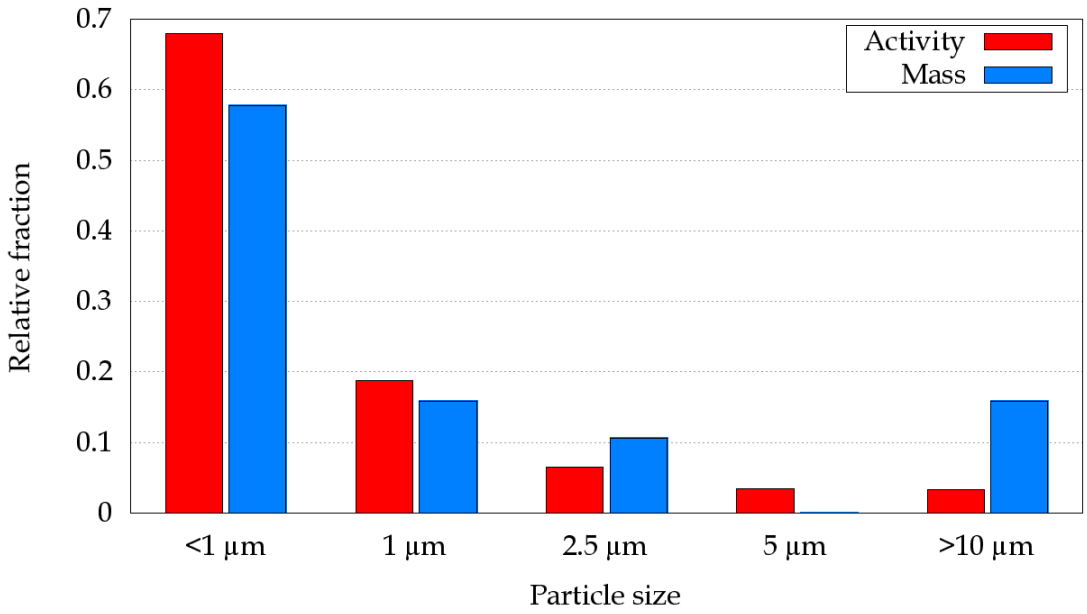

Figure 9: Size distribution of particles produced during cleaning of stainless steel sample for 200 µs pulses and 85 Hz repetition rate

As continuation of these studies, a mobile laser decontamination system prototype is under construction. The prototype construction is scheduled for the end of 2011. This system will be able to handle metallic tubing constructions of a complex surface of 0.5 - 1.5 m diameter and up to 2 m length.

The experiments on the oxide layer removal from metal substrates were made in Saint-Petersburg at ITMO University in [38]. In this study, a pulsed Nd:YAG laser with 10 ns laser pulses was used. The depth and surface of the oxide removal as a function of laser beam intensity was determined. The results of this work are presented on Figure 10. From this figure, the ablation mechanism is different for low and high intensities. For $I < 150$ MW/cm^2, the main mechanism is seen as thermomechanical ablation, while for I > 150 MW/cm2, it is seen as evaporation ablation.

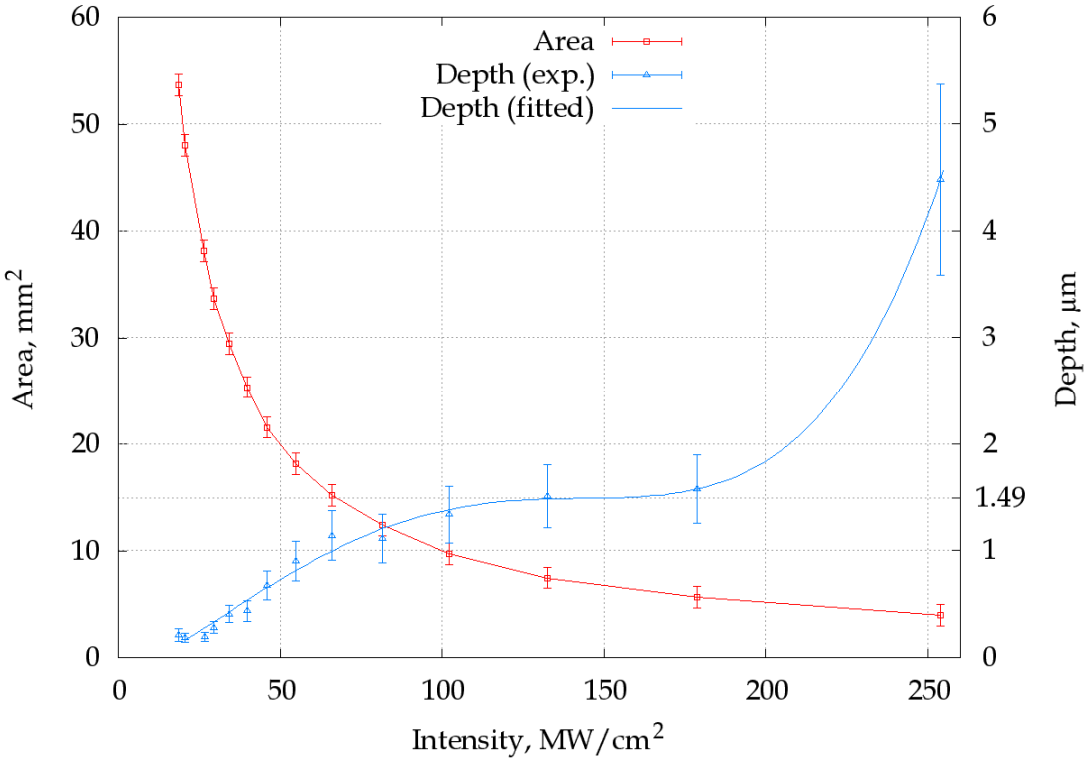

Figure 10: Results of laser ablation of a corroded layer: ablated layer thickness and processed surface area versus intensity of the applied laser radiation [38]

The study on laser removal of loose uranium compound contamination was made in South Africa [39]. In this study, the laser removal of a loose uranyl nitrate and uranium dioxide contamination was under consideration. These compounds were used for fuel production for Pebble Bed Modular Reactor (PBMR). A pulsed Nd:YAG laser (7 – 10 ns pulses, 0.8 J energy) was used to clean the samples under study. It was demonstrated that one laser pass with 0.36 J/cm^2 has removed 85% of UO2 and 98% of uranyl nitrate. These results may testify to the fact that laser treatment can be very effective even with such low fluences for cleaning loose contaminations.

In [40], the feasibility tests to select the most appropriate light source were performed with surrogate samples with a continuous CO_2 laser, a continuous Nd:YAG laser and a pulsed Nd:YAG laser used as light sources. The pulsed Nd:YAG laser was found to be the most efficient among them.

Despite evident efficiency of laser ablation cleaning, it might be not satisfactory for certain particular cases. Thus, it should be regarded mainly as supplementary cleaning techniques to the conventional ones.

1.5 The aims of our studies

The above thorough review of the state-of-art of modern cleaning and decontamination methods and techniques and also the analysis of the previously obtained results of investigations performed in different research laboratories were made to define the scope of our investigations. The analysis of these results and data was used to determine and precise the steps of our theoretical and experimental studies on "Laser decontamination and cleaning of metal surfaces: modelling and experimental studies" within the frames of our research interest in this field. As a result, our study was aimed to the following:

1. modelling of laser heating of metal surface with a layer;
2. development and application of experimental equipment for studies on high repetition rate laser surface heating and cleaning by laser ablation;
3. ablation threshold determination for different metal surfaces (oxide layer on stainless steel, ITER-like samples, Mo-mirror);
4. experimental studies on laser ablation efficiency (Decontamination Factor, ablation rate, metal substrate damaging) for cleaning metal surfaces with contaminated layer;
5. Tokamak diagnostics mirrors cleaning to reconstruct their initial reflectivity.

Experimental and theoretical results comparison to improve and validate the developed models was under particular attention in these studies.

Chapter 2. Models of laser heating of metal surfaces

Contents

In this chapter, we discuss interaction of laser beam with metal substrate and determine damage thresholds for materials under study with taking into account alteration of the reflection coefficient with temperature and accumulation of plastic deformations for repetitive laser pulses.

For laser cleaning of metal mirrors (molybdenum and stainless steel mirrors, in our case), it is necessary to choose appropriate laser parameters to avoid irreversible damage of mirror surface. Below, we present the model to calculate the damage threshold fluence for metals.

We suppose that damage occurs at the fluence when the maximal temperature due to laser heating reaches the melting point. Below, we will present the model of laser heating of metal surface which is applied to determine damage thresholds for metals.

Propagation of light in the layer is discussed. As deposited layers of thermonuclear devices and oxide layers formed in nuclear installations are inhomogeneous, the scattering in the layer is considered. The model to calculate the light intensity distribution for such layers is proposed and compared with the known limiting cases.

2.1 Laser heating of pure metal surface

We consider the interaction of laser pulse with the Gaussian spatial profile with a semi-infinite metal substrate (see **Figure 11**). Laser beam intensity distribution is $I(r) = I_0 \exp\left(-r^2/a^2\right)$, where I_0 is an maximal intensity at the center of the beam and a is a laser beam radius at $1/e$ intensity.

To find the temperature distribution $T(x, y, z, t)$ in target, we need to solve the heat conduction equation, which is the following

$$\rho \frac{\partial T}{\partial t} = k\nabla^2 T \qquad (1)$$

where metal is described by the following thermophysical features:

- density ρ [kg/m^3]
- specific heat capacity c [J/kg·K]
- thermal conductivity k [W/m·K]
- thermal diffusivity $\kappa = k/\rho c$ [m^2/s]

In equation (1), we suppose that the features do not depend on temperature. It was shown in [41] that for graphite, the mean temperature-independent thermophysical features can be used instead of temperature-dependent ones in laser heating calculations. We suppose that the same is true for metals.

The optical properties of the metal substrate are:

- absorption coefficient α [1/m]
- reflection coefficient R

As we are interested in heating of the metal surface, we should solve heat conduction equation with the appropriate initial and boundary conditions:

$$T(x,y,z,0) = 0 \quad T(\infty,t) = 0 \quad -k\frac{\partial}{\partial} = f(x,y,z,t) \tag{2}$$

where ρ is the density, c is the specific heat, k is the thermal conductivity of the sample and $f(x, y, z)$ is the heat sources distribution, which indicates how much of energy is liberated in a unit volume at a given point. Here and further in this work, the temperature is counted from room temperature.

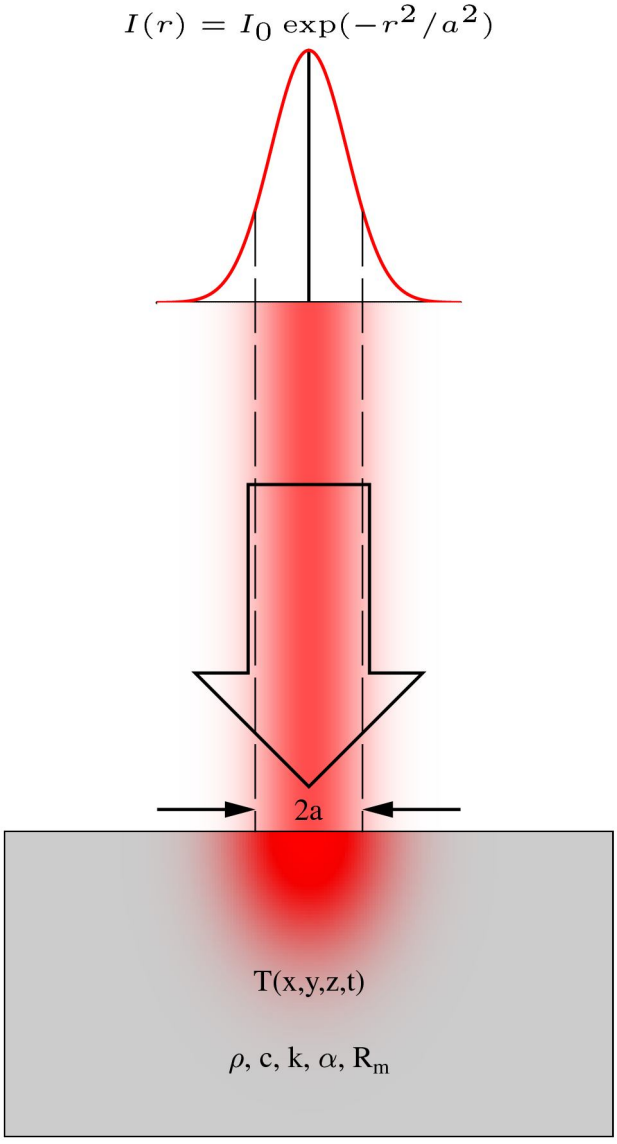

Figure 11: Scheme of laser heating of material

Different regimes of target heating by laser beam can be considered: surface and volume heating applied with one or high repetitive rate pulses.

2.1.1 Surface heating

The surface heating regime is realized when the absorption length can be neglected over the heat diffusion length during the pulse duration.

For a Nd:YAG laser (wavelength $\lambda = 1.064$ μm), the absorption coefficient of metals is equal to tens of inverse micrometers at room temperature (see **Appendix A**). In our case, the diameter of laser beam on the surface is 150 μm on e^{-2} intensity level and the characteristic heat diffusion length during the pulse $l = \sqrt{4\kappa\tau}$ (see below) is sufficiently greater than the absorption length $\alpha^{-1} \approx 0.0\ 2$ μm. So, we can apply the 1D model of surface laser heating.

The surface heating model implies $f(x, y, z, t) \sim \delta(z)$ that means that the heat sources are confined at the surface. To calculate heating temperature at the origin ($x = y = z = 0$) due to laser heating, the method of the Green's function will be used [42]. To obtain the Green's function $T_\delta(t)$ at the origin, let's consider the superficial instantaneous unit impact with the Gaussian laser beam. The heating sources function then writes as

$$f_\delta(x, y, z, t) = \frac{(1-R)}{\pi a^2} \mathrm{e}\ \mathrm{x}\left(-\frac{x^2+y^2}{a^2}\right)\delta(z)\delta(t) \tag{3}$$

Index δ means that this value corresponds to instantaneous heating pulse. The temperature profile, which corresponds to such heating, writes as [43]:

$$T_\delta(x, y, z, t) = \sqrt{\frac{\kappa}{\pi}}\frac{(1-R)E}{k\ (a^2+4\kappa)}\mathrm{e}\ \mathrm{x}\left(-\frac{x^2+y^2}{a^2+4\kappa}-\frac{z^2}{4\kappa}\right) \tag{4}$$

At the origin of coordinates ($x = y = z = 0$) where the temperature is maximal, it gives:

$$T_\delta(t) = \sqrt{\frac{k}{\pi}}\frac{(1-R)E}{k\ (a^2+4\kappa)} \tag{5}$$

According to the Green's theorem, the solution at time τ for the heating varying with time as $P(t)$ can be obtained using the following expression:

$$T(\tau) = \int_{-\infty}^{\tau} P(t)T_\delta(\tau - t)d \tag{6}$$

For the case of continuous wave (CW) laser heating that switches on at time $t = 0$, the laser power $P(t)$ has a form:

$$P(t) = \begin{cases} 0 & x < 0 \\ P_0 & x \geq 0 \end{cases} \tag{7}$$

where P_0 [W] is laser power. Then, expression for heating temperature (6) transforms to:

$$T(\tau) = \int_0^{\tau} \sqrt{\frac{\kappa}{\pi}} \frac{(1-R)P_0}{k\,(a^2 + 4\kappa\,)} d\,\, = \frac{(1-R)P_0}{k\,\pi^{3/2}} \mathrm{arc}\,\frac{\sqrt{4\kappa}}{a} \tag{8}$$

Using this expression, one can calculate the temperature on the surface at the centre of the Gaussian laser beam at the time τ after beginning of CW laser heating. The obtained result is in accordance with the one obtained in [44] using the Hankel and the Laplace transformation techniques.

For small τ, when $\frac{\sqrt{4\kappa\,\tau}}{a} \ll 1$, the expression (8) can be simplified using relation $\mathrm{arc}\,tx \approx x$ to

$$T(\tau) = \frac{(1-R)P}{k\,\pi^{3/2}} \frac{\sqrt{4\kappa}}{a} \tag{9}$$

The dependence of the dimensionless temperature $\eta = T/T_m$, where $T_m = (1-R)P/2k\,\pi\sqrt{\pi}$, on the dimensionless time $\xi = 4\kappa\,\tau/a^2$ can then be expressed as

$$\eta = \frac{2}{\pi} \mathrm{arc}\,\sqrt{\xi} \tag{10}$$

The expressions (9) and (10) give the possibility to determine the heating temperature for pure metal surface under interaction with CW laser beam of the Gaussian spatial profile. Figure 12 shows the dependence of dimensionless heating temperature as the function of the heating time. There are two different cases that can be distinguished:

- 1D heating for $\xi \ll 1$ with $T(\tau) \sim \sqrt{\tau}$
- 3D heating for $\xi \gg 1$ with $T(\tau) \sim \mathrm{arc}\,\frac{\sqrt{4\kappa\,\tau}}{a}$

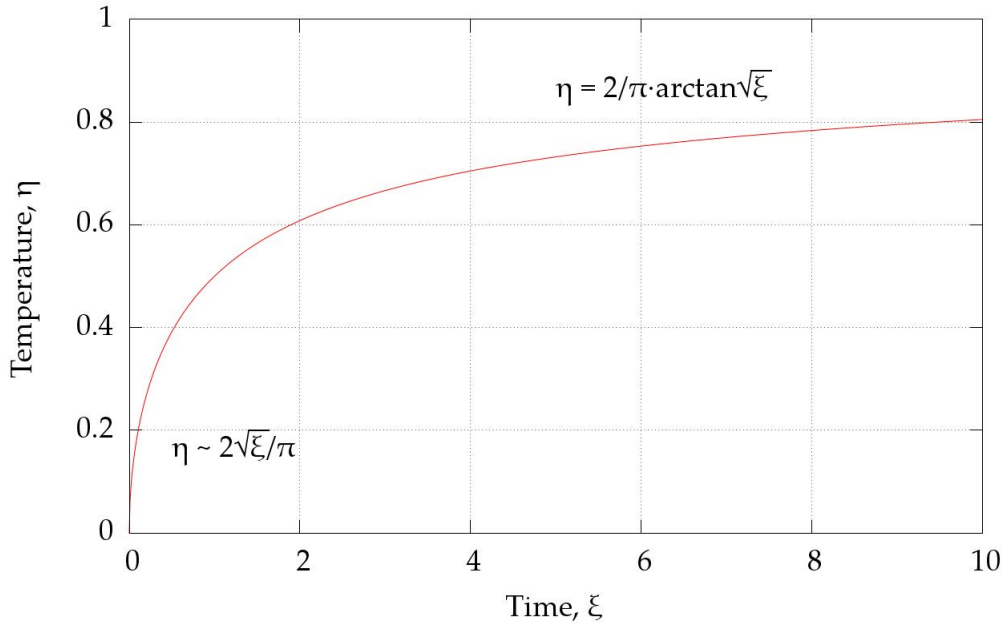

Figure 12: Dimensionless temperature at the origin as a function of dimensionless time.

Laser fluence is $F = E/\pi a^2$, laser power P can be associated with fluence F, radius a, pulse duration τ and pulse energy E as:

$$P = \frac{\pi a^2 F}{\tau} = \frac{E}{\tau} \tag{11}$$

Then, for 1D case, we obtain:

$$T(\tau) = \frac{(1-R)E}{k\ a^2}\sqrt{\frac{4\kappa}{\pi}} \tag{12}$$

From this expression, it can be concluded that for a laser pulse of a given energy, the heating temperature decreases with the pulse duration as $1/\sqrt{\tau}$.

In the case of multi-pulse heating, the temperature after the N-th pulse will be slightly higher than after the first one. It happens because heat has not enough time to diffuse in-depth of the sample and when the second laser pulse arrives, the surface temperature is slightly higher than it was before beginning of heating. Moreover, when the average laser power and repetition rate are constants, this temperature will depend on pulse duration.

To calculate additional temperature increase caused by repetitive pulsed heating, it is necessary to have the expression for temperature $T(t)$ at any moment after the pulse of duration τ. To calculate it, we will use linearity of heat conduction equation (1). This means that if $T_1(t)$ and $T_2(t)$ are temperatures caused by excitations $f_1(t)$ and $f_2(t)$, then $T_s(t) = T_1(t) + T_2(t)$ is the temperature caused by the total

excitation $f_s(t) = f_1(t) + f_2(t)$. Then, we can decompose the pulse excitation into two Heaviside excitations as indicated in Figure 13.

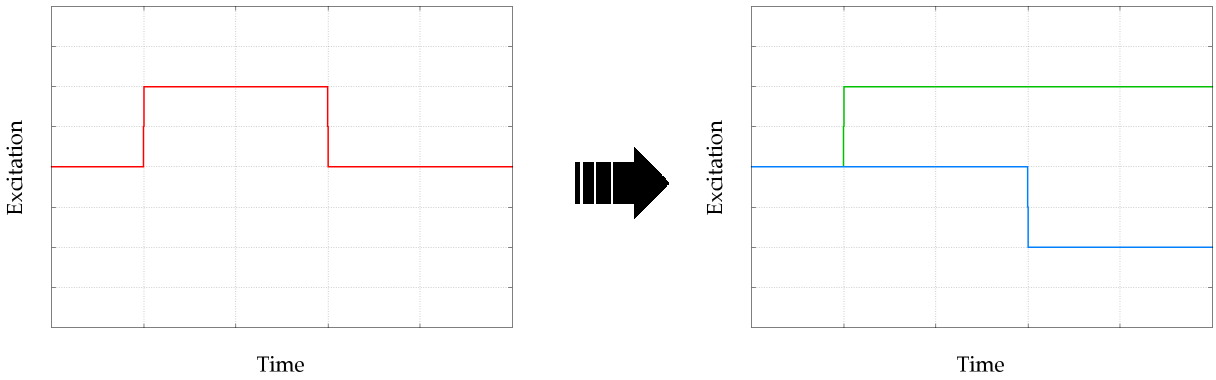

Figure 13: Decomposition of pulse excitation into two Heaviside excitations

Then, using formula (8), it is possible to write the temperature at the origin on the surface at the time t after laser pulse of duration τ as:

$$T(t,\tau) = \begin{cases} 0 & t < 0 \\ \dfrac{(1-R)P_0}{k\,\pi^{3/2}} \mathrm{arctan}\dfrac{\sqrt{4\kappa\,t}}{a} & 0 \le t \le \tau \\ \dfrac{(1-R)P_0}{k\,\pi^{3/2}} \left[\mathrm{arctan}\dfrac{\sqrt{4\kappa\,t}}{a} - \mathrm{arctan}\dfrac{\sqrt{4\kappa(t-\tau)}}{a} \right] & t > \tau \end{cases} \tag{13}$$

During the laser pulse ($0 \le t \le \tau$), the expression for heating temperature is the same as for constant heating (8). After the laser pulse ($t > \tau$), the expression consists of two terms. The first term corresponds to the constant heating starting at $t = 0$. The second term corresponds to the negative heating source of the same power that switches on at the end of the laser pulse $t = \tau$.

In order to calculate maximal temperature just at the end of the N-th laser pulse, we should compute the sum over all preceding pulses:

$$T_{max}(N) = \sum_{n=0}^{N-1} T(nt_0 + \tau, \tau) \tag{14}$$

where t_0 is a period between pulses.

The sum in (14) converges with the number of pulses to T_{max} which can be computed numerically. The sum term in (14) can be simplified using the relation $\mathrm{arctan}\,x + \mathrm{arctan}\,y = \mathrm{arctan}\frac{x+y}{1-xy}$ [45] to:

$$T(nt_0+\tau,\tau)=\frac{(1-R)f_0}{k\ \pi^{3/2}}\mathrm{a\ r\ c}\left(\frac{a\sqrt{4\kappa}\left(\sqrt{nt_0+\tau}-\sqrt{nt_0}\right)}{a^2+4\kappa\sqrt{nt_0(nt_0+\tau)}}\right) \tag{15}$$

2.1.2 Volume heating

In the case when absorption length $1/\alpha$ is comparable with the heat diffusion length $\sqrt{4\kappa}$ the approximation of surface heating is not valid and the in-depth distribution of heat sources must be taken into account to get a correct expression for temperature on the surface.

To obtain the expression for heating temperature due to constant laser heating, at first, we will derive the time Green's function for instantaneous unit heating impact that has the Gaussian lateral profile and decreases in-depth according to the Beer-Lambert law. In this case, the heating source writes as:

$$f(x,y,z,t)=\frac{\alpha e^{-\alpha}}{\pi a^2}\mathrm{e\ x}\left(-\frac{x^2+y^2}{a^2}\right)\delta(t) \tag{16}$$

where a is the beam radius and α is the absorption coefficient.

To deal with semi-infinite body, we want to point out that the temperature field produced by a heat source in point (x',y',z') of semi-infinite body equals to the half of temperature field produced in infinite body by two heat sources (x',y',z') and $(x',y',-z')$. In this case, the boundary condition $-k\frac{\partial T}{\partial z}=0$ (there is no heat flux across the surface) will be automatically satisfied from a reason of symmetry. So, we can use infinite body with the following heat source:

$$f(x,y,z,t)=\frac{\alpha e^{-\alpha|z|}}{\pi a^2}\mathrm{e\ x}\left(-\frac{x^2+y^2}{a^2}\right)\delta(t) \tag{17}$$

The temperature field produced in homogeneous infinite body by unit point instantaneous energy source placed in (x',y',z') is given by the expression [42]:

$$T_p(x,y,z,x',y',z',t)=\frac{1}{8k\sqrt{\kappa}(\pi)^{3/2}}\mathrm{e\ x}\left(-\frac{(x-x')^2+(y-y')^2+(z-z')^2}{4\kappa}\right) \tag{18}$$

where k is the thermal conductivity and κ is the thermal diffusivity of body.

To compute the temperature field caused by heating sources (17), we should take an integral over all space and time:

$$T_\delta(x,y,z,t)=\frac{1}{2}\iiint_\Omega T_p(x,y,z,x',y',z',t-\xi)f(x',y',z',\xi)dx'dy'dz'd \tag{19}$$

The integral over time can be easily eliminated as the expression under integral contains $\delta(\xi)$ and substituting here expressions for T_δ and f, we obtain:

$$T_\delta(x,y,z,t) = \\ = \frac{1}{2}\overbrace{\iint_{-\infty}^{+\infty}\frac{1}{\pi a^2}\exp\left(-\frac{x'^2+y'^2}{a^2}\right)\frac{1}{4k\sqrt{\kappa}(\pi t)^{3/2}}\exp\left(-\frac{(x-x')^2+(y-y')^2}{4\kappa t}\right)dx'dy'}^{I_1} \times \\ \times \underbrace{\int_{-\infty}^{+\infty}\alpha e^{-\alpha|z'|}\exp\left(-\frac{(z-z')^2}{4\kappa t}\right)dz'}_{I_2} \tag{20}$$

Let's consider integral I_1:

$$I_1 = \frac{1}{\pi a^2 k\sqrt{\kappa}(\pi t)^{3/2}}\int_{-\infty}^{+\infty}\exp\left(-\frac{x'^2}{a^2}\right)\exp\left(-\frac{(x-x')^2}{4\kappa t}\right)dx' \times \\ \times \int_{-\infty}^{+\infty}\exp\left(-\frac{y'^2}{a^2}\right)\exp\left(-\frac{(y-y')^2}{4\kappa t}\right)dy' \tag{21}$$

In order to take these integrals, we should isolate full squares in exponents:

$$\int_{-\infty}^{+\infty}\exp\left(-\frac{x'^2}{a^2}-\frac{x^2}{4\kappa t}-\frac{x'^2}{4\kappa t}+\frac{2xx'}{4\kappa t}\right)dx' = \\ = \int_{-\infty}^{+\infty}\exp\left(-\left[\frac{\sqrt{4\kappa t+a^2}\cdot x'}{\sqrt{4\kappa t}\cdot a}-\frac{a\,x}{\sqrt{4\kappa t+a^2}\cdot\sqrt{4\kappa t}}\right]^2+\frac{a^2x^2}{(4\kappa t+a^2)\cdot 4\kappa t}-\right. \\ \left.-\frac{x^2}{4\kappa t}\right)dx' = \exp\left(-\frac{x^2}{4\kappa t+a^2}\right)\times \\ \times\int_{-\infty}^{+\infty}\exp\left(-\left[\frac{\sqrt{4\kappa t+a^2}\cdot x'}{\sqrt{4\kappa t}\cdot a}-\frac{a\,x}{\sqrt{4\kappa t+a^2}\cdot\sqrt{4\kappa t}}\right]^2\right)dx' = \\ = \exp\left(-\frac{x^2}{4\kappa t+a^2}\right)\underbrace{\int_{-\infty}^{+\infty}e^{-t^2}dt}_{\sqrt{\pi}}\frac{\sqrt{4\kappa t}\cdot a}{\sqrt{4\kappa t+a^2}} \tag{22}$$

Therefore, we obtain for I_1

$$I_1 = \frac{1}{a^2 4k\sqrt{\kappa}(\pi t)^{3/2}}\times\frac{4\kappa t\,a^2}{4\kappa t+a^2}\exp\left(-\frac{x^2+y^2}{4\kappa t+a^2}\right) \tag{23}$$

We split integral I_2 into two integrals:

$$I_2 = \int_{-\infty}^{+\infty} \alpha e^{-\alpha|z'|} \exp\left(-\frac{(z-z')^2}{4\kappa}\right) dz' = \\ = \underbrace{\int_{0}^{+\infty} \alpha e^{-\alpha z'} \exp\left(-\frac{(z-z')^2}{4\kappa\, t}\right) dz'}_{I_+} + \underbrace{\int_{-\infty}^{0} \alpha e^{\alpha z'} \exp\left(-\frac{(z-z')^2}{4\kappa\, t}\right) dz'}_{I_-} \tag{24}$$

Integral I_- can be rewritten as:

$$I_- = \int_{0}^{+\infty} \alpha e^{-\alpha z'} \exp\left(-\frac{(z+z')^2}{4\kappa}\right) dz' \tag{25}$$

So, to take I_2, we must take the following integral:

$$\int_{0}^{+\infty} e^{-\alpha z'} \exp\left(-\frac{(z \pm z')^2}{b^2}\right) dz' = \int_{0}^{+\infty} \exp\left(-\left[\frac{z'^2}{b^2} + \alpha z' \pm \frac{2zz'}{b^2} + \frac{z^2}{b^2}\right]\right) dz' = \\ = \int_{0}^{+\infty} \exp\left(-\left[\left(\frac{z'}{b} + \left(\frac{\alpha\, b}{2} \pm \frac{z}{b}\right)\right)^2 - \frac{\alpha^2 b^2}{4} \mp \alpha\, z\right]\right) dz' = \\ = \underbrace{\exp\left(\frac{\alpha^2 b^2}{4} \pm \alpha\, z\right)}_{A} \int_{0}^{+\infty} \exp\left(-\left(\frac{z'}{b} + \left(\frac{\alpha\, b}{2} \pm \frac{z}{b}\right)\right)^2\right) dz' = A \int_{\frac{\alpha\, b}{2} \pm \frac{z}{b}}^{+\infty} b e^{-t^2} dt = \\ = A\, b \left(\int_{0}^{+\infty} e^{-t^2} dt - \int_{0}^{\frac{\alpha\, b}{2} \pm \frac{z}{b}} e^{-t^2} dt \right) = \frac{A\, b\sqrt{\pi}}{2} \left(1 - \operatorname{erf}\left(\frac{\alpha\, b}{2} \pm \frac{z}{b}\right)\right) = \\ = \frac{\alpha\, b\sqrt{\pi}}{2} \exp\left(\frac{\alpha^2 b^2}{4} \pm \alpha\, z\right) \operatorname{erfc}\left(\frac{\alpha\, b}{2} \pm \frac{z}{b}\right) \tag{26}$$

where $\operatorname{erf}(x) = \frac{2}{\sqrt{\pi}} \int_0^x e^{-t^2} dt$ and $\operatorname{erfc}(x) = 1 - \operatorname{erf}(x)$ are error function and complementary error function respectively.

Using this expression, we obtain for I_2:

$$I_2 = I_+ + I_- = \alpha\sqrt{\pi\, \kappa} \exp(\kappa\, \alpha^2) \left[e^{\alpha z} \operatorname{erfc}\left(\frac{\alpha\sqrt{4\kappa}}{2} + \frac{z}{\sqrt{4\kappa}}\right) + e^{-\alpha z} \operatorname{erfc}\left(\frac{\alpha\sqrt{4\kappa}}{2} - \frac{z}{\sqrt{4\kappa}}\right) \right] \tag{27}$$

And finally we receive the time Green's function as:

$$T_\delta(x, y, z, t) = \frac{\alpha\, 1}{2\pi\,)(a^2 + 4\kappa\,)} \exp\left(\alpha^2 \kappa\, - \frac{x^2 + y^2}{a^2 + 4\kappa}\right) \left[e^{-\alpha z} \operatorname{erfc}\left(\frac{2\alpha\, \kappa - z}{2\sqrt{\kappa}}\right) + \right. \\ \left. + e^{\alpha z} \operatorname{erfc}\left(\frac{2\alpha\, \kappa + z}{2\sqrt{\kappa}}\right) \right] \tag{28}$$

For the origin, it is evaluated as:

$$T_\delta(t) = \frac{\alpha\ \ e^{\alpha^2\kappa}}{\pi\ )(a^2 + 4\kappa\ )}\mathrm{e}\ \ \mathrm{r}\ \ \alpha\sqrt{\kappa} \tag{29}$$

To obtain the temperature for continuous heating, we must take the integral:

$$T(\tau) = \int_{-\infty}^{\tau} P(t)T_\delta(\tau - t)d \tag{30}$$

This integral cannot be taken in analytical form even for constant heating (7), so numerical calculations should be performed for heating temperature calculation. Further in section 2.2 we will use this result to compare surface and volume heating models.

2.1.3 Temperature dependence of material absorptance

In many cases, the most significant discrepancy of experimental results and the model occurs due to temperature dependence of material absorptance. The analytical solution of 1D heat conduction equation in the case of changing surface absorptance was obtained in [46].

In this work, the temperature dependence of absorptance is supposed to be a linear function of surface temperature $A(T_s) = A_0 + A_1T_s$, where A_0 is absorptance at room temperature. In this case, the temperature rise at the surface at the time t after beginning of CW heating will be:

$$T(t) = \frac{A_0}{A_1}\left[e^{u^2}(1 + \mathrm{e}\ \ 1u) - 1\right] \tag{31}$$

where $u = \frac{IA_1}{k}\sqrt{\kappa}\ t$and I is laser beam intensity. The damage threshold can be determined as:

$$F_{th} = \frac{u}{A_1}\sqrt{\frac{\tau}{\kappa}} \tag{32}$$

where u is a solution of equation (31) for $T = T_m$, where T_m is a melting temperature.

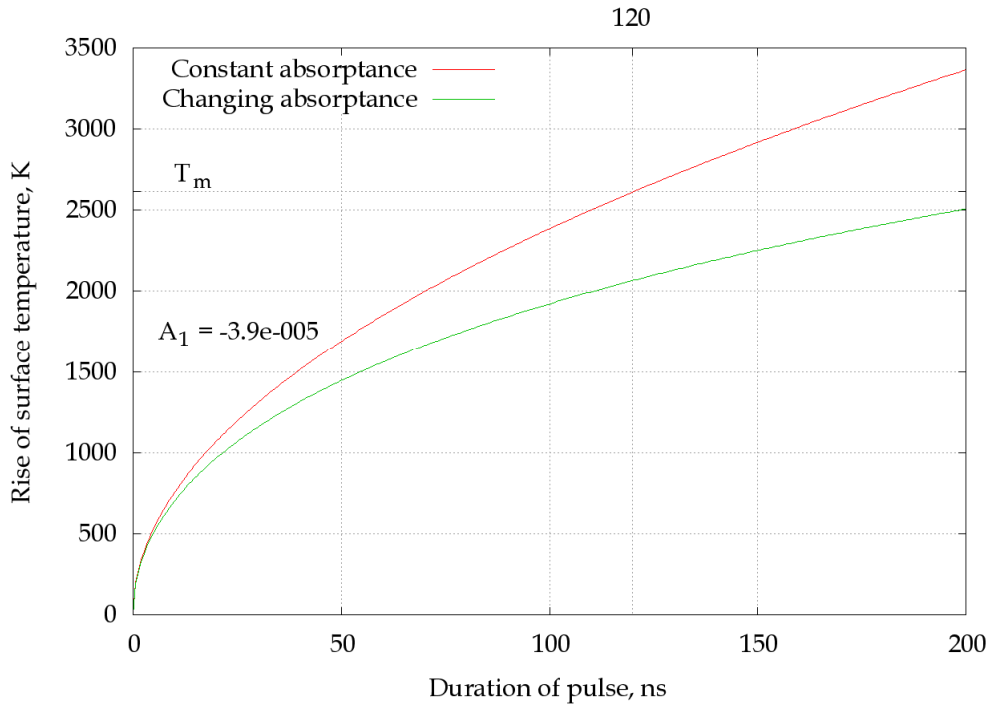

Figure 14: Time dependence of molybdenum surface temperature.

On Figure 14, the time dependence of surface temperature for constant and changing absorptance is presented. To produce this plot, a CW irradiation was supposed with intensity $I = F_{th}/\tau = 4.06$ MW/cm². The value $A_1 = -3.9 \cdot 10^{-5}$ was calculated from spectral emissivity measurements [47]. You can see that due to the same irradiation, the temperature is lower in the case of changing absorptance and, thus, the damage thresholds should increase. In order to determine a threshold, we should solve equation (31) with $I = F/\tau$ for fluence F when $T = T_m$.

On Figure 15, the surface temperature as a function of laser fluence is presented. One can see that for molybdenum mirror, the damage threshold changes from 4.67 J/cm² to 6.67 J/cm² if we take into account temperature dependence of Mo absorptance.

To the best of our knowledge, there is no experimental data on the temperature dependence of the absorptance of emissivity for stainless steel (and particularly for AISI 316L) at 1.064 μm. But the measured λ_x (X-point, for more information see [48], [49]) of major components of stainless steel (namely iron, chromium and nickel) are higher than 1.06 μm and we can suppose that λ_x of stainless steel is also higher than 1.06 μm [48]. Hence, absorptance of stainless steel should decrease with temperature, which means that $A_1 < 0$ for SS. The precise value of A_1 will be evaluated below on the basis of experimental results.

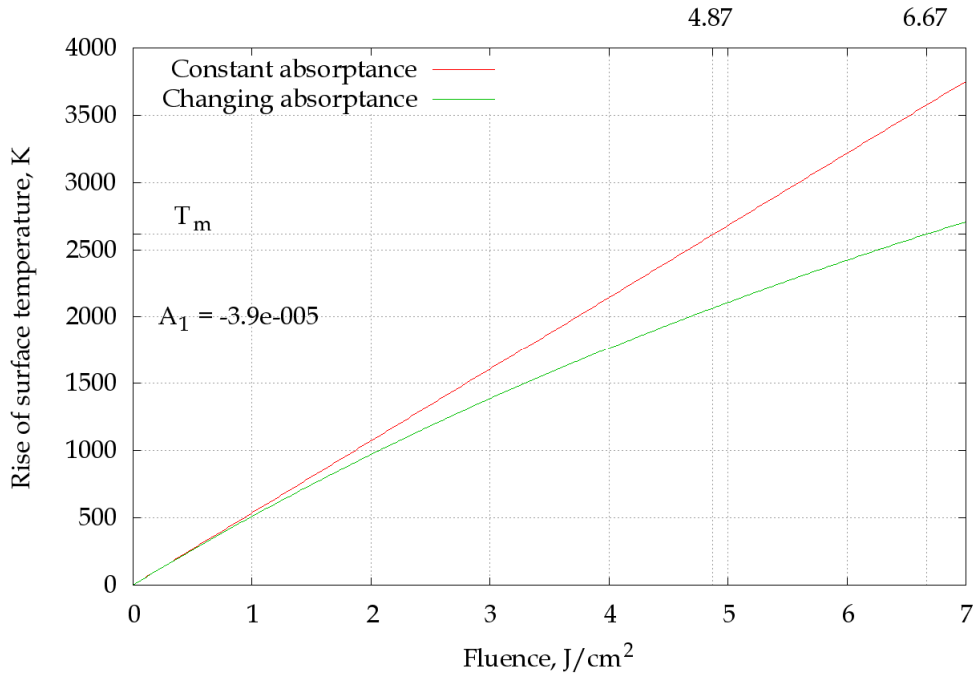

Figure 15: Surface temperature as a function of laser fluence for molybdenum sample.

2.2 Damage thresholds

In order to determine damage thresholds, we suppose that damage occurs on the surface of a target heated by laser when its temperature increases up to the melting point.

To estimate the temperature under the action of laser pulse, we have used laser parameters of our experimental system. In our case, $\tau = 1.2 \cdot 10^{-7}$ s, $a = 53$ μm and $\sqrt{4\kappa\tau}/a = 0.09 \ll 1$, so we can use 1D approximation.

Using expression (12), the rise of temperature of the molybdenum mirror evaluates as $T \approx E \cdot 6090$ K, and one can see that for $E = 1$ mJ (this corresponds to 11.33 J/cm² for $2a \approx 100$ μm spot diameter), the maximum temperature will be around 6363 K, which is sufficiently higher than the melting temperature. As the melting temperature of molybdenum is 2890 K, we can calculate the threshold laser pulse energy for one pulse heating, which is $E_{th} = 0.43$ mJ or $F_{th} = 4.87$ J/cm². As it was obtained in previous section, this threshold increases to 6.67 J/cm², if we take into account temperature dependence of surface absorptance.

Using the stainless steel features presented in **Appendix A**, the temperature rise in the center of the spot at the end of the laser pulse can be computed to be $T = E \cdot 13 \cdot 10^3$ K, where E is expressed in mJ. This value exceeds the one for

molybdenum mirrors because the thermal conductivity of stainless steel is much smaller than the one of molybdenum. These estimations clearly explain the observed ablation of surface on the stainless steel mirror during experimental studies. The damage threshold of stainless steel mirror equals to E_{th} = **0.105** mJ or F_{th} = **1.19** J/cm². Here we can't compute the damage threshold in the case of changing surface absorptance as there is no reliable data on the coefficient A_1 for stainless steel AISI 316L in the literature.

2.2.1 Multi-pulse damage

To describe the decrease in damage threshold under multiple pulses laser irradiation, the model of mechanical-fatigue degradation of substrate was proposed in [50–52]. It is supposed in this model that plastic slip deformation, which is accumulated on the surfaces under repeated irradiation, increases surface roughness and is followed by the increase of absorbed laser energy. The multiple pulse threshold depends on the single pulse threshold and the number of pulses as:

$$F_N = F_1 N^{s-1} \tag{33}$$

where N is number of pulses, F_N is the N-pulse threshold, F_1 is the single pulse threshold and s is the exponent specific to the material.

This model was already applied for investigation of multi-pulse molybdenum damage thresholds [53], [54] and the exponent s of accumulation curve was estimated as $s = 0.88 \pm 0.01$. With such value multi-pulse threshold for 5000 pulses (this value is typical for our set-up) will equal to F_N = 2.5 6 J/cm².

For stainless steel, multiple pulse threshold to a single pulse threshold ratio should equal to $F_N/F_1 = N^{s-1}$ = 0.2 7 and for our theoretical estimation of SS damage threshold F_1 = 1.1 9 J/cm², we obtain F_N = 0.3 3 J/cm².

2.2.2 Influence of phase transitions

If material in solid state undergoes the first-order phase transition at the temperature T_p, then this material absorbs some amount of energy and thermophysical properties of material change their values at that temperature. This phenomenon will influence heat conduction in the material and can change damage thresholds.

For molybdenum, there are no first order phase transitions up to the melting point. For stainless steel 316L, the first of transitions occurs only at ~1570 K (see Figure 16) and its latent heats aren't high enough to change strongly the damage

thresholds. So, the presence of phase transitions during stainless steel heating is neglected.

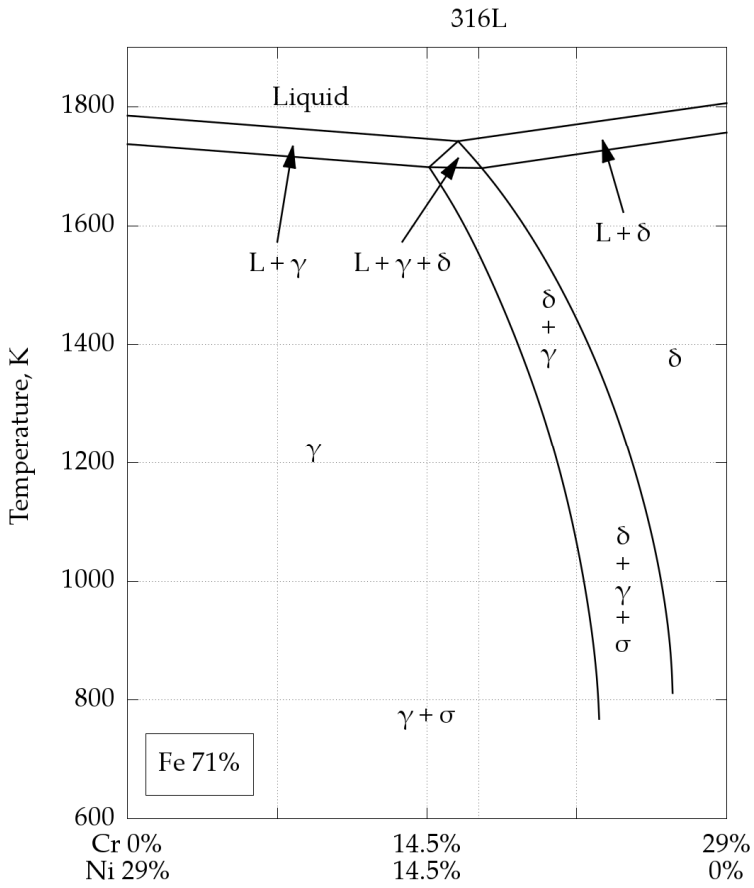

Figure 16: Phase diagram for stainless steel 316L.

Repetitive heating.

The calculated T_{max} for our materials and laser parameters are presented in the table below.

Table 1: Temperature rise and damage thresholds for long repetitive heating (20 kHz, 120 ns)

	Molybdenum	Stainless steel
T_{max}, for q_0 = 1 mJ	6164 K	14372 K
Damage threshold	0.425 mJ (4.82 J/cm²)	0.096 mJ (1.09 J/cm²)

We have calculated temperatures for molybdenum substrate after laser pulse with 1 mJ energy and 120 ns duration as the following:

Surface heating (3D)	6074 K
Volume heating (3D)	6036 K

We also have compared these results with those obtained by numerical calculations with LaserAblation software developed in LILM [41]. The obtained surface temperature was exactly the same as for the volume heating model.

The results of the surface temperature calculation as a function of time for 1 mJ laser pulse for molybdenum substrate are shown on Figure 17. The drop of heating temperature after 120 ns is caused by the end of the laser pulse. From the figure, for long pulse durations (>10 ns), the difference between surface and volume heating models is small enough (approximately 1%). But for short pulse durations (shorter than 0.5 ns), the error can be significant (see inset on Figure 17). The volume and surface heating models match well the numerical results.

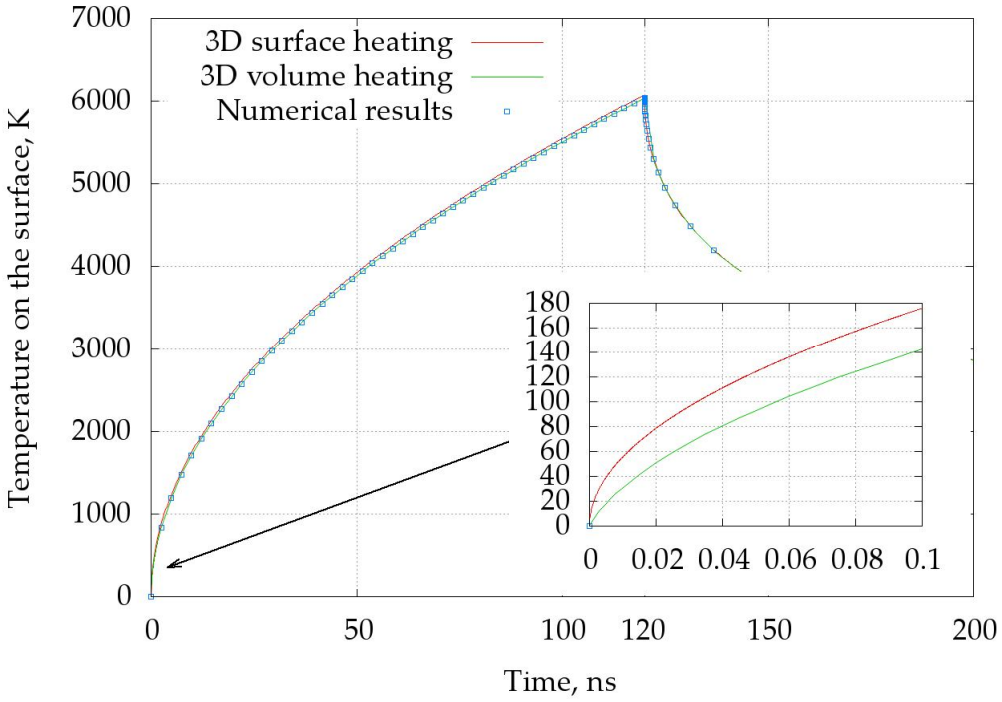

Figure 17: Comparison of volume and surface heating and numerical calculations models for molybdenum mirror.

2.3 Laser heating of a substrate with a layer

The problem of laser heating of semitransparent layers on the substrate is very important for laser cleaning and decontamination of surfaces with thin films. In LILM laboratory (CEA Saclay, France), the model to calculate heating temperature has been developed and applied for homogeneous layers of optical quality [41], [55].

However, real layers, which should be cleaned, are very inhomogeneous (for example, deposited layers on the plasma facing components in ITER and oxide layers with radioactive contamination). For such layers, the scattering of light should be included into the light propagation and heating models.

Here, we will present the model which includes the scattering of light in the layer. We suppose that partially collimated and partially diffuse light falls perpendicularly on the target with the layer. We present the solutions of the one-dimensional thermal conduction equation for a substrate with a layer in section 2.3.1. This solution depends on the heat sources caused by radiation absorption. In section 2.4, we use the four-flux theory to find the distribution of intensity in the target and calculate the heat sources in-depth distribution.

2.3.1 Temperature calculation

We will use the 1D approximation for the complete system of heat conduction equations [41], [55], [56]. Also we suppose the thermo-physical and optical features to be independent of temperature. Then, laser heating is described by following linear heat conduction equations:

$$\begin{cases} \dfrac{\partial T}{\partial} = \kappa_l \dfrac{\partial^2 T}{\partial z^2} + \dfrac{f_0}{\rho} q(z) f(t), & z < d \\ \dfrac{\partial T}{\partial} = \kappa_s \dfrac{\partial^2 T}{\partial z^2} + \dfrac{f_0}{\rho} q(z) f(t), & z > d \end{cases} \tag{34}$$

where d is the layer thickness, $\kappa = k/\rho c$ [m²/s] is the thermal diffusivity, k, c, ρ are the thermal conductivity, the heat capacity and the density of the matter, respectively, and the indexes l and s indicate the layer and the substrate, respectively. The second term of the right hand side contains the volumetric power of heat sources f_0 [W/m³] and functions $q(z)$ and $f(t)$, which describe the spatial and temporal distribution of heating sources in the target, respectively. Function $f(t)$ is the temporal shape of laser pulse.

We suppose that before the action of a single laser pulse, the target temperature is zero, hence, the initial condition is $T(z,\ t = 0) = 0$. The boundary conditions at the contact between the layer and the substrate take the form [42]:

$$-k_l \frac{\partial T}{\partial}\bigg|_{z=d-0} = -k_s \frac{\partial T}{\partial}\bigg|_{z=d+0} \equiv q_d \tag{35}$$

$$T(t, z = d - 0) - T(t, z = d + 0) = \frac{q_d}{h} \tag{36}$$

where h is a coefficient of surface heat transfer for the boundary between the layer and the substrate.

One more boundary condition implies the heat flux from the surface to be proportional to the temperature difference between the surface and the surrounding medium, so that it is given by:

$$k_l \frac{\partial T}{\partial z}\bigg|_{z=0} = \mu \left[T(t,0)\right. \tag{37}$$

where μ is a coefficient of surface heat transfer.

To nondimensionalize equations, it is necessary to replace the variables t and z with their scaled quantities:

$$\xi = \frac{t}{\tau_0}$$

$$\chi_d = \frac{d}{\sqrt{\kappa_l \tau_0}}$$

$$\chi = \begin{cases} \dfrac{z}{\sqrt{\kappa_l \tau_0}} & z < d \\ \dfrac{d}{\sqrt{\kappa_l \tau_0}} + \dfrac{z-d}{\sqrt{\kappa_s \tau_0}} & z > d \end{cases} \tag{38}$$

$$\theta = \frac{T}{T_0} \qquad T_0 = \begin{cases} \dfrac{f_0 \tau_0}{\rho_l c_l} & \chi < \chi_d \\ \dfrac{f_0 \tau_0}{\rho_s c_s} & \chi > \chi_d \end{cases}$$

Using this notation, the heat conduction problem simplifies to:

$$\frac{\partial \theta}{\partial \xi} = \frac{\partial^2 \theta}{\partial \chi^2} + q(\chi) f(\xi) \tag{39}$$

$$\frac{\partial \theta}{\partial \chi}\bigg|_{\chi=0} = \frac{\mu \sqrt{\kappa_l \tau_0}}{k_l} \theta(\xi, 0) \tag{40}$$

$$-\sqrt{\kappa_l \tau_0} \frac{\partial \theta}{\partial \chi}\bigg|_{\chi=\chi_d-0} = -\sqrt{\kappa_s \tau_0} \frac{\partial \theta}{\partial \chi}\bigg|_{\chi=\chi_d+0} \equiv \frac{q_d}{f_0} \tag{41}$$

$$\frac{\theta(\xi, \chi_d - 0)}{\rho_l c_l} - \frac{\theta(\xi, \chi_d + 0)}{\rho_s c_s} = \frac{q_d}{h f_0 \tau_0} \tag{42}$$

Using the method of separation variables [57], [58], we will search for the partial solution of homogeneous equation $\dot{\theta} = \theta'$ in the form:

$$\theta_\lambda(\xi, \chi) = e^{-\lambda^2 \xi} X_\lambda(\chi) \tag{43}$$

For simplicity, we will not consider the case of the completely imperfect heat contact between the substrate and the layer, so $h \to \infty$. Substituting the expression (43) into the equation (39) and boundary conditions (40)–(42), the following boundary problem for function $X_\lambda(\chi)$ can be obtained

$$X'_\lambda(\chi) = -\lambda^2 X_\lambda(\chi) \tag{44}$$

$$X'_\lambda(0) = \eta X_\lambda(0) \quad \text{where } \eta = \frac{\mu\sqrt{\kappa_l \tau_0}}{k_l} \tag{45}$$

$$\alpha \frac{\partial \theta}{\partial \chi}\bigg|_{\chi=\chi_d-0} = \frac{\partial \theta}{\partial \chi}\bigg|_{\chi=\chi_d+0} \quad \text{where } \alpha = \sqrt{\frac{\kappa_l}{\kappa_s}} \tag{46}$$

$$\begin{gathered}\beta\,\theta(\xi, \chi_d - 0) - \theta(\xi, \chi_d + 0) = -g \frac{\partial \theta}{\partial \chi}\bigg|_{\chi=\chi_d+0} \\ \text{where } \beta = \frac{\rho_s c_s}{\rho_l c_l}, g = \frac{\rho_s c_s \sqrt{\kappa_s}}{h\sqrt{\tau_0}}\end{gathered} \tag{47}$$

The orthogonality condition for the eigenfunctions is written as follows

$$\int_0^\infty w(\chi) X_\lambda(\chi) X_{\lambda'}(\chi)\, d\chi = \frac{\pi}{2}\left(\delta(\lambda + \lambda') + \delta(\lambda - \lambda')\right) \tag{48}$$

$$w(\chi) = \begin{cases} \alpha & \chi < \chi_d \\ 1 & \chi > \chi_d \end{cases} \tag{49}$$

The solution of this problem is

$$\boxed{X_\lambda(\chi) = \begin{cases} \dfrac{\lambda \cos\lambda\chi + \eta \sin\lambda\chi}{\sqrt{c^2(\lambda) + d^2(\lambda)}} & \chi < \chi_d \\ \dfrac{c(\lambda)\cos\lambda\chi + d(\lambda)\sin\lambda\chi}{\sqrt{c^2(\lambda) + d^2(\lambda)}} & \chi > \chi_d \end{cases}} \tag{50}$$

$$\begin{aligned} c(\lambda) &= \alpha(g\cos\lambda\chi_d - \sin\lambda\chi_d)(\eta\cos\lambda\chi_d - \lambda\sin\lambda\chi_d) + \beta\cos\lambda\chi_d(\eta\sin\lambda\chi_d + \lambda\cos\lambda\chi \\ d(\lambda) &= \alpha(g\sin\lambda\chi_d + \cos\lambda\chi_d)(\eta\cos\lambda\chi_d - \lambda\sin\lambda\chi_d) + \beta\sin\lambda\chi_d(\eta\sin\lambda\chi_d + \lambda\cos\lambda\chi \end{aligned} \tag{51}$$

The solution $\theta(\xi, \chi)$ of inhomogeneous heat conduction equation can be written in a form of decomposition into functions $X_\lambda(\chi)$

$$\theta(\xi, \chi) = \int_0^\infty \Theta(\xi, \lambda) X_\lambda(\chi)\, d\lambda \tag{52}$$

Here functions $\Theta(\xi, \lambda)$ are the coefficients of the decomposition. Substituting this expression into the equation (39), we obtain

$$\int_0^\infty \frac{\partial \Theta(\xi,\lambda)}{\partial \xi} X_\lambda(\chi)\, d\chi = \int_0^\infty \Theta(\xi,\lambda) X'_\lambda(\chi)\, d\chi + q(\chi) f(\xi) \tag{53}$$

Applying integrating operator $\int_0^\infty \cdot\, X_{\lambda'}(\chi) d\chi$ and taking into account (44) and (48), one obtains:

$$\dot{\Theta}(\xi,\lambda) = -\lambda^2 \Theta(\xi,\lambda) + Q(\lambda) f(\xi) \tag{54}$$

$$\boxed{Q(\lambda) = \frac{2}{\pi} \int_0^\infty w(\chi) q(\chi) X_\lambda(\chi)\, d\chi} \tag{55}$$

The solution of the equation $y' + f(x)y = g(x)$ passing an arbitrary point (ξ, η) is [59]:

$$y = e^{-F}\left(\eta + \int_\xi^x g(x) e^F\, dx\right) \quad \text{where } F(x) = \int_\xi^x f(x)\, dx \tag{56}$$

In our case, we obtain:

$$\Theta(\xi,\lambda) = Q(\lambda) F_\lambda(\xi) \tag{57}$$

$$\boxed{F_\lambda(\xi) = \int_0^\xi f(\xi') \exp\left(\lambda^2(\xi' - \xi)\right) d\xi'} \tag{58}$$

Thus, the final solution is:

$$\boxed{\theta(\xi,\chi) = \int_0^\infty X_\lambda(\chi) Q(\lambda) F_\lambda(\xi) d\lambda} \tag{59}$$

We have obtained the expression that could be applied for laser heating temperatures calculation for the target consisting of a bulk substrate and a layer of constant thickness.

For certain cases, some of the quantities defined by integrals can be expressed as simple analytical expressions. For **surface heating**, the distribution of heat sources is described by the Dirac function, so $q(\chi) = \delta(\chi)$. For the case of the **thermo-isolated surface** and the **completely perfect heat contact** between the layer and the substrate, substituting $q(\chi)$ into (55), we obtain:

$$Q(\lambda) = \frac{2\alpha_l}{\pi\sqrt{\alpha^2 \sin^2 \lambda\chi_d + \beta^2 \cos^2 \lambda\chi_d}} \tag{60}$$

If we are at the time which is much longer than pulse duration, the actual laser pulse can be replaced by the **Dirac pulse** $f(\xi) = \delta(\xi)$. With this approximation, we have:

$$F_\lambda(\xi) = e^{-\lambda^2 \xi} \tag{61}$$

In the case of **constant heating** $f(\xi) = 1$, so:

$$F_\lambda(\xi) = \frac{1 - \mathrm{e}\ \mathrm{x}\left(-\lambda^2 \xi\right)}{\lambda^2} \tag{62}$$

2.4 In-depth heat sources distribution

In the above section, we have obtained the solution by quadratures of heat conduction equation for substrate-layer structure for the case of general heat sources specified by functions $f(t)$ and $q(z)$. It will be recalled that f(t) describes the temporal behaviour of heating sources and $q(z)$ describes their in-depth distribution. While $f(t)$ can be easily determined by measuring laser pulse temporal profile, direct measurements of $q(z)$ are impossible, and it is necessary to apply the adequate model for its calculation.

Usually, to take into account in-depth distribution of light intensity in a solid body, the intensity is supposed to decay exponentially according to the Beer-Lambert law. This model is applicable when the target has no layer or if the thickness of a layer is much higher than the light absorption length $1/\alpha$.

If the thickness of the layer on the target surface is not high, one should take into account the reflection of light at the substrate-layer interface. For incoherent light, the intensity in the layer can be determined as a sum of intensities of waves propagating back and forth due to the reflection at the layer boundaries.

As laser light is coherent, the interference effects have to be taken into account. Laser radiation can be considered completely coherent if its coherence length l_c is much greater than the optical thickness nd of the layer and than the total absorption length for light circulating in the layer, i.e. if

$$l_c = \frac{\lambda^2}{\Delta\lambda} \gg n \qquad l_c \gg \left(\alpha - \frac{1}{d} 1 \quad \sqrt{R_1 R_2}\right)^{-1} \tag{63}$$

where R_1 and R_2 are reflection coefficients at the layer boundaries. For example, the pulsed ytterbium fiber laser IPG YLP-1/120/20 produces the light at $\lambda = 1.064$ μm

with the spectral width of $\Delta\lambda = 3$ nm[1]. Then, the coherence length equals to $l_c = \lambda^2/\Delta\lambda \approx 3\ 3$ μm, and for the layers of the optical thickness nd much lower than l_c, the light should be considered as coherent. This case was studied in [41], where the expressions for in-depth intensity distribution were established.

When the layer is not homogeneous, the scattering of light should be also considered. We can replace our inhomogeneous layer with a homogenous one with some scattering coefficient and average properties. Conventionally, to consider such a case, the radiation transfer theory and four-flux model [60–63] is applied. This model does not take into account any interference effects and, hence, should be applied only for scattering substrates or very thick scattering layers (when coherent radiation does not reach the interface between the layer and the substrate). The model of paint ablation was developed in CEA Saclay on the basis of this model in [64], [65]. In this work, we will further improve the model of light propagation by combining the four-flux model and the model of homogeneous layer with interference.

In the following consideration, a 1D model of light propagation will be applied. This approximation is valid when the laser beam radius w_0 is much bigger than the layer thickness d and the light wavelength λ in the layer, $w_0 \gg d, \lambda$. These relations lead to a condition that the layer thickness is much lower than the Rayleigh length of laser beam: $d \ll l_R = n\ \pi w_0^2/\lambda_0$. For convergent or divergent beam, relative variation of beam size on the layer thickness should be much lower than the beam size: d t a $\vartheta \ll w_0$, where ϑ is the angle of the beam in the layer. When these conditions are met, the beam can be considered as a plane wave incident on the layer surface.

First, the expression for heat sources $q(z)$ will be derived. Then, the general expression for light intensity and associated heat sources are obtained. And then; the model is compared with the special cases.

2.4.1 Expression for heat sources

Let's consider a plane monochromatic electromagnetic wave. The field of the wave is:

$$\boldsymbol{E} = \boldsymbol{E}_0 \mathrm{c}\ \mathrm{o}(-\omega\ + \boldsymbol{k}\ + \phi) \tag{64}$$

It is useful to use exponential form instead of trigonometric one:

$$\widehat{\boldsymbol{E}} = \widehat{\boldsymbol{E}}_0 e^{-i\ \omega + i\boldsymbol{k}\ + i} \tag{65}$$

[1] YPL series spec. http://www.ipgphotonics.com/Collateral/Documents/English-US/YLP_Series.pdf

To obtain real vector, it is necessary to use expression:

$$\frac{1}{2}\left(\widehat{\boldsymbol{E}} + \widehat{\boldsymbol{E}}^*\right) \tag{66}$$

By definition, the intensity of an electromagnetic wave is the time-averaged magnitude of the Poynting vector [66]:

$$I = |\langle \boldsymbol{S} \rangle| \tag{67}$$

The Poynting vector of an electromagnetic field is defined as (in the Gaussian units):

$$\boldsymbol{S} = \frac{c}{4\pi}[\boldsymbol{E}, \boldsymbol{H}] \tag{68}$$

For plane monochromatic wave in a matter (including absorbing matter), the following condition between the electric and magnetic fields is satisfied (in the Gaussian units) [66]:

$$\boldsymbol{H} = \sqrt{\frac{\varepsilon}{\mu}}[\boldsymbol{l}, \boldsymbol{E}] \tag{69}$$

Here, ε and μ are the dielectric and magnetic permeabilities of the matter (in case of absorbing matter, they are complex), $\boldsymbol{l}$ is the wave propagation vector[1].

To compute (68), the field should be expressed in a real form. Hence, for a monochromatic electromagnetic wave, we obtain:

$$\boldsymbol{S} = \frac{c}{1\ \pi}[\boldsymbol{E} + \boldsymbol{E}^*, \boldsymbol{H} + \boldsymbol{H}^*] = \frac{c}{1\ \pi}([\boldsymbol{E}, \boldsymbol{H}^*] + [\boldsymbol{E}^*, \boldsymbol{H}]) \tag{70}$$

In this expression, the terms $[\boldsymbol{E}, \boldsymbol{H}]$ and $[\boldsymbol{E}^*, \boldsymbol{H}^*]$ are omitted as in following averaging over time they give zero.

Using the expression (69) and the following property of vector multiplication

$$\left[\boldsymbol{a}, [\boldsymbol{b}, \boldsymbol{c}]\right] = \boldsymbol{b}(\boldsymbol{a}, \boldsymbol{c}) - \boldsymbol{c}(\boldsymbol{a}, \boldsymbol{b}) \tag{71}$$

and the property that for plane electromagnetic wave $\boldsymbol{l} \perp \boldsymbol{E}$, we obtain:

$$[\boldsymbol{E}^*, \boldsymbol{H}] = \sqrt{\frac{\varepsilon}{\mu}}\left[\boldsymbol{E}^*, [\boldsymbol{l}, \boldsymbol{E}]\right] = \sqrt{\frac{\varepsilon}{\mu}}\left(\boldsymbol{l}(\boldsymbol{E}^*, \boldsymbol{E}) - \boldsymbol{E}(\boldsymbol{E}^*, \boldsymbol{l})\right) = \boldsymbol{l}\sqrt{\frac{\varepsilon}{\mu}}|\boldsymbol{E}|^2 \tag{72}$$

$$\boldsymbol{S} = \frac{c}{8\pi}\Re\sqrt{\frac{\varepsilon}{\mu}}|\boldsymbol{E}|^2\boldsymbol{l} \tag{73}$$

[1] In the case of a transparent medium, $\boldsymbol{k}$ is real and $\boldsymbol{k} \parallel \boldsymbol{l}$. In the case of an absorbing medium, the vector $\widehat{\boldsymbol{k}} = \boldsymbol{k}' + \boldsymbol{k}''$ is complex and if $\boldsymbol{k}'$ and $\boldsymbol{k}''$ are codirectional, then $\widehat{\boldsymbol{k}} \parallel \boldsymbol{l}$.

$$I = \frac{c}{8\pi}\Re\sqrt{\frac{\varepsilon}{\mu}}|\boldsymbol{E}|^2 \tag{74}$$

Here, we use $\Re$ and $\Im$ to denote the real and imaginary parts of complex number, respectively.

In case of non-magnetic medium, we have $\mu = 1$, and taking into account that in this case $\Re\sqrt{\frac{\varepsilon}{\mu}} = \Re\sqrt{\varepsilon} = n$, we get:

$$I = \frac{c}{8\pi}|\boldsymbol{E}|^2 \tag{75}$$

In accordance with [66], the power of heat sources $q(z)$ related to the radiation absorption of monochromatic wave can be found as:

$$q = \langle -\nabla \boldsymbol{S} \rangle \tag{76}$$

Further analysis leads to [66]:

$$q = \frac{\omega}{8\pi}\left(\Im\varepsilon|\boldsymbol{E}|^2 + \Im\mu|\boldsymbol{H}|^2\right) \tag{77}$$

In case of non-magnetic, medium second term is zero, and using (75), we get:

$$q = \frac{\omega\Im\varepsilon}{8\pi}|\boldsymbol{E}|^2 = \frac{\omega\Im\varepsilon}{n}I \tag{78}$$

Expression (78) can be reduced taking into account that $\omega\, c = 2\pi\lambda_0$ and $\Im\varepsilon = \Im\hat{n}^2 = 2n\,\varkappa$ where quantities n and $\varkappa$ are real and imaginary parts of complex refractive index $\hat{n}$. In this case, we obtain:

$$q = \frac{2\pi}{\lambda_0}\frac{2n\,\varkappa}{n}I = \frac{4\pi\,\varkappa}{\lambda_0}I = \alpha \tag{79}$$

This means that the spatial distribution of heat sources is proportional to the light intensity.

All these expressions are written in the Gaussian unit system. Expressions (68), (75) and (78) in SI unit system will look as:

$$\boldsymbol{S} = [\boldsymbol{E}, \boldsymbol{H}]$$

$$I = \frac{c\,n\varepsilon_0}{2}|\boldsymbol{E}|^2 \tag{80}$$

$$q = \frac{\omega\Im\varepsilon\varepsilon_0}{2}|\boldsymbol{E}|^2 = \frac{\omega\Im\varepsilon}{n}I$$

2.4.2 Light propagation model

Now let's consider the coherent laser beam directed perpendicularly on the layer/substrate system. The amplitude and intensity of the incident wave on the layer at the point $z = 0 - 0$ are E_0 and I_0, respectively. They are related by the expression (75).

The radiation field in the layer can be decomposed into two parts: the coherent one, which interferes due to the multiple reflections on the layer boundaries and the diffuse (scattered) one.

The layer is characterized by the complex index of refraction $\widehat{n}_1 = n_1 + i\varkappa_1$ and the scattering coefficient β. Optical properties of the substrate are characterized by the complex index of refraction $\widehat{n}_2 = n_2 + i\varkappa_2$. It is supposed that there is no scattering in the substrate.

The boundaries of the layer are characterized by reflection and transmission coefficients. The applied notation is the following:

- The amplitude and intensity reflection coefficients are designated by r and R respectively. The amplitude and intensity transmission coefficient are designated by τ and T, respectively.
- Indexes c and d indicate the reflection coefficient for collimated or diffuse fluxes, respectively.
- Indexes 0, 1 and 2 indicate the vacuum, the layer and the substrate, respectively. For example, the value $r_{1\,2}$ indicates the amplitude reflection coefficient for the light travelling from the layer to the substrate, the value $T_{1\,0}$ indicates the intensity transmission coefficient for the light travelling from the layer to the vacuum.
- Indexes (+) and (−) indicate the direction of propagation of light, for which the reflection coefficient is computed. The expressions of reflection coefficient are presented in section 2.5.

Now we will find coherent part $I_c(z)$ and diffuse part $I_d(z)$ of the intensity distribution in the layer.

Coherent part. The field at the point z is:

$$E_c(z<d) = E_0\tau_0\left(e^{i\widehat{k}_1 z} + \tau r_1\, e^{i\widehat{k}_1(d-z)} + \tau^2 r_1\, r_1\, e^{i\widehat{k}_1 z} + \tau^3 r_1\, r_1^2\, e^{i\widehat{k}_1(d-z)} + \right.$$
$$\left. + \tau^4 r_1^2\, r_1^2\, e^{i\widehat{k}_1 z} + \cdots\right) =$$
$$= E_0\tau_0\left\{e^{i\widehat{k}_1 z}\left(1 + r_1\, r_1\, \tau^2 + \cdots\right) + \tau r_1\, e^{i\widehat{k}_1(d-z)}\left(1 + r_1\, r_1\, \tau^2 + \cdots\right)\right\} = \quad (81)$$
$$= E_0\tau_0\,\frac{e^{i\widehat{k}_1 z} + \tau r_1\, e^{i\widehat{k}_1(d-z)}}{1 - r_1\, r_1\, \tau^2}$$

$$E_c(z>d) = E_0\tau_0\left(\tau\tau_1\, e^{i\widehat{k}_2(z-d)} + \tau^3\tau_1\, r_1\, r_1\, e^{i\widehat{k}_2(z-d)} + \cdots\right) =$$
$$= E_0\tau_0\,\tau\tau_1\, e^{i\widehat{k}_2(z-d)}\left(1 + r_1\, r_1\, \tau^2 + \cdots\right) = \frac{E_0\tau\tau_0\,\tau_1\, e^{i\widehat{k}_2(z-d)}}{1 - r_1\, r_1\, \tau^2} \quad (82)$$

where $\widehat{k}_1 = 2\pi/\lambda_0\left(n_1 + i(\varkappa_1 + \tilde{\varkappa}_1)\right)$ is a complex wave number of the wave in the layer, $\widehat{k}_2 = 2\pi\widehat{n}_2/\lambda_0$ is the complex wave number in the substrate, $\tilde{\varkappa}_1 = \beta\lambda_0/4\pi$ is the efficient extinction coefficient caused by coherent light scattering and $\tau = e^{i\widehat{k}_1 d}$ is the complex transmission coefficient through the layer.

Using these expressions with (75), the intensities for coherent part of the laser radiation can be obtained as:

$$I_c(z<d) = n_1 I_0\left|\frac{\tau_0\left(e^{i\widehat{k}_1 z} + \tau r_1\, e^{i\widehat{k}_1(d-z)}\right)}{1 - r_1\, r_1\, \tau^2}\right|^2 \quad (83)$$

$$I_c(z>d) = n_2 I_0\left|\frac{\tau\tau_0\,\tau_1\, e^{i\widehat{k}_2(z-d)}}{1 - r_1\, r_{12}\tau^2}\right|^2 \quad (84)$$

Full reflection coefficient for coherent radiation from the layer/substrate structure equals to [67]:

$$R = |r|^2 \quad r = \frac{r_0 + r_1\,\tau^2}{1 + r_0\, r_1\,\tau^2} \quad (85)$$

The power of heat sources induced by coherent part is $q(z) = \alpha_1 I_c$. The second part $\beta_1 I_c$ is scattered into diffuse light.

Incoherent part. To obtain the intensity distribution for incoherent part of radiation, we apply the four-flux model [60–63].

Radiative flux or radiative flux density is the amount of radiative energy moving through the unit area per second in all directions. It is related with intensity as [68]:

$$F = \int I(\vartheta, \varphi) \cos\vartheta \, d\omega \tag{86}$$

For our case, when the radiation propagates only to one hemisphere and has the azimuthal symmetry, this equals to:

$$F = 2\pi \int_0^{\pi/2} I(\vartheta) \cos\vartheta \sin\vartheta \, d\vartheta \tag{87}$$

which for isotropic diffuse light reduces simply to $F = \pi I$ and for collimated light to $F = I$.

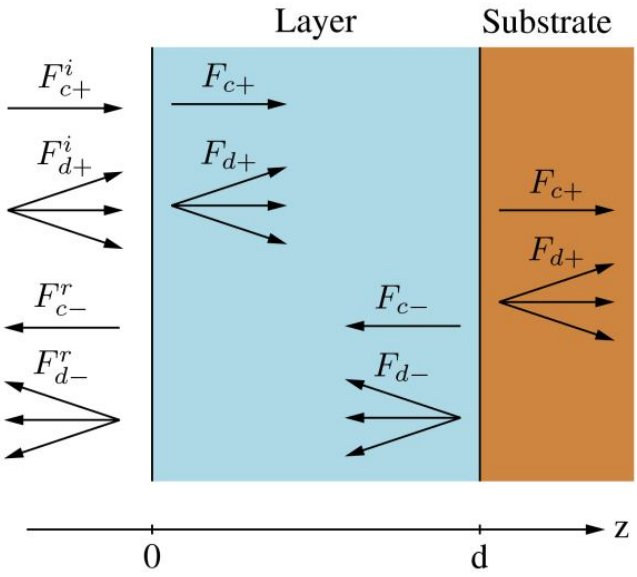

Figure 18: Graphical presentation of the four-flux model.

Within the four-flux model, the whole radiation field is divided into four fluxes: two collimated fluxes F_c^+ and F_c^- propagating in positive and negative directions, respectively, and two diffuse fluxes F_d^+ and F_d^- (see Figure 18). The medium is characterized by the absorption coefficient[1] α, the scattering coefficient β and the forward scattering ratio σ, which equals to the energy scattered in the forward hemisphere over the total scattered energy. The average path-length parameter ξ is introduced in the model to take into account the different path lengths of diffuse radiation compared with that of collimated radiation. For semi-isotropic diffuse light $\xi = 2$ [69]. One should note that this parameter affects also the expression for heat sources and leads to the relation $q(z) = \alpha \xi F_d(z)$.

[1] Here and further we will omit the index l to describe the characteristics of the layer if this does not lead to an ambiguity.

We assume that the forward scattering ratio is the same for collimated and diffuse light. This assumption is perfect in two limiting cases of isotropic scattering and of completely forward-throwing scattering.

In our model, we cannot divide coherent radiation field into positively and negatively directed fluxes because of interference. We suppose that scattering is isotropic, i.e. $\sigma = ½$ and $\xi = 2$. The solution for collimated part is given by expressions (83) and (84). The part of coherent intensity, which is scattered, equals to $\beta_1 I_c$. The energy balance equations for diffuse fluxes are the following:

$$\begin{aligned} \frac{dF_d^+}{d} &= -2\alpha F_d^+ - \beta F_d^+ + \beta F_d^- + \frac{\beta I_c}{2} \\ \frac{dF_d^-}{d} &= 2\alpha F_d^- + \beta F_d^- - \beta F_d^+ - \frac{\beta I_c}{2} \end{aligned} \tag{88}$$

with the following boundary conditions:

$$\begin{aligned} F_d^+ &= R_{d1}^- F_d^- \quad z = 0 \\ F_d^- &= R_{d2}^+ F_d^+ \quad z = d \end{aligned} \tag{89}$$

To solve system (88) with the boundary conditions (89), we introduce the following notation:

$$\begin{aligned} y_1 &= F_d^+ & y_2 &= F_d^- \\ a &= 2\alpha + \beta & f(z) &= \frac{\beta I_c(z)}{2} \\ r_1 &= R_{d1}^- & r_2 &= R_{d2}^+ \end{aligned} \tag{90}$$

Then, our system takes the form:

$$\begin{cases} y_1' = -a y_1 + \beta y_2 + f(z) \\ y_2' = -\beta y_1 + a y_2 - f(z) \end{cases} \tag{91}$$

with the boundary conditions:

$$\begin{aligned} y_1 &= r_1 y_2 \quad \text{at } z = 0 \\ y_2 &= r_2 y_1 \quad \text{at } z = d \end{aligned} \tag{92}$$

The homogeneous system $\boldsymbol{y}' = \boldsymbol{A}\,\boldsymbol{y}$ where $\boldsymbol{y} = (y_1, y_2)$ and $\boldsymbol{A} = \begin{pmatrix} -a & \beta \\ -\beta & a \end{pmatrix}$ has the eigenvalues $\lambda_{1,2} = \pm\sqrt{a^2 - \beta^2}$ and the general solution is:

$$\boldsymbol{y}^h = c_1 e^{\lambda_1 z} \boldsymbol{e}_1 + c_2 e^{\lambda_2 z} \boldsymbol{e}_2 \tag{93}$$

where $\boldsymbol{e}_1, \boldsymbol{e}_2$ are the eigenvectors:

$$\boldsymbol{e}_1 = \begin{pmatrix} \beta \\ a + \sqrt{a^2 - \beta^2} \end{pmatrix} \quad \boldsymbol{e}_2 = \begin{pmatrix} \beta \\ a - \sqrt{a^2 - \beta^2} \end{pmatrix} \tag{94}$$

The general solution of the inhomogeneous system $\boldsymbol{y}' = \boldsymbol{A}\,\boldsymbol{y} + \boldsymbol{f}$ is the sum of the general solution of homogeneous system and a partial solution of the inhomogeneous system: $\boldsymbol{y} = \boldsymbol{y}^h + \boldsymbol{y}^i$.[n]

To find the solution of the boundary value problem, we act as follows:

1. We find a partial solution of the inhomogeneous system with special initial conditions $y_1 = 0, y_2 = 0$. The solution is obtained numerically using the Runge-Kutta method.
2. Now we know the general solution, which depends on two constants c_1 and c_2.
3. The constants can be found using two boundary conditions (92).

For numerical solution of inhomogeneous system (91), GNU Scientific Library [70] implementation of the embedded Runge-Kutta-Fehlberg (4, 5) method [71] was used.

The equations on c_1 and c_2 write as:

$$\begin{gathered} c_1 \underbrace{\left(r_1\left(a+\sqrt{a^2-\beta^2}\right)-\beta\right)}_{a_{1\,1}} + c_2 \underbrace{\left(r_1\left(a-\sqrt{a^2-\beta^2}\right)-\beta\right)}_{a_{1\,2}} = 0 \\ c_1 \underbrace{\left(e^{\sqrt{a^2-\beta^2}d}\left(a+\sqrt{a^2-\beta^2}-r_2\beta\right)\right)}_{a_2} + c_2 \underbrace{\left(e^{-\sqrt{a^2-\beta^2}d}\left(a-\sqrt{a^2-\beta^2}-r_2\beta\right)\right)}_{a_2} = \tilde{c} \end{gathered} \tag{95}$$

where $\tilde{c} = r_2 y_1^i(d) - y_2^i(d)$.

And the solution is:

$$c_1 = \frac{-a_1\ \tilde{c}}{a_1\ a_2\ - a_1\ a_2} \quad c_2 = \frac{a_1\ \tilde{c}}{a_1\ a_2\ - a_1\ a_2} \tag{96}$$

Now when the intensity of coherent light and fluxes of diffuse light are found, the heat sources can be expressed as

$$q(z) = \alpha I_c(z) + \xi\ \left(F_d^+(z) + F_d^-(z)\right) \tag{97}$$

To study the influence of scattering coefficient on the intensity distribution in the layer, a series of calculation were performed for different β. The parameters applied for calculation are presented in Table 2.

Table 2: Parameters of the substrate and the layer used in calculations

	Layer	Substrate
Matter	H/C mixture (DLC+H)	Molybdenum
Reflection coefficient	0.1	0.69

Absorption coefficient	0.2 μm^{-1}	55 μm^{-1}
Thickness	10 μm	

The results of calculation are presented on Figure 19. One can see that with increasing in scattering coefficient β, the intensity oscillations caused by the interference are decreasing. It happens because the coherent laser beam attenuates with a coefficient $\alpha_1 + \beta_1$.

The second conclusion that can be made from these results is that radiation tends to be confined near the surface with increasing in β.

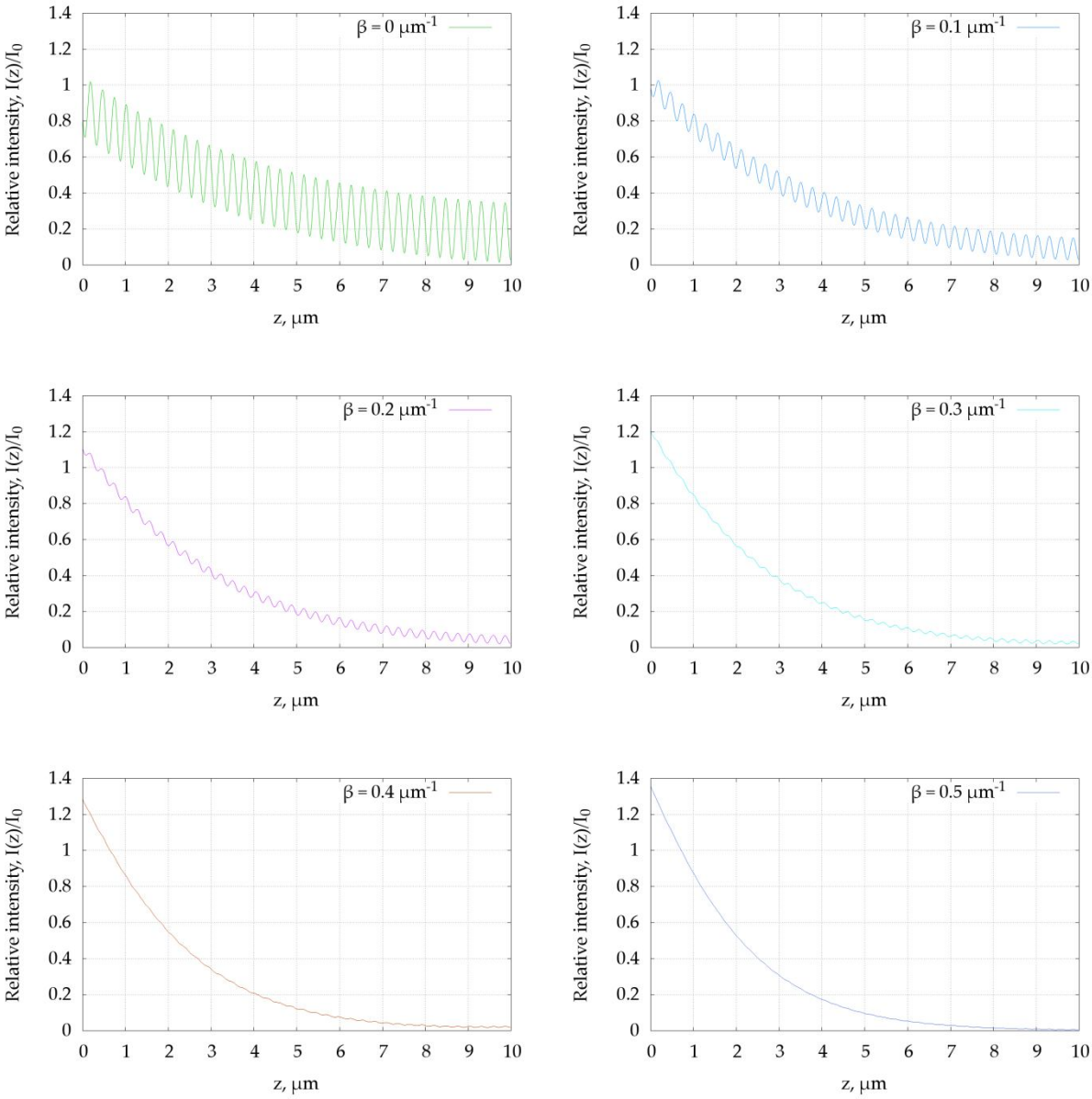

Figure 19: Total flux distribution in the layer for different values of scattering coefficient.

On Figure 20, the calculated total reflection coefficient for the layer/metal system is presented as a function of the layer thickness for three different values of scattering coefficient β. While the reflection coefficient is highly oscillating for a layer without scattering, these oscillations decrease with increasing β.

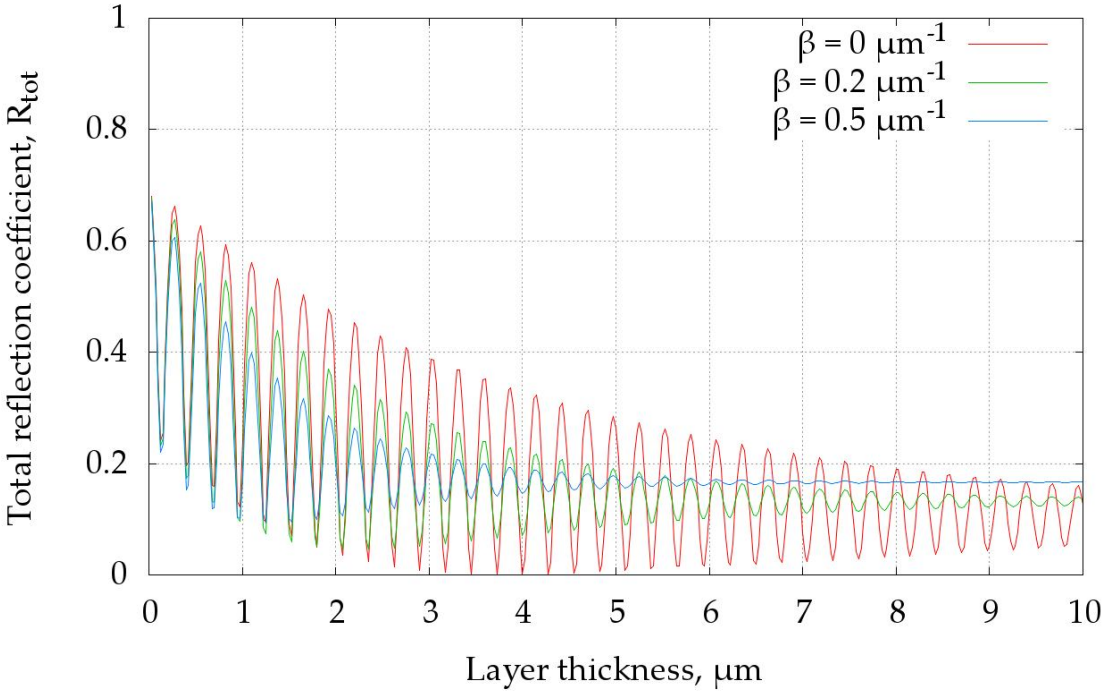

Figure 20: Reflection coefficient as a function of layer thickness. Reflection coefficient for metal surface without layer is R = 0.69.

2.4.3 Limiting cases

To validate our model, we will compare it with two limiting cases having analytical solution: coherent light model ($\beta = 0$) and incoherent three-flux model ($\alpha + \beta \gg 1/d$).

In the case when β equals to zero, there is no scattering in the layer and diffuse fluxes disappear. Then, the intensity of coherent light will be:

$$I_c(z < d) = n_1 I_0 \left| \frac{\tau_0 \left(e^{i\hat{k}_1 z} + \tau r_1 \, e^{i\hat{k}_1 (d-z)} \right)}{1 - r_1 \, r_1 \, \tau^2} \right|^2 \tag{98}$$

$$I_c(z > d) = n_2 I_0 \left| \frac{\tau \tau_0 \, \tau_1 \, e^{i\hat{k}_2 (z-d)}}{1 - r_1 \, r_1 \, \tau^2} \right|^2 \tag{99}$$

where $\tau = e^{i\hat{k}_1 d}$ is the complex transmission coefficient through the layer and the wave number $\hat{k}_i = 2\pi\hat{n}_i/\lambda_0$, $i = 1,2$. These expressions are in agreement with those obtained in [55].

Full reflection coefficient from the layer/substrate structure equals to [67]:

$$R = |r|^2 \quad r = \frac{r_0 + r_1 \tau^2}{1 + r_0 r_1 \tau^2} \tag{100}$$

In the case when β is high, so that $\alpha + \beta \gg 1/d$, the coherent part almost completely decays in the layer and the model transforms to the model of three fluxes developed earlier in [64], [65].

On Figure 21, the in-depth distribution of total intensity is presented for the coherent model with scattering (indicated by solid lines) and for two limiting cases: for the model without scattering and for the three-flux model (indicated by points). The parameters used in calculations are presented in Table 2. From this comparison, we can conclude that the developed model converges to the known cases as it was expected.

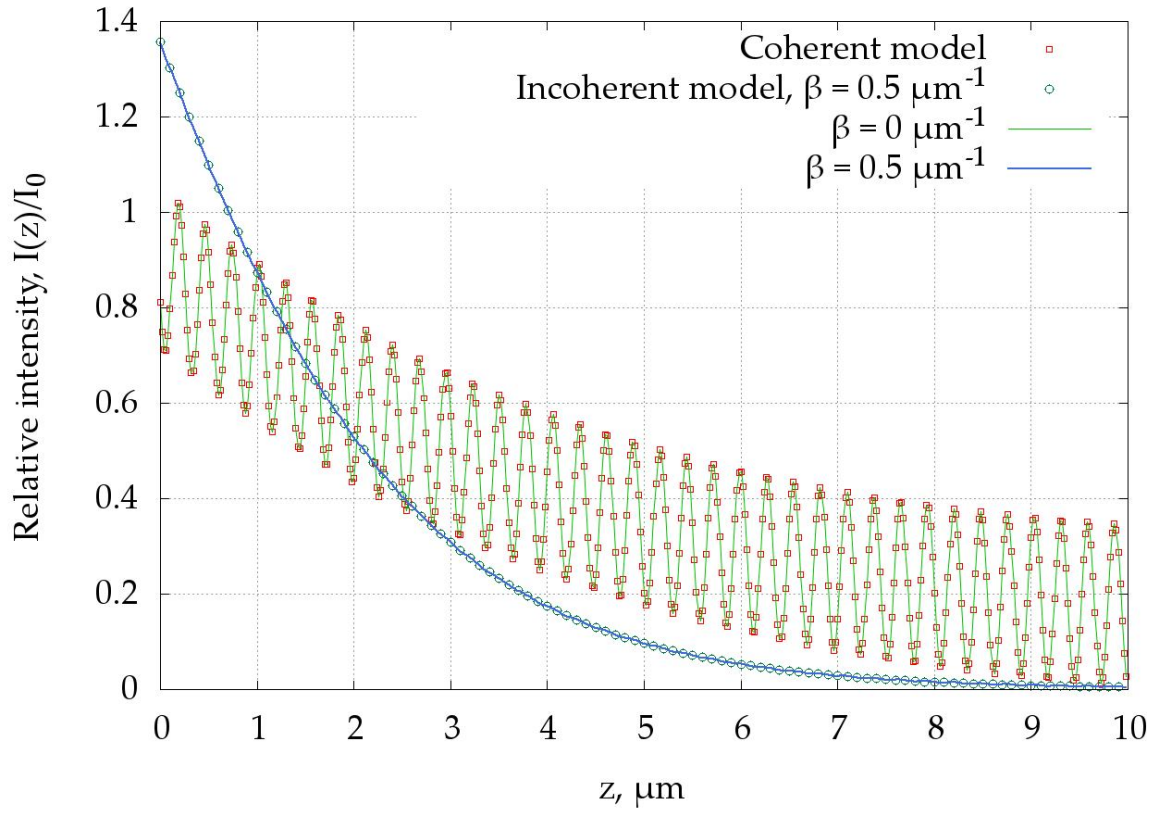

Figure 21: Comparison of in-depth intensity distribution obtained with developed model and with two known models (pure coherent [55] and three-flux models [65])

2.5 Reflection coefficients

In the section above, we have obtained the expressions for heat sources in-depth distribution supposing the reflection coefficients to be known. The reflection coefficient for collimated and diffuse light will be derived in this section.

2.5.1 Collimated light

For plane homogeneous wave propagating perpendicularly to the boundary, the Fresnel reflection coefficient for any polarization is [66]:

$$R_{c\perp} = \left|\frac{\hat{n}_1 - \hat{n}_2}{\hat{n}_1 + \hat{n}_2}\right|^2 \tag{101}$$

Here, $\hat{n}_1$ and $\hat{n}_2$ are complex refractive indexes of the first medium (layer with incident and reflected waves) and the second medium (substrate with transmitted wave), respectively.

The derivation for oblique incidence is done primarily according to [72]. In the general case of inhomogeneous wave[1], the wave vector equals to:

$$\hat{\boldsymbol{k}} = \hat{n}k_0\hat{\boldsymbol{g}} \tag{102}$$

where $k_0 = w/c$ and $\hat{\boldsymbol{g}}$ is a complex vector satisfying $\hat{\boldsymbol{g}} \cdot \hat{\boldsymbol{g}} = 1$. The vector $\hat{\boldsymbol{g}}$ can be defined with the inhomogeneity parameter β and two real perpendicular unit vectors $\boldsymbol{g}_\parallel$ and $\boldsymbol{g}_\perp$:

$$\hat{\boldsymbol{g}} = \boldsymbol{g}_\parallel \cos\beta + i\boldsymbol{g}_\perp \sin\beta \tag{103}$$

Using the vector $\boldsymbol{g}_\parallel$, the right-handed coordinate system $(\boldsymbol{e}_1, \boldsymbol{e}_2, \boldsymbol{g}_\parallel)$ of the wave can be constructed with the rule that vector $\boldsymbol{e}_1$ is always codirectional with $[\boldsymbol{s}, \boldsymbol{g}_\parallel]$, where $\boldsymbol{s}$ is the unit normal to the boundary. With this right-handed coordinate system, we can define angle ψ that indicates the direction of inhomogenity of the wave as:

$$\boldsymbol{g}_\perp = \boldsymbol{e}_1 \cos\psi + \boldsymbol{e}_2 \sin\psi \tag{104}$$

To calculate reflection coefficient for oblique incident, we suppose that incident wave is homogeneous (that is, the inhomogeneity parameter for incident wave $\beta_i = 0$, the real and imaginary parts of wave vector are codirectional). In the case when vector $\boldsymbol{g}_\perp^i$ lies in the plane of incidence $\psi_i = \pi/2$, which is always true for $\beta_i = 0$, and

[1] Inhomogeneous wave in an absorbing medium is a wave whose complex wave vector has non- collinear real and imaginary components.

we can use the conventional complex Snell-Descartes laws to determine parameters of transmitted wave:

$$\mathrm{s\ i}\,\hat{\theta}_r = \mathrm{s\ i}\,\hat{\theta}_i \tag{105}$$

$$\hat{n}_2 \sin\hat{\theta}_t = \hat{n}_1 \sin\hat{\theta}_i \tag{106}$$

where $\hat{\theta} = \theta - i\ ,\beta\theta$ is the angle of incidence; and indexes i, r, t mean incident, reflected and transmitted wave, respectively. The parameter ψ_t saves its value $\pi/2$.

The parameters θ_t, β_t and ψ_t determine unambiguously the complex wave vector for transmitted wave $\hat{\boldsymbol{k}}_t$. Using this vector, the reflection coefficients can be determined as [73]:

$$\hat{r}_s = \frac{\hat{k}_i^z - \hat{k}_t^z}{\hat{k}_i^{z*} + \hat{k}_t^z} \quad \text{for s-wave} \tag{107}$$

$$\hat{r}_p = \frac{\hat{k}_i^*\left(\hat{k}_t^2\hat{k}_i^z - \hat{k}_i^2\hat{k}_t^z\right)}{\hat{k}_i\left(\hat{k}_t^2\hat{k}_i^{z*} + \left(\hat{k}_i^*\right)^2\hat{k}_t^z\right)} \quad \text{for p-wave} \tag{108}$$

And the intensity reflection coefficient for unpolarized light is:

$$R_c = \frac{|\hat{r}_s|^2}{2} + \frac{\left|\hat{r}_p\right|^2}{2} \tag{109}$$

We have established the expressions for reflection coefficients from the boundary between two absorbing media for plane homogeneous wave. These expressions are used to find reflection coefficients for coherent light in section 2.4.2 and to calculate the reflection coefficient for diffuse light in the next section.

2.5.2 Diffuse light

The reflection coefficient for the diffuse light can be introduced in terms of fluxes as:

$$R_d = F_r/F_i \tag{110}$$

where F_i is an incident flux and F_r is a reflected flux from some surface.

For radiation field with azimuthal symmetry (see (87)), the reflection coefficient (110) can be expressed as:

$$R_d = \frac{2\pi\int_0^{\pi/2} R(\vartheta)I(\vartheta)\,\mathrm{c\ co}\vartheta\,\mathrm{s\ i}\vartheta\ d\ \cdot}{2\pi\int_0^{\pi/2} I(\vartheta)\,\mathrm{c\ co}\vartheta\,\mathrm{s\ i}\vartheta\ d\ \cdot} \tag{111}$$

which simplifies to $R_d = 2\int_0^{\pi/2} R(\vartheta)\cos\vartheta\sin\vartheta d\vartheta$ in the case of isotropic diffuse light [74].

For the case of absorbing media, this integral is computed numerically with $R(\vartheta)$ calculated by (109). It is supposed that incident light consists of only homogeneous waves propagating at different angles with respect to the interface.

In the case of transparent media, this coefficient R_d was obtained analytically in [75–77]:

$$R_d = \frac{1}{2} + \frac{(n-1)(3n+1)}{6(n+1)^2} + \frac{n^2\left(n^2-1\right)^2}{(n^2+1)^3}\ln\left|\frac{n-1}{n+1}\right| - \frac{2n^3\left(n^2+2n-1\right)}{(n^2+1)(n^4-1)} + \\ + \frac{8n^4\left(n^4+1\right)}{(n^2+1)(n^4-1)^2}\ln|n| \tag{112}$$

It produces the same results as similar expressions (but derived differently) from [78]. And also it satisfies the condition $R_d + T_d = 1$ for T_d from [79].

2.6 Applicability of the model

The following assumptions are supposed in the model:

- The laser beam axis is perpendicular to the surface.
- The wave is plane, monochromatic and unpolarized.
- The propagation of light is one-dimensional. The model does not take into account the widening of radiation field due to scattering. Thus, it is valid when transversal size of laser beam is much greater than the thickness d of the layer.
- The boundaries are smooth. The reflection coefficient for collimated light is determined according to the generalized Fresnel formula. The reflection coefficient for diffuse light is determined as the average over all angles of incidence.
- The substrate is homogeneous. There is no back-flux from the substrate into the layer.

The real laser beams are neither monochromatic, nor plane. The laser beam will be quasi-monochromatic within the frames of the model if the following condition is met [80], [81]:

$$N\Delta s \ll \frac{\lambda^2}{\Delta\lambda} \quad \text{where } N = \frac{\pi\sqrt[4]{R_{c1}^- R_{c2}^+}\exp(-\alpha_i)}{1-\sqrt{R_{c1}^- R_{c2}^+}\exp(-2\alpha_i)} \tag{113}$$

For a laser with the wavelength $\lambda = 1.064$ μm and a layer of 10 μm thickness with refractive index $n = 2.5$ ($R = 0.18$) and absorption coefficient $\alpha = 0.1$, the laser spectral width should be $\Delta\lambda \ll 4.5$ nm.

The laser beam will be quasiplane in the scope of the model if it produces less than one interference fringe upon the reflection from the layer [80].

$$\vartheta_1 < \sqrt{\frac{n_1 \lambda}{d}} \tag{114}$$

For example, for the laser beam (wavelength $\lambda = 1.064$ μm) falling on the layer of thickness $d = 10$ μm with refractive index $n = 2.5$, the model is applicable if the laser beam angle is less than $\vartheta_{laser} < 3.0°$.

2.7 Conclusions

- Theoretical model for determination of damage threshold of a pure metal substrate was developed and applied. For the model to calculate the damage threshold fluence for metals, it was supposed that damage occurs at the fluence when the maximal temperature due to laser heating reaches the melting point.
- The calculations have demonstrated that multi-pulse heat accumulation was not significant and could be neglected.
- In contrast, the effect of reflectivity change as a function of surface temperature was significant during laser-substrate interaction.
- To determine multiple-pulse damage threshold, the phenomenological theory explained by plastic deformations accumulation was applied.
- Using the model, damage thresholds for stainless steel, molybdenum, and tungsten were calculated.
- New model of laser wave propagation in a scattering layer on the metal surface was developed.
- The in-depth distributions of total flux $F_t(z)$ and the dependences of total reflection coefficient on the layer thickness $R_t(d)$ were calculated for different values of scattering coefficient.
- The model is validated by the comparison with two models developed earlier.

The next step of improvement of the model is to take into account the roughness of the surfaces as it was done in [82].

Chapter 3. Description of experimental equipment

Contents

This chapter describes the experimental equipment and methodology applied in this study. The laser ablation set-up for laser cleaning and the temperature measurement set-up are presented. The instruments for surface characterization and reflection coefficient measurements are also introduced. The data treatment methods for damage thresholds and laser heating temperature measurements are specified.

3.1 Laser ablation and heating

Two laser set-ups are used in our study: DetriLaser system for the laser ablation and a temperature measurement set-up for laser heating studies.

The DetriLaser (Figure 22) system comprises a pulsed ytterbium fiber laser (IPG YLP-1/120/20), a x-y galvanic scanner (SCANLAB SCANcube 10) and a focusing lens (Linos F-Theta Ronar, λ = 1064 nm, f = 420 mm). The aspirated air is filtered by PUREX LASEREX 400iPVC vacuum pump. The sample is mounted on a micro-control assembly (with the positioning precision of ± 5 μm) with a double-faced adhesive tape. The assembly can be precisely moved in the direction of the laser beam propagation to change the sample position with respect to the waist position.

Table 3: Specifications of the DetriLaser set-up.

Wavelength	1.06 μm
Average laser power	2 – 20 W
Pulse repetition rate	20 kHz
Pulse energy	from 0.1 mJ up to 1 mJ
Pulse duration	120 ns (full width at half maximum)
Beam quality factor	M^2 = 1.5
Laser beam radius in the waist position	53 μm at the 1/*e* intensity
Laser fluence in the waist position	1 – 10.5 J/cm^2
Scanning speed	Up to 9000 mm/s
Maximum scan field	290×290 mm^2

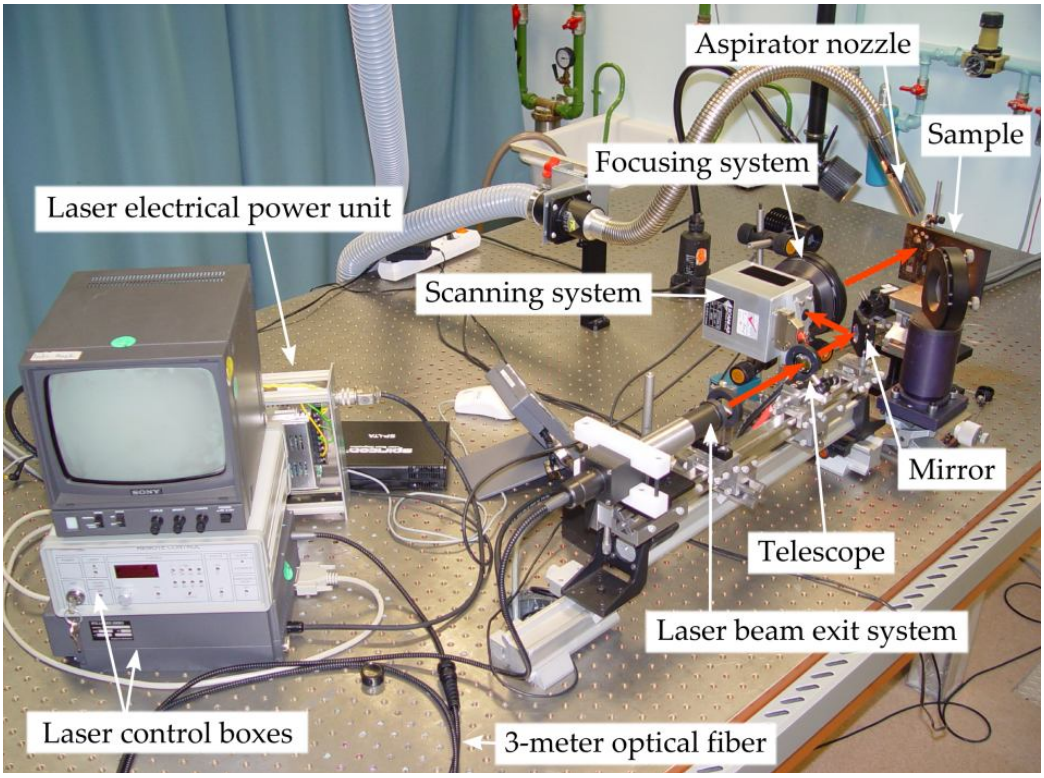

Figure 22: Photo of DetriLaser set-up.

For nanosecond laser ablation, a fluence deposited on the surface is one of the main parameters, which determines the amount of removed material and the physical mechanisms involved in this ablation. For the Gaussian laser beam, the fluence is not constant over the beam profile, but corresponds to the intensity distribution. The maximal fluence at the centre of a beam equals to

, where E is the pulse energy and a is a laser beam radius at $1/e$ intensity. Further in this work, this maximal fluence is referred to as a "pulse fluence".

Waist position. At the fixed laser pulse energy, the fluence depends on the laser beam radius, and, hence, on the sample position with respect to the waist position. To find the exact waist position of the laser beam, the test sample is treated with a maximal laser power of 18.6 W, but at different positions along the laser beam axis Z. Then, the spots formed as a result of substrate melting/ablation are analysed with an optical microscope (see Figure 23). At the position near the beam waist, the beam in narrow and the fluence is high. In this case, the extruded ridges around the irradiation spot are well observable (Figure 23). As we move away from the beam waist position in any direction, the laser beam widens and the pulse fluence decreases. At some distance, ridges are not formed anymore (Figure 23). These positions are situated at equal distances from the waist in the opposite directions. Hence, the waist position can be found as the center between two positions where

ridges disappear. For the measurement, presented on Figure 23, the waist is at $Z = 18.5$ mm.

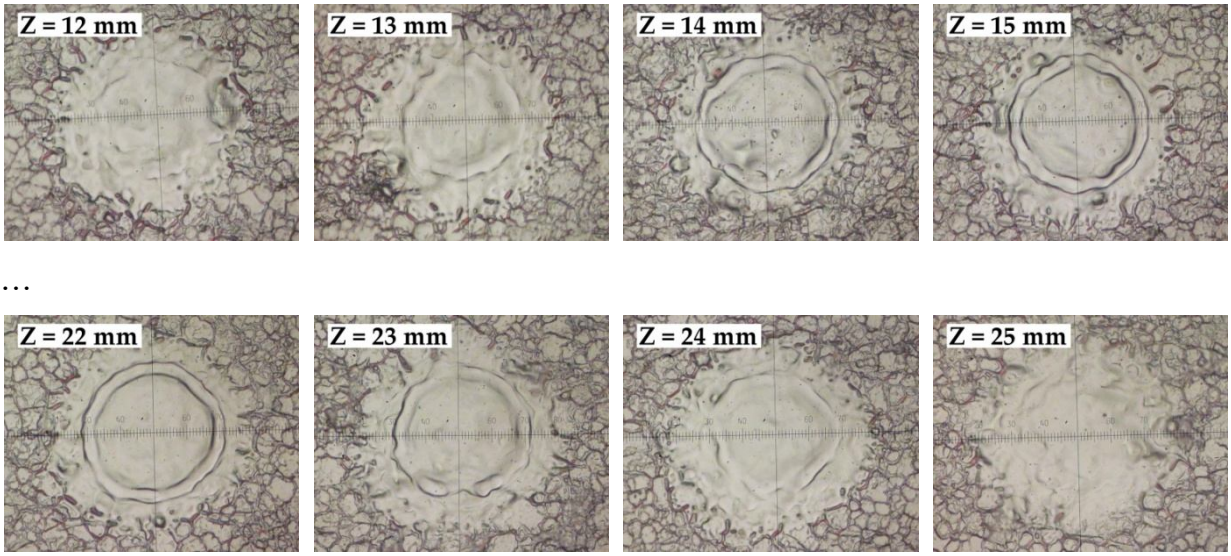

Figure 23: Photos of craters formed at different positions along the laser beam axis. *Z* indicates the different positions of the sample along the beam axis.

To find the exact beam radius, the laser beam profile is measured with the camera CCD Pulnix TM-6AS and the SPIRICON acquisition system for different mean laser powers. The laser beam is attenuated by a reflecting mirror to avoid camera damage. For each measured profile, it is fitted to the Gaussian profile and the beam radius is determined. To obtain the average beam radius, we calculated laser fluence as a function of the laser power and fitted this dependence with a linear function (see Figure 24). We obtained the average laser beam $a = 53.6 \pm 1.8$ μm.

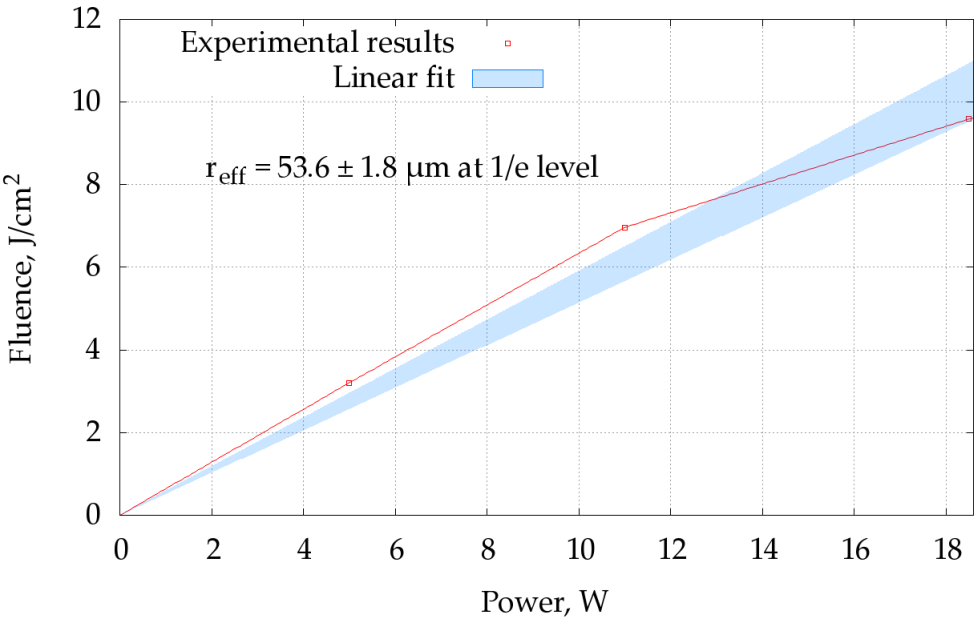

Figure 24: Dependence of the laser fluence in the focal plane on the mean laser power for DeltriLaser set-up. Blue zone indicates the best linear fit to the experimental results. Beam radius corresponding to this fit is indicated as $r_{e\ f\cdot f}$

The photo of the temperature measurement set-up is shown on Figure 25. The main features are the following:

- The sample is mounted on the holder with embedded electric heater to allow sample preheating up to 700 K.
- For laser heating, an ytterbium fiber laser IPG YLR-100 is used. The laser can work in CW (continuous wave) or pulsed modes with the peak power of 100 W and the maximal average power of 50 W and with adjustable pulse durations from 1 ms up to CW mode. In the case of the pulsed mode, the laser pulses are shaped by a pulse generator (Schlumberger 4433). The laser power is verified before any measurement by a calorimeter (Scientech 380101). The specification gives the output laser beam diameter as 5.0 ± 0.1 mm at $1/e^2$ intensity level.
- For temperature measurements, a pyrometer (Kleiber KGA 740-LO) is used. Its sensitivity curve is shown on Figure 26. The pyrometer response time is 6 μs (t_{95}). To eliminate the influence of the reflected laser radiation on the detector, an optical filter is used. Its spectral transmittance is shown on Figure 27.
- A fast photodiode (EG&G FND-100) with rise time of less than 1 ns into 50 ohms is used to control laser pulses shape and duration.

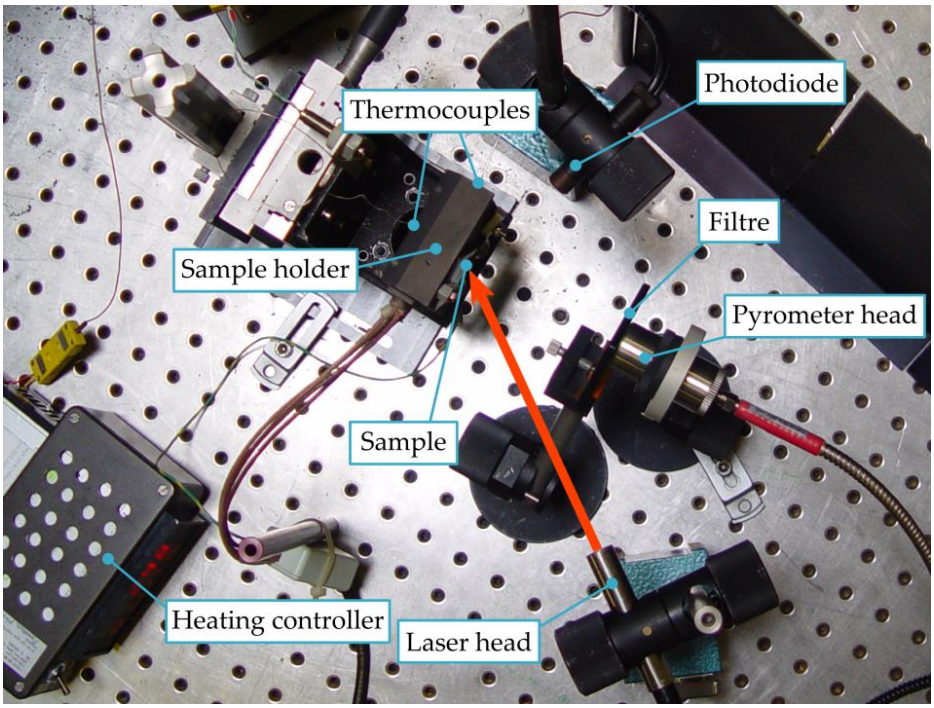

Figure 25: Photo of the temperature measurement set-up.

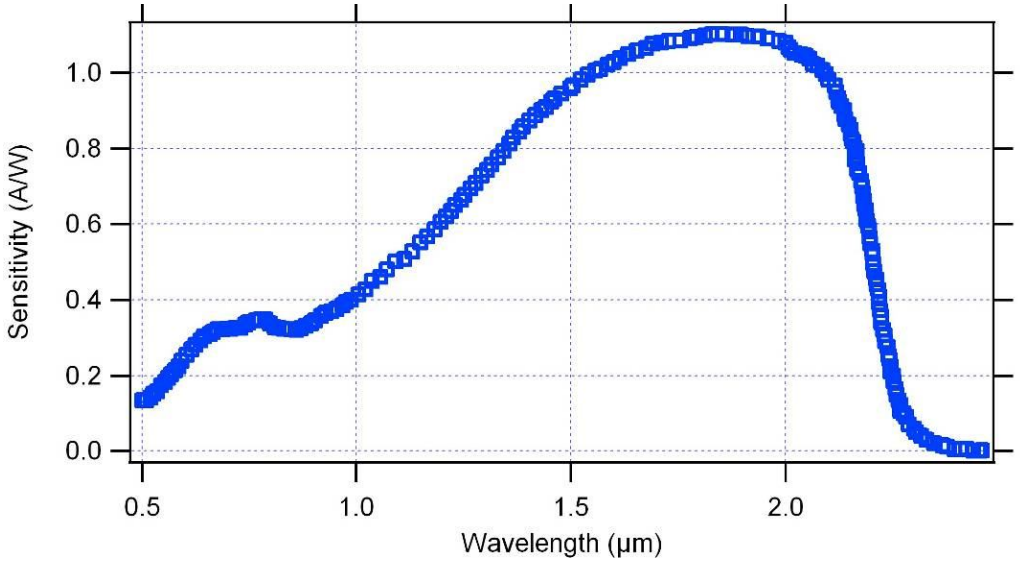

Figure 26: Kleiber KGA 740-LO pyrometer spectral sensitivity

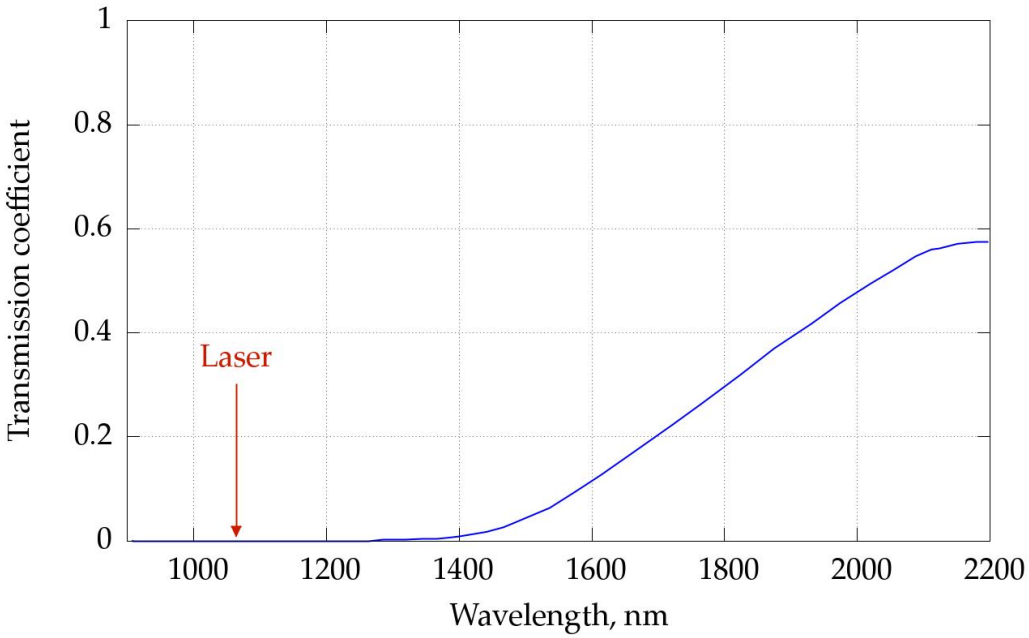

Figure 27: Transmission curve of the optical filter placed in front of the pyrometer

The pyrometer was calibrated with a black-body source. Figure 28 shows the obtained calibration curve.

The expression to convert pyrometer signal to the black body temperature is:

(115)

where U is the pyrometer signal in mV (R = 50 ohms), $a = 5.3 \cdot 10^{-14}$ and $b = 5.56$.

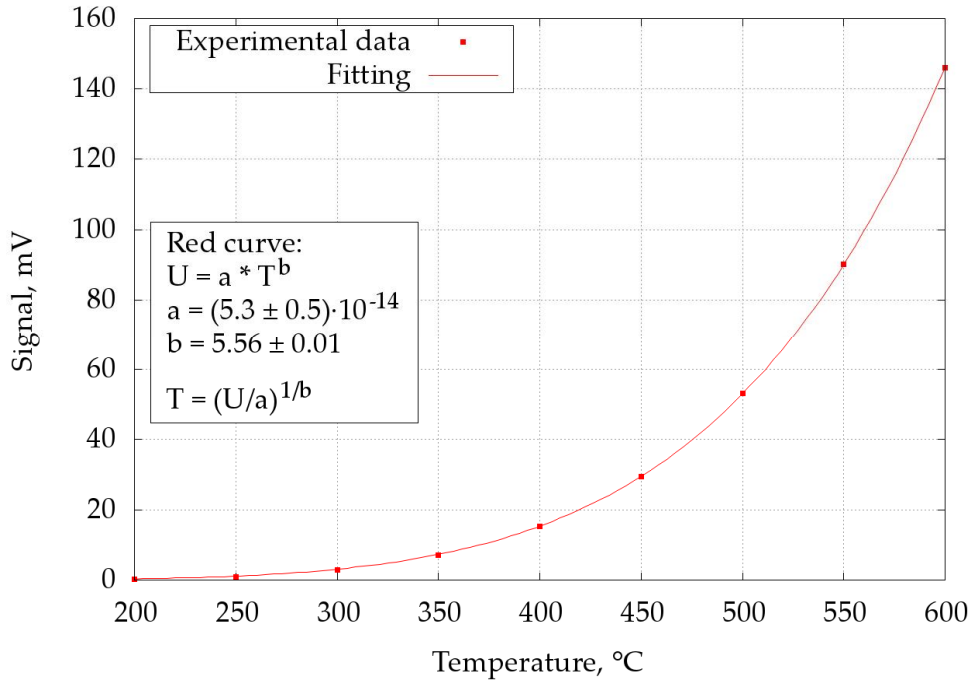

Figure 28: Calibration curve of the pyrometer Kleiber KGA 740-LO

3.2 Analysis of a sample surface

The analysis of a sample surface is performed with an optical microscope (Olympus polarising microscope, Carl Zeiss Axioscope 50) and a scanning electron microscope (JEOL JSM-7000F).

The surface height profiles are measured with an optical profilometer (Phase Shift Technology MicroXAM 100) and mechanical profilometer Mahr.

The optical profilometer MicroXAM 100 is based on the Mirau interferometer [83]. Figure 29 presents the scheme of the optical profilometer. The light from the source goes to the microscope objective where it is split into two identical beams. The first reference beam is reflected from the reference surface inside the objective, while the second one — from the test surface. Due to test surface roughness, parts of the beam reflected from different points are of different phase lag with respect to the reference beam. Then, these two beams combine, thus forming an interference pattern that is imaged on the CCD sensor. This interference pattern forms only when the surface is near the focal position of objective and is completely defined by the surface profile.

To form the height map of the test surface, the objective scans over a distance in a vertical direction. During the scan, the interference pattern changes and is analysed by a computer. These data are then interpreted to provide height information on a pixel basis, for a highly resolved 3D representation of the surface.

Table 4: Specifications of MicroXAM 100 profilometer

Objectives	5x (f/# = 0.13), 20x (f/# = 0.40)
Camera resolution	376 × 240 px
Measuring areas	827 × 626 μm (5x), 206 × 156 μm (20x)
Spatial sampling	2.2 × 2.6 μm (5x), 0.55 × 0.65 μm (20x)
Optical resolution	2.12 μm (5x), 0.69 μm (20x)
Vertical scan range	Up to 10 mm
Depth of focus @550 nm	20.72 μm (5x), 2.19 μm (20x)
RMS repeatability	1 nm
In-depth resolution	4 nm

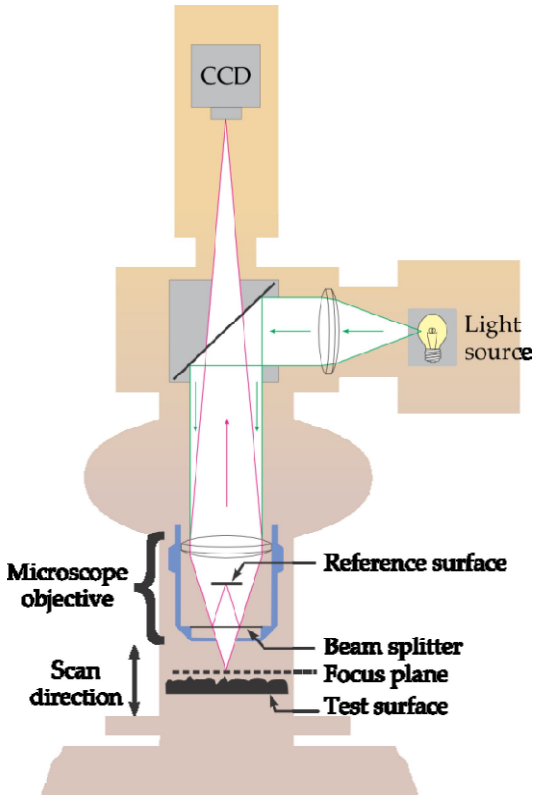

Figure 29: The principal scheme of MicroXAM 100 optical profilometer

In the mechanical profilometer, a diamond stylus is moved vertically in contact with a sample and then moved laterally across the sample for a specified distance. The profilometer can measure small surface variations in vertical stylus displacement as a function of the position. On Figure 30, the principal scheme of the mechanical profilometer is presented. The profilometer is intended primarily for the line profiles measurements, but it can be used to measure several equidistant line profiles, thus, forming surface profile. The profilometer Mahr is equipped with:

- a measurement unit PAV-CV, which controls movements of a pick-up and a table and transfers the measurement data to a computer;
- a drive unit PGK-20;
- a pick-up MFW-250;
- X/Y-table PKT and motorized position controller VSE-PKT.

The profilometer specifications are presented in Table 5.

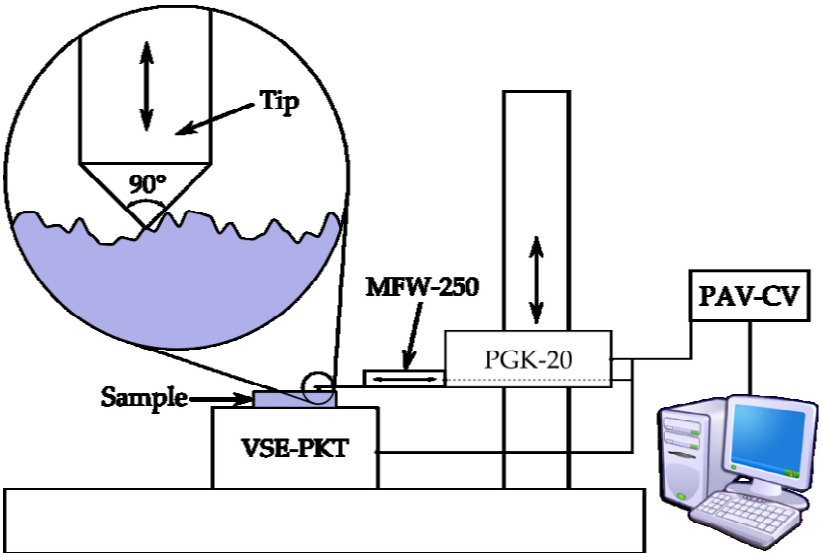

Figure 30: The principal scheme of mechanical profilometer Mahr.

Table 5: Profilometer Mahr specifications

Maximal profile length	20 mm
Maximal/minimal stylus height	± 250 μm
Scanning speed	0.1 or 0.5 mm/s
Sampling	Up to 16000 points/profile
Lateral resolution	0.1 μm
In-depth resolution	10 nm
Tip radius	2 μm
Tip angle	90°
Flatness	< 0.2 μm/20 mm
Residual roughness R_z	< 30 nm

The analysis of all 2D profiles measured with these instruments was performed with the Gwyddion software [84].

3.3 Reflection coefficient measurements

To measure the reflection coefficients of samples, a spectrometer (PerkinElmer Lambda 19) and a set-up based on an integrating sphere were used.

Figure 31: Photo of PerkinElmer Lambda 19 spectrometer

The spectrometer is capable to measure spectral reflection coefficient from 200 nm to 2600 nm wavelength. To perform reflection coefficient measurements, a special reflectance accessory was installed into the sample chamber. The photo of the accessory and the scheme of measurement are shown on Figure 32. The angle of measurements is fixed at 10°. The reflection measurements were carried out under normal atmospheric conditions.

Before measurements, the calibration of the instrument is necessary. For calibration, the sample is removed and the auxiliary mirror is in the bottom position (see Figure 32, left). In this case, the sample beam makes three reflections: 2 from the prismatic mirror and 1 from the auxiliary one. The spectrum measured in this configuration is saved as the reference.

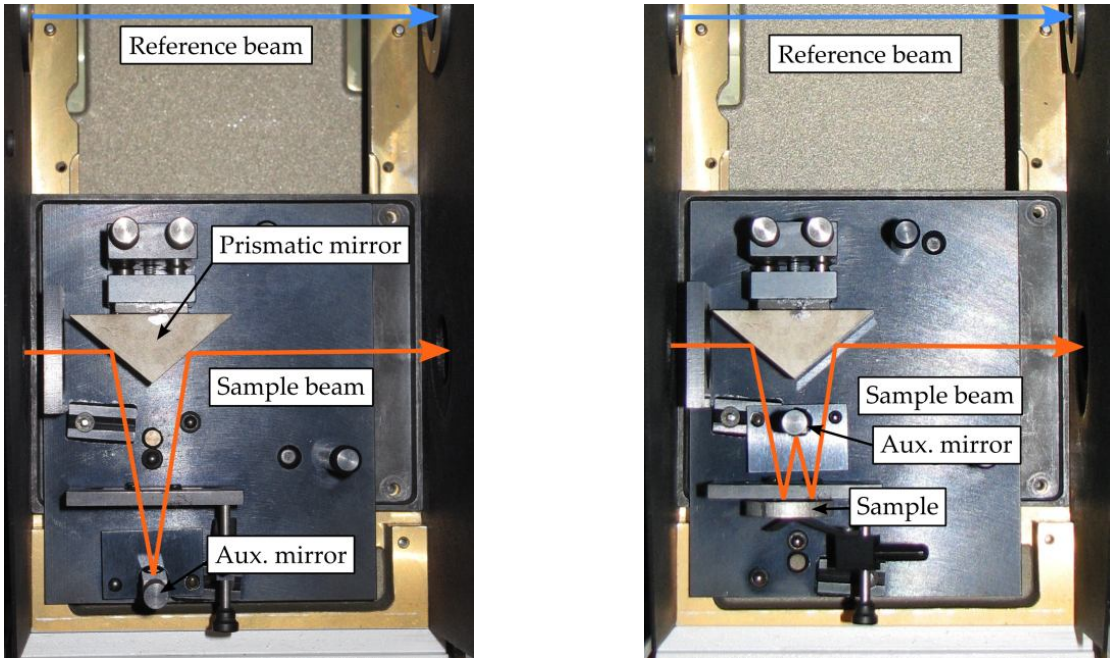

Figure 32: Scheme of the reflection coefficient measurement accessory

To perform sample reflectivity measurements, the auxiliary mirror is placed in the top position and the sample is placed to the holder (see Figure 32, right). The sample beam makes 5 reflections in this case: 2 from prismatic mirror, 1 from auxiliary surface and 2 from the sample. Hence, by dividing the spectrum measured with sample by the reference spectrum, the spectral dependence of is obtained. Three separate measurements are performed with a sample to verify correct sample placing to the holder.

3.3.1 Integrating sphere

The spectrometer is able to measure only specular reflection coefficient. To measure diffuse and total reflection coefficients, the integrating sphere LabSphere is used.

The integrating sphere has three identical ports of 6.4 mm, two of which are on the diametrally opposite sides. The fast photodiode FND-100 (rise time is less than 1 ns at 50 ohm) is installed in an upper port. Two available diametrally opposite ports are used to insert the laser beam and to place the sample for measurements.

Measurements are performed as follows: at first, we place the sphere so that the axis of the sphere passing through centers of these apertures makes an angle with the optical axis of laser system to provide laser beam pass through it (Figure 33, a). When the exit of the sphere is open, we receive a zero signal on the detector. If we set the back plug, the light reflects in all directions (Figure 33, b). As the surface of the

sphere and the plug reflects almost 100% of light, the signal in this case was taken as the reference. Then, we bring our sample to the exit of sphere (Figure 33, c). In this case, the sample secularly reflects a certain part of the light, and then this part falls onto the surface of the sphere, which reflects it in all directions. The ratio of the detector signal obtained with the sample to the reference signal was taken as a total reflection coefficient of the sample.

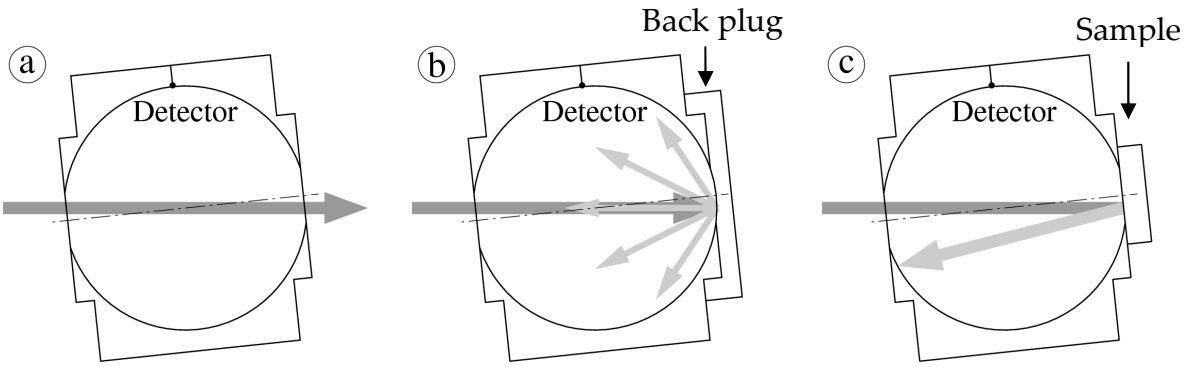

Figure 33: Scheme of the reflection coefficient measuring using an integration sphere

Therefore, we apply the spectrometer to measure specular reflection coefficient and the integrating sphere to measure total reflection coefficient. Diffuse reflection coefficient is determined as a difference between total and specular ones.

3.4 Methodology

3.4.1 Damage threshold measurements

The calculation of the thresholds fluences is based on the analysis of the craters diameters formed under laser pulses of different energy with the Gaussian spatial profile. This is a so-called "burning paper" technique [85].

The distribution of intensity in the plane perpendicular to the direction of propagation of the Gaussian beam is:

$$I(r) = I_0 \, \mathrm{e}^{\,\mathrm{x}\left(-\frac{r^2}{a^2}\right)} \tag{116}$$

We can relate the fluence with the intensity as $F = I\tau$, where τ is the pulse duration, hence, the fluence F has the same spatial distribution as the intensity. The fluence is calculated as $F_{e\ x\ \overline{p}} E/\pi a^2$, where a is the laser beam radius at $1/e$ intensity. We can calculate the total deposited energy as:

$$E = \int_0^{\infty} 2\pi\, r\,(r)d \;\; = \pi a^2 F_0 \tag{117}$$

Consequently, the experimental fluence equals to the maximal fluence in the centre of the Gaussian beam $F_{e\ x\ \overline{p}} F_0$.

We suppose that the damage occurs at the points where the fluence is higher than some threshold fluence F_{th}. Then, the spot diameter r_s can be found by solving the equation:

$$F_{th} = F(r_s) = F_0\, \mathrm{e}\ \mathrm{x}\left(-\frac{r_s^2}{a^2}\right) \tag{118}$$

which can be expressed as:

$$r_s^2 = a^2 1\ \ \frac{F_0}{F_{th}} \tag{119}$$

This means that the dependence of r_s^2 on $1\ \ F_0$ is linear, and coefficient of this dependence can be used to find a and F_{th}.

If we fit out experimental results by the linear function $y = \alpha x + \beta$, where $y = r_s^2$ and $x = 1\ \ F_0$, then, we can express a and F_{th} as:

$$a = \sqrt{\alpha} \quad F_{th} = \mathrm{e}\ \ \mathrm{x}(-\beta/\alpha) \tag{120}$$

The uncertainties of laser beam radius and damage threshold can be found with the expressions

$$\Delta a = \frac{\Delta\alpha}{2\sqrt{\alpha}} \quad \Delta F_{th} = \frac{\mathrm{e}\ \ \mathrm{x}(-\beta/\alpha)}{\alpha}\sqrt{\frac{\beta^2}{\alpha^2}\Delta\alpha^2 + \Delta\beta^2} \tag{121}$$

where uncertainties of coefficients $\Delta\alpha$ and $\Delta\beta$ are determined by fitting routine.

3.4.2 Temperature measurements

The procedure of temperature measurement consists of the following steps:

1. measurement of the pyrometer signal U_0, when the sample temperature equals to the room temperature T_r = 293 K (Figure 34**a**);
2. measurement of the pyrometer signal U_h, when the sample is heated and its temperature equals to T_h = 500–600 K (Figure 34**b**);
3. calculation of sample surface emissivity using these two measurements and the detector calibration curve;
4. measurement of the pyrometer signal due to the periodic laser pulsed heating; the signal is averaged over 50 pulses (Figure 34**c**);
5. calculation of the heating temperature from the signal using sample surface emissivity and reference level (Figure 34**d**).

We will omit the detailed description of the first four steps for further measurements and present only the resulting heating temperatures.

The emissivity of the material is the "multiplicative factor … which rates the radiated power to that of a blackbody for which $\varepsilon = 1$, at the same temperature" [86]. The emissivity can be calculated as the ratio of the difference between pyrometer signals from the sample at two different temperatures T_1 and T_2 to the difference between pyrometer signals from the black body at the same temperatures:

$$\varepsilon = \frac{\Delta U}{\Delta U_b} = \frac{U(T_1) - U(T_2)}{U_b(T_1) - U_b(T_2)} \tag{122}$$

We have used room temperature T_r as T_1 and the temperature T_h as T_2.

After determination of emissivity, the recalculation of the pyrometer signal to the surface temperature is straightforward and can be done using the expression (see black body calibration curve in section 3.1):

$$T = \left(\frac{U - U_0}{a}\right)^{\frac{1}{b}} + T_r \tag{123}$$

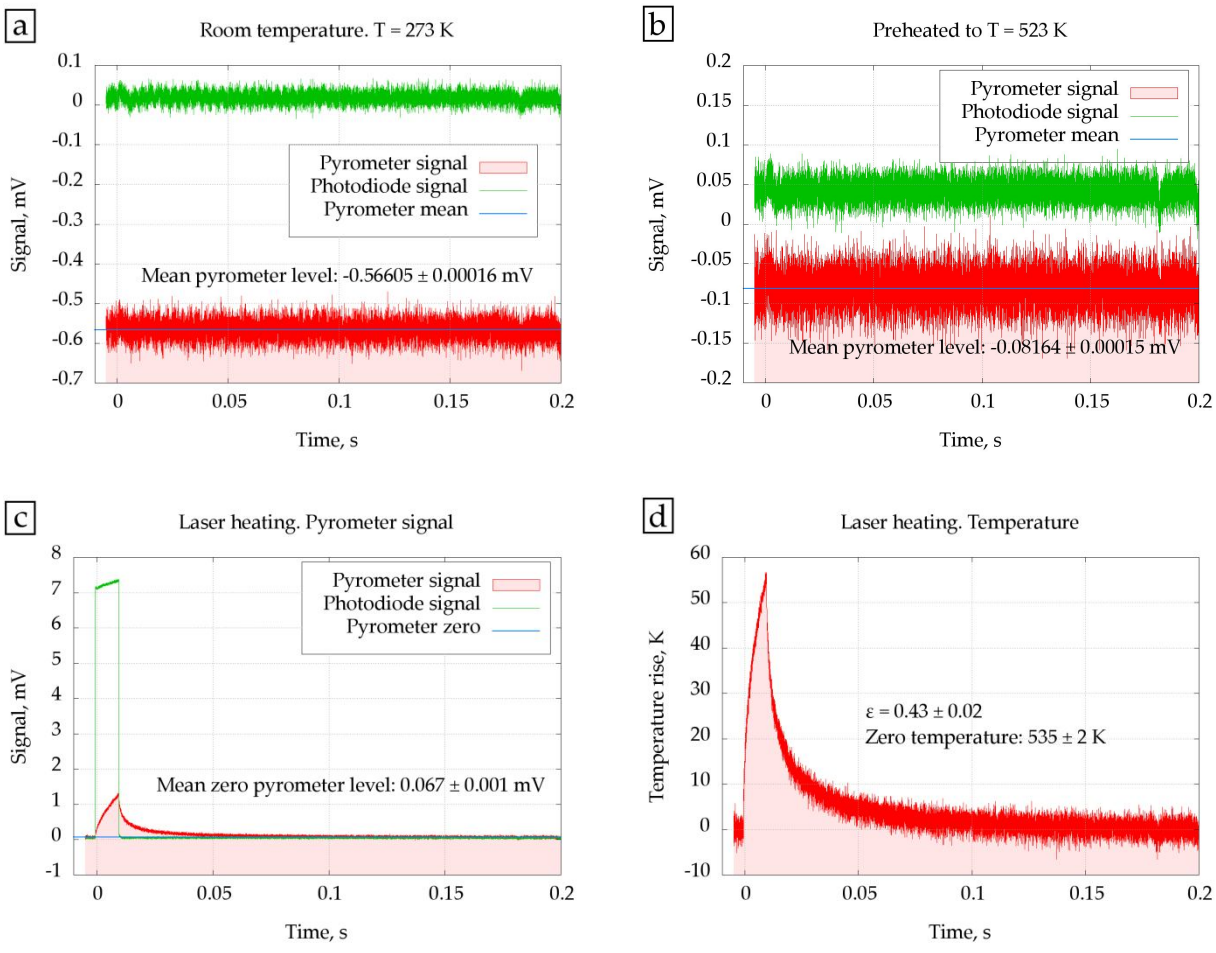

Figure 34: The procedure of laser heating temperatures measurements

3.5 Conclusions

Laser ablation and laser cleaning tests are performed with a pulsed ytterbium fiber laser (IPG YLP-1/120/20) with 120-ns laser pulse at 1.064 μm. According to the previous studies presented in 0, this wavelength is the most efficient for laser decontamination. The set-up is properly adjusted, and a focal plane of laser is found. The laser system supplies the fluence up to 10.5 J/cm^2 in the focal plane. This is more than enough to ablate the most types of deposited layers from metal substrates.

The efficiency and features of laser ablation and cleaning are analysed by measuring surface profiles before and after laser treatment. Two profilometers, an optical (Phase Shift Technology MicroXAM 100) and a mechanical (Mahr), were applied. For laser cleaning, the ablated depth is determined as a difference in surface height of the treated area and the untreated one.

The reflectivity of metal mirrors subjected to laser cleaning is controlled by a spectrometer. A special accessory is used to allow measurements of reflection coefficient at 10° incident angle. Spectra obtained with the spectrometer provide information on the reflection coefficient restoration in the wavelength range from 250 to 2500 μm. Along with the spectrometer, which measures only specular reflection coefficient, a set-up based on integrating sphere is applied to measure total reflection coefficient of a surface under interest at 543.5 and 1064 nm wavelengths.

The pyrometer for laser heating temperature measurements is calibrated with a black body radiation source. The appropriate data treatment method, which is able to determine the unknown emissivity of a sample, is chosen.

Chapter 4. Experimental results

Contents

4.1 Laser cleaning of contaminated oxidized metal surface

As it was described in Chapter 1, one of the applications of laser ablation is laser decontamination of metal components from nuclear power plants.

The following experiments are aimed to investigate laser cleaning performances of oxidized stainless steel surface. Among different types of steel, an AISI 304L steel is chosen, because it is often used in modern nuclear power plants. The provider gives the following composition of the heat (in weight percent): 18.231% Cr, 8.073% Ni, 1.88% Mn, 0.305% Si, 0.071% N, 0.03% P, 0.018% C, 0.003% S.

Experiments with radioactive sample require special regulations and safety. Besides, it is not possible to measure ablation depth or perform GDS measurements without special equipment adapted for radioactive experiments. Our experiments are carried out with non-radioactive samples simulating the real oxidized surface. This allows us to perform all necessary work on the conventional equipment.

4.1.1 Oxidation by laser

Several tests were performed to investigate the possibility to form the oxide layer on the surface of samples by laser. Different treatment regimes were investigated: the single-pulse fluence varies in the range of $F = 0.57 – 3$ J/cm² and the effective number of pulses in one place $(N_{e\ f})_f$ ranges from 5000 to 40000. The treatment was performed in air at atmospheric pressure.

To speed up the treatment in all cases, the maximal laser power was used and the sample was displaced from focal position at the distance Δz to reduce single-pulse fluence. The photos of treated zones are presented on Figure 35 and the details of treatment are presented in Table 6.

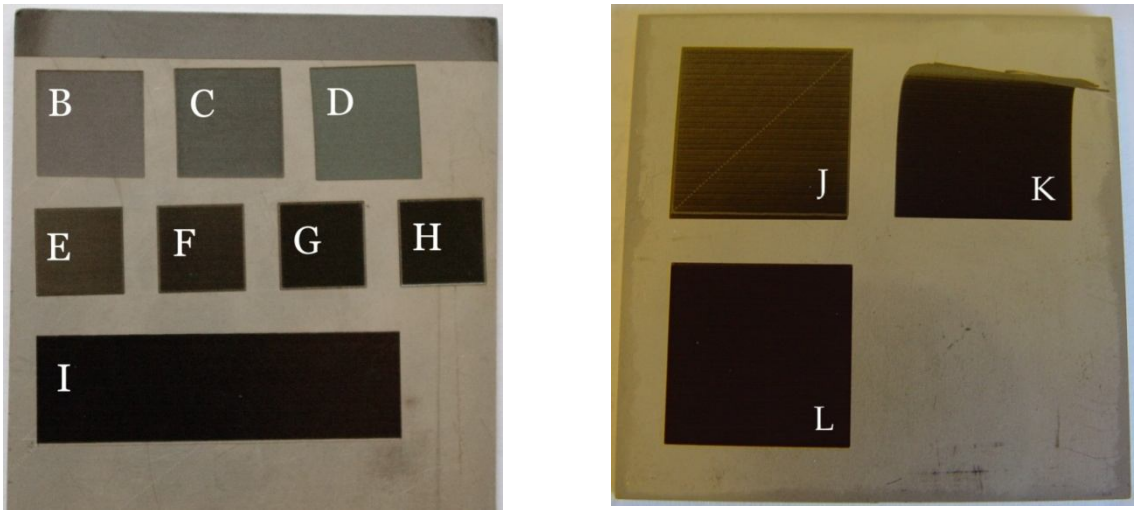

Figure 35: Overview of laser treated zones

Table 6: Detailed information about oxidation regimes

Sample/Zone	Zone size, mm²	Fluence F Displacement Δz Beam radius r	Scanning regime
A	50x50	F = 0.57 J/cm² Δz = 23.4 mm r = 228 µm	$\Delta x = \Delta y$ = 4.27 µm v_x = 85 mm/s N_{eff} = 5000
B	15x15	--	$\Delta x = \Delta y$ = 4.27 µm v_x = 85 mm/s N_{eff} = 10000
C	15x15	--	$\Delta x = \Delta y$ = 3.022 µm v_x = 60 mm/s N_{eff} = 20000
D	15x15	--	$\Delta x = \Delta y$ = 2.14 µm v_x = 42.74 mm/s N_{eff} = 40000
E	12x12	F = 1 J/cm² Δz = 17.3 mm r = 172 µm	$\Delta x = \Delta y$ = 4.5 µm v_x = 90 mm/s N_{eff} = 5000
F	12x12	--	$\Delta x = \Delta y$ = 3.176 µm v_x = 63.5 mm/s N_{eff} = 10000
G	12x12	--	$\Delta x = \Delta y$ = 2.25 µm v_x = 45 mm/s N_{eff} = 20000
H	12x12	--	$\Delta x = \Delta y$ = 1.59 µm v_x = 31.76 mm/s N_{eff} = 40000
I	50x15	F = 3 J/cm² Δz = 9 mm r = 100 µm	$\Delta x = \Delta y$ = 15 µm v_x = 300 mm/s N_{eff} = 140
J & F	22x22	F = 1 J/cm² Δz = 17.3 mm r = 172 µm	$\Delta x = \Delta y$ = 3.176 µm v_x = 63.5 mm/s N_{eff} = 10000
K & H	22x22	--	$\Delta x = \Delta y$ = 1.59 µm v_x = 31.76 mm/s N_{eff} = 40000
L	22x22	F = 2 J/cm² Δz = 11.6 mm r = 122 µm	$\Delta x = \Delta y$ = 2.22 µm v_x = 44 mm/s N_{eff} = 10000

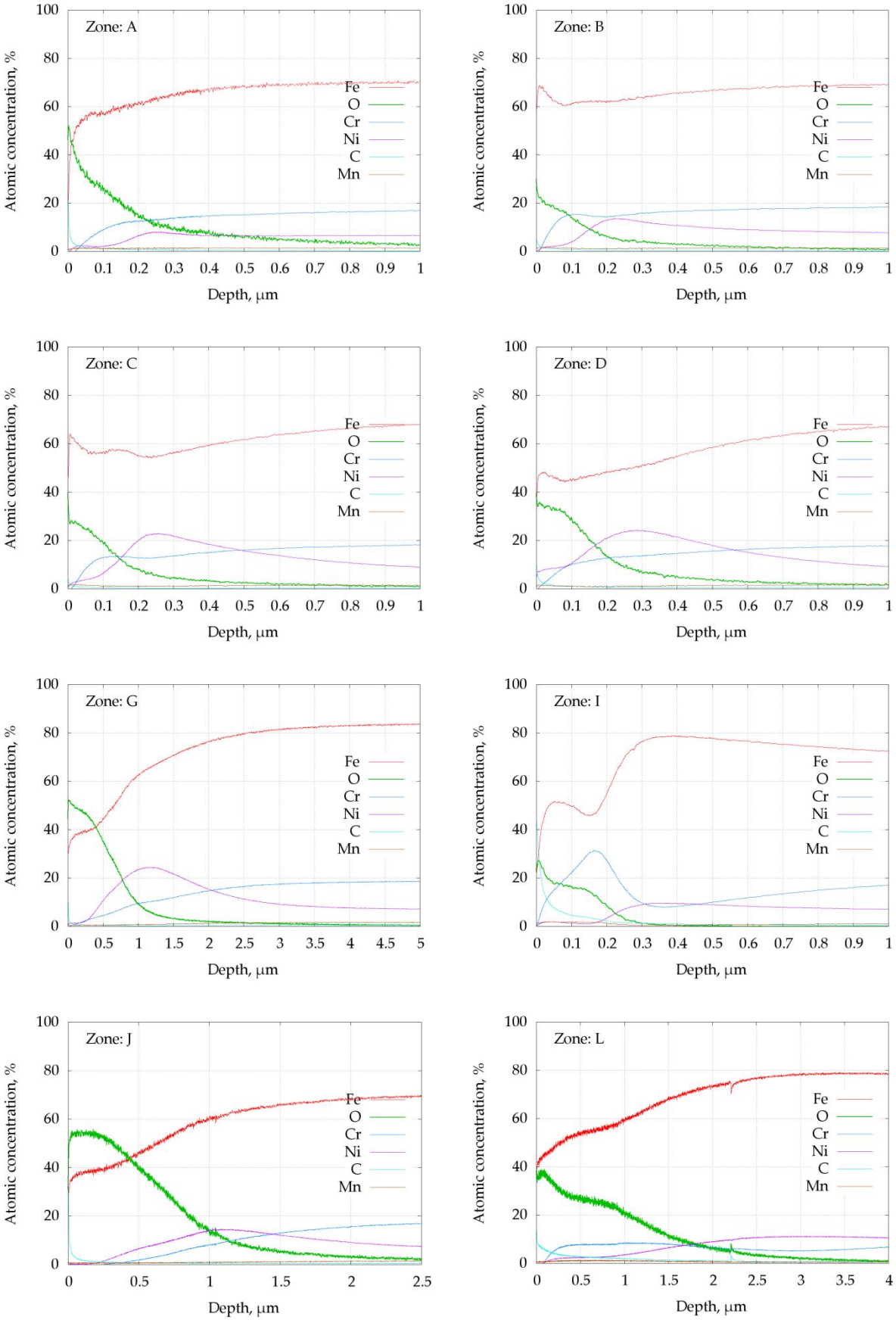

Figure 36: Results of GDS analysis of different zones oxidized by laser

The analysis of oxidized zones was performed with GDS. The results are shown on **Figure 36**. We define the thickness of an oxide layer as the depth where the concentration of oxygen drops to its half value at the surface.

From these experiments, we can conclude that oxide layer thickness does not increase strongly with effective number of pulses, but increases with single-pulse laser fluence. Indeed, for all zones A – D made with the fluence of 0.57 J/cm², the thickness is in the range of 0.1 – 0.2 μm. If we increase fluence to 2 J/cm², the thickness increases up to ~1 μm (zone L).

High fluences $F \geq 3$ J/cm² (zone I) are sufficient to ablate the oxide layer formed by laser heating, thus, its thickness drops again down to ~0.2 μm. However, only such regime shows formation of the second inner oxide sub-layer enriched with chromium.

4.1.2 Oxidation in furnace

A set of four identical samples made of AISI 304L stainless steel were treated in the furnace with 1273 K. The treatment consists of furnace heating up to working temperature (2 hours), holding for 20 hours at working temperature and cooling down during ~16 hours. The treatment was performed in air at atmospheric pressure.

The results of GDS measurements of the formed oxide layer are presented on Figure 37. For the furnace oxidized sample, the oxide has thickness of 1 – 2 μm. But unlike the laser formed oxide layers, oxygen penetrates up to 7 – 8 μm in depth.

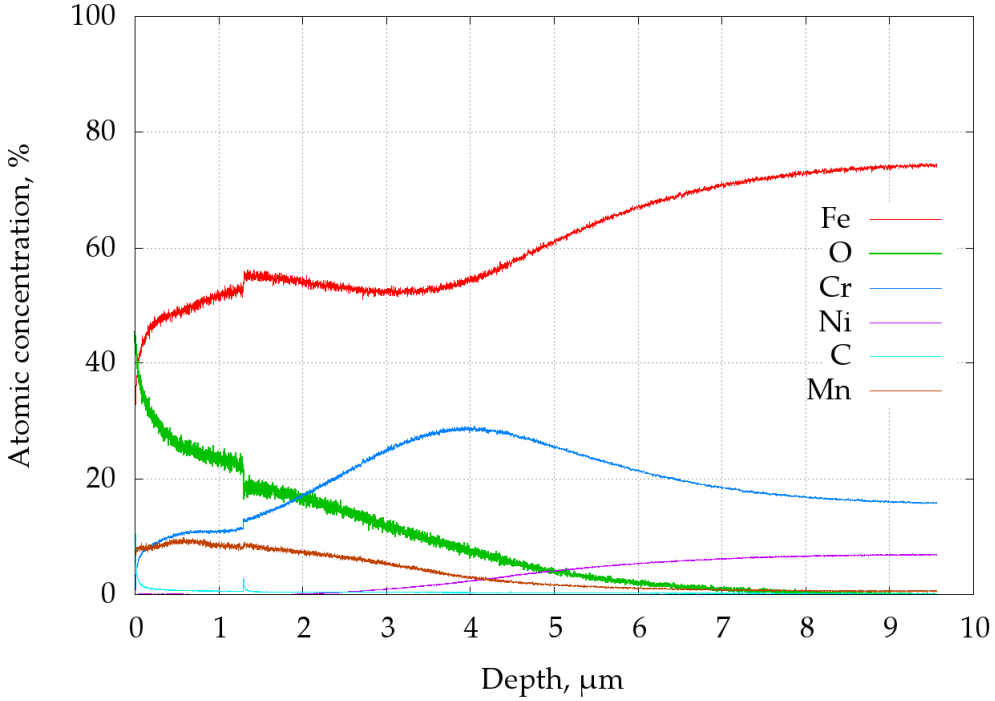

Figure 37: GDS of the sample oxidized in furnace

Thus, we have prepared a set of AISI 304L samples oxidized by laser and in furnace with different oxide layers.

4.1.3 Cleaning tests

Selection of the scanning regime was made before cleaning tests.

Laser beam scans the surface by zigzag. The horizontal scanning regime is characterized by the scanning speed v_x and horizontal scanning step Δx between two successive laser spots, which are related by $\Delta x = v_x/\nu$, where $\nu = 20000$ Hz is the laser repetition rate. The vertical scanning regime is characterized by the vertical step Δy between two successive lines. The tested scanning regimes are presented graphically on Figure 38 and their parameters are given in Table 7.

Table 7: Scanning regimes

Regime 1	$\Delta x = \Delta y = 50$ μm $v_x = 1000$ mm/s	**Regime 2**	$\Delta x = \Delta y = 100$ μm $v_x = 2000$ mm/s
Regime 3	$\Delta x = 100$ μm $\Delta y = 50$ μm $v_x = 2000$ mm/s	**Regime 4**	$\Delta x = 100$ μm $\Delta y = 25$ μm $v_x = 2000$ mm/s

The spots are not synchronized between two lines, i.e. the spots of the second line are not situated just under the spots of the first line. Rather, they can be shifted

(one against another) by a random distance. But for large enough number of passes, all laser impacts are uniformly distributed over the lines.

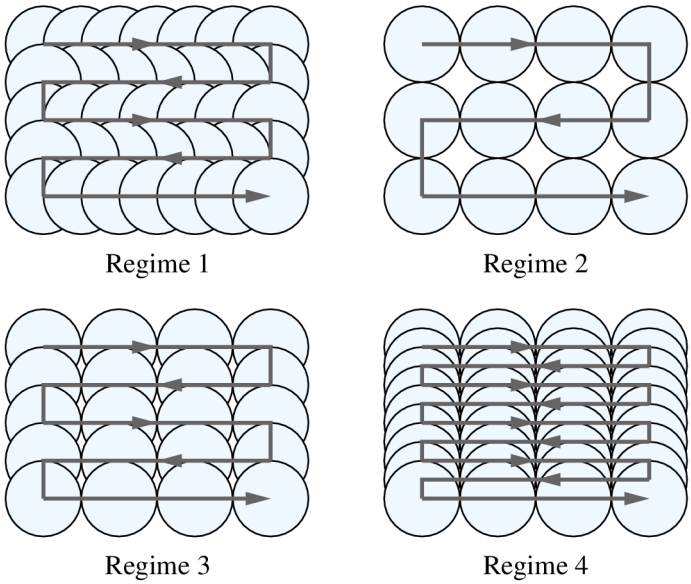

Figure 38: Graphical representation of scanning regimes

A dependence of ablation depth on the total deposited fluence for four cleaning regimes is presented on Figure 39. For regimes 1, 3, 4, ablation depth is almost the same for same deposited fluence. Only for regime 2, ablation depth is slightly lower.

After analysis of the laser treated zones, the following conclusions can be made for the applied regimes:

- Regime 1 with high horizontal overlapping leads to the repeated oxidation of surface during cleaning.
- Regimes 1 – 3 with low and medium vertical overlapping result in high waviness of cleaned surface along vertical direction.
- Only regime 4 gives smooth surface after ablation and doesn't lead to repeated oxidation.

For all further experiments, regime 4 was chosen.

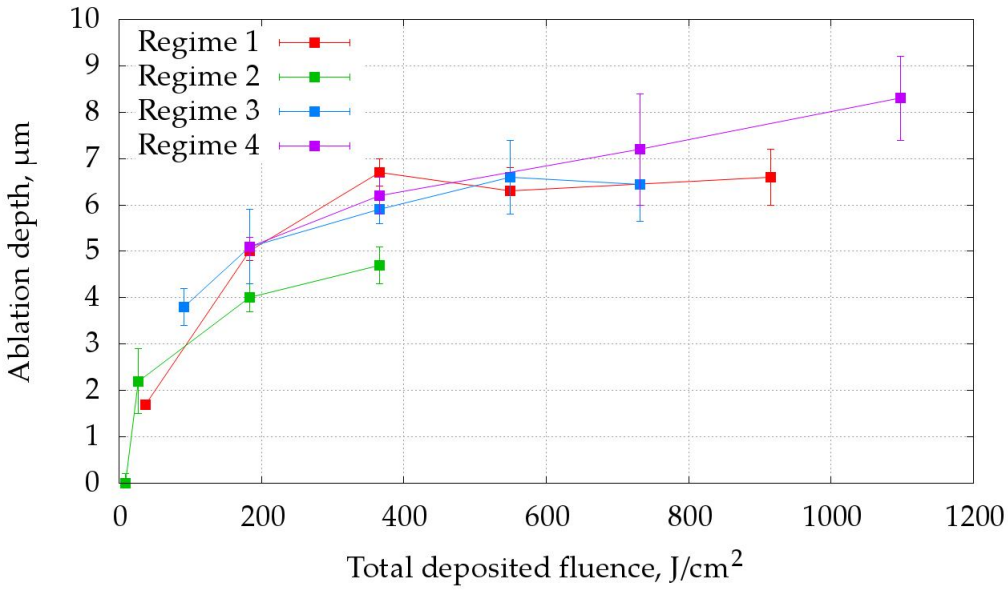

Figure 39: Results of cleaning test

It was shown in Chapter 1 that the majority of the contamination is placed in the oxide layer on the surface of metal. But during long exploitation, the metal substrate also can become radioactive because of the diffusion of contamination into the substrate and the bulk activation. The bulk radioactivity is one of the reasons that limit the feasible decontamination factor. To increase decontamination factor after removing of oxide layer, the metal substrate should be ablated. This procedure is considerably more difficult and demands more time to remove the same thickness of metal than to remove oxide layer. To find the efficiency of stainless steel removal, the dependence of the ablation efficiency as a function of scanning step was measured for a given laser power.

For the measurements, some zones were treated with different scanning regimes and different number of passes. Number of passes was chosen high enough ($N > 5$) to facilitate the measurements of ablation depth. Only the step between successive laser pulses Δx (or scanning speed) and the step between horizontal scanning lines Δy were changed, while all other parameters were constant (beam radius at the sample surface plane $a = 53$ μm, single-pulse fluence $F = 10.5$ J/cm² at the center of Gaussian laser beam). Both vertical and horizontal scanning steps were equal in these experiments ($\Delta x = \Delta y$). The treatment was performed in air at atmospheric pressure.

The results of these measurements are presented on Figure 40, where the ablation efficiency is shown as a function of scanning step normalized to the beam radius. Ablation efficiency was determined as the ratio of the ablation depth to the

total deposited laser fluence. The increase of efficiency in the vicinity of normalized step $\Delta x/a = 0.2$ is associated with the surface oxidation, which occurs at high overlapping. Due to oxidation, the surface reflectivity drops and the energy coupling increases.

Thus, ablation efficiency from 0.0045 up to 0.006 μm/(J/cm²) was obtained for SS ablation.

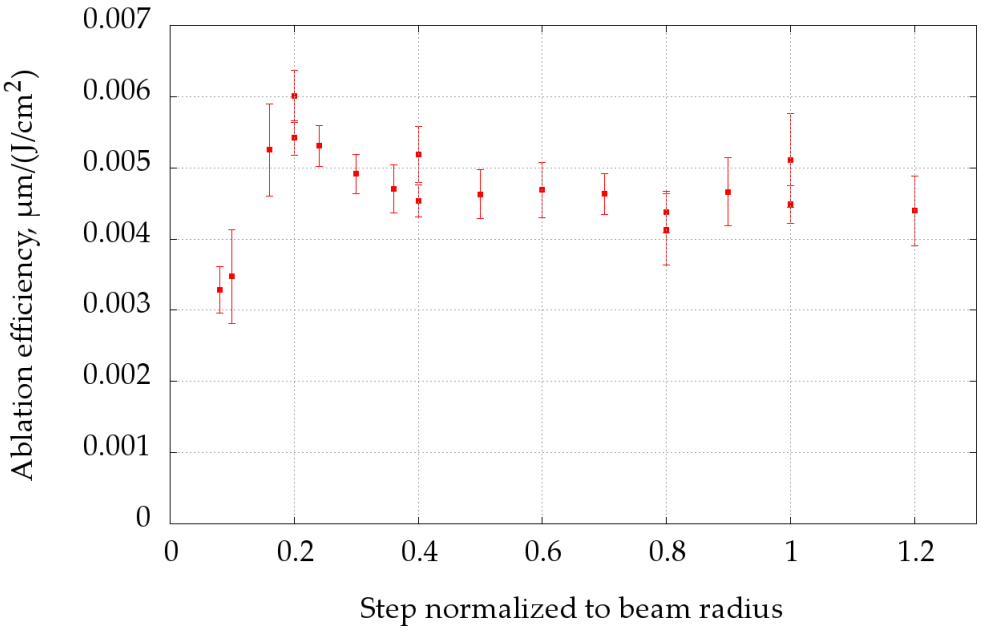

Figure 40: Dependence of the ablation efficiency of stainless steel on the scanning speed

However, this fact cannot explain the drop of efficiency at $\Delta/a = 0.1$. Only two passes were applied to these two zones because the treatment takes very long time at such small steps. Thus, the drop may be attributed to insufficient number of passes ($N < 3$) applied to the zones due to very large time necessary for one pass.

To find the most effective regime of oxide layer removal, we have measured the ablation rate of the oxide layer formed in the furnace as a function of single-pulse fluence. In the measurements, the sample is placed in focal plane of laser beam and the laser power is changing to modify the single-pulse fluence. The scanning regime 4 (see Table 7) is applied. The results of measurements are presented on Figure 41. In the range of 4 – 10.5 J/cm², the ablation rate depends linearly on the fluence. The ablation threshold fluence is determined as a point where this linear dependence crosses abscissa axis. It equals to $F_{th} = 3.1 \pm 0.3$ J/cm².

There is no saturation of ablation rate up to the maximal fluence. As the overall deposited energy is proportional to the single-pulse fluence, this means that the

highest efficiency is observed at 10.5 J/cm² for the scanning regime 4 and it is equal to 0.04 μm/(J/cm²). This means that one pass with laser fluence $F = 10.5$ J/cm² and scanning regime 4 removes 1.46 μm of the oxide layer. The ablation efficiency for oxide layer is ~10 times higher than for SS substrate.

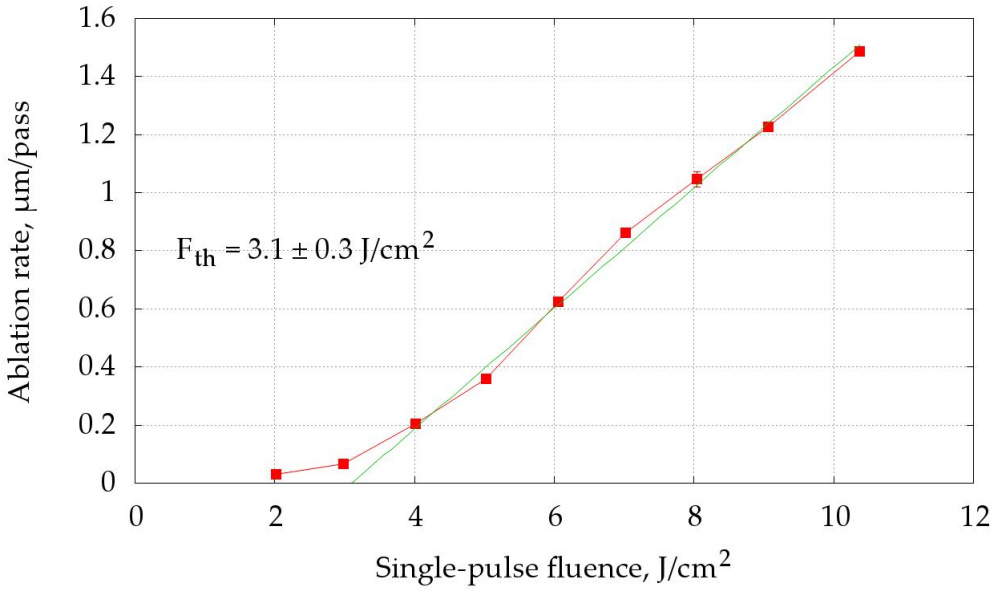

Figure 41: Dependence of the oxide layer ablation rate on the laser fluence. Sample was oxidized in furnace. Oxide layer thichness is 5 – 6 μm.

To investigate the influence of defocusing on the ablation efficiency, an additional measurement was performed for a sample displaced by $\Delta z = 3.14$ mm toward the laser. In this case, the mean laser power of 18.6 W corresponds to the single-pulse fluence of $F = 6$ J/cm², but the overall deposited energy is the same as the scanning regime was not changed. The oxide layer ablation efficiency is 0.03 μm/(J/cm²) for this case, thus indicating that the defocalisation is unfavourable for oxide layer ablation.

The ablation depth as a function of number of passes is presented on **Figure 42** and **Figure 43** for a sample oxidized in furnace and a sample oxidized by laser (regime L, see Table 6 and Figure 36), respectively. On these figures, the ablation rate of oxide layer is indicated as v_l and the ablation rate of stainless steel substrate as v_s. On both figures, the transition between the layer and the substrate is easily observable. The layer thickness can be estimated as 5 – 6 μm for both oxide layers. This correlates with oxygen distributions measured with GDS (see Figure 36, zone L and Figure 37). The ablation rate of laser formed oxide layer is around twice higher than the one of oxide layer produced in furnace, thus indicating that the furnace

layer is harder and more stable. After large number of laser passes, the roughness of cleaned surface increases, thus leading to high errors in ablation depth determination. These errors do not allow us to calculate definitely the ablation rate of stainless steel substrate for the sample oxidized by laser (see **Figure 43**).

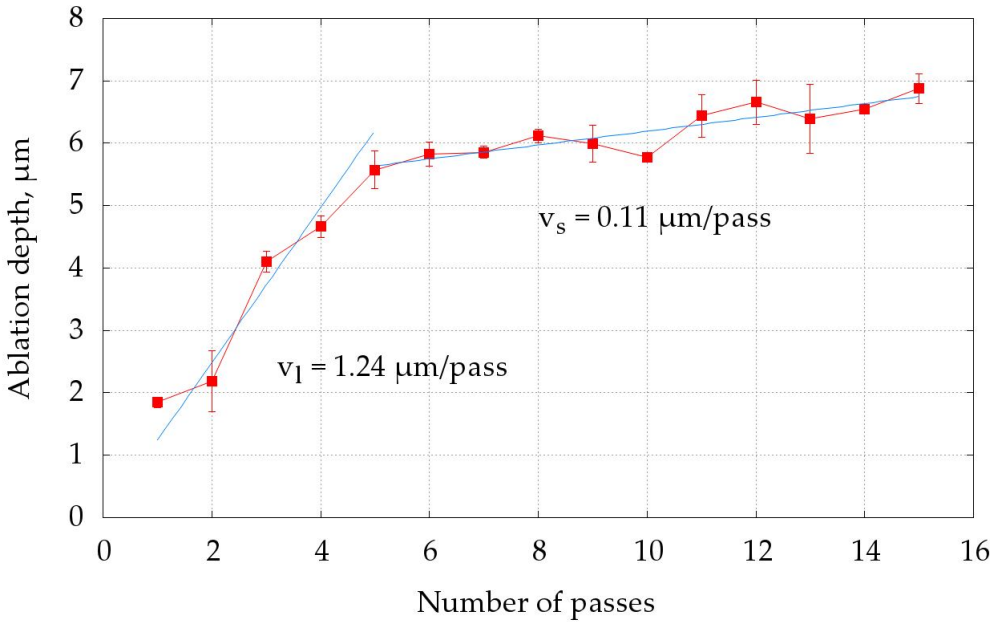

Figure 42: Ablation depth of the oxide layer as a function of the number of passes. Sample was oxidized in furnace.

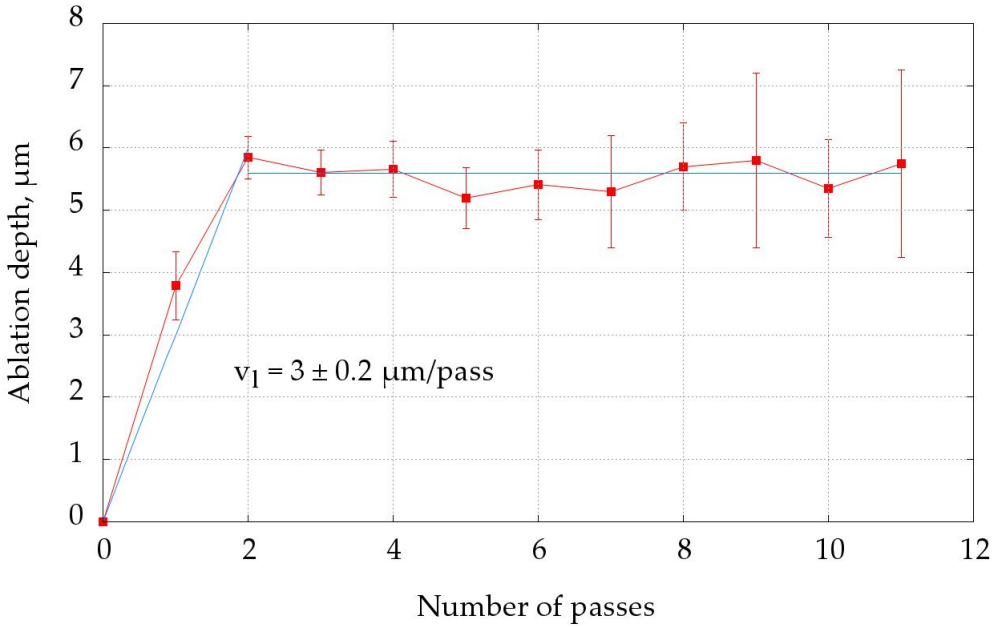

Figure 43: Ablation depth of the oxide layer as a function of the number of passes. Sample oxidized by laser.

The experiment with europium was conducted with the sample oxidized in furnace. The half of the oxidized sample (60 × 30 mm²) was submerged in the water solution of $Eu(NO_3)_3$ (1 g/l) for 24 hours and then dried (see Figure 44).

The GDS analysis of contaminated zone presented on Figure 46 shows that the majority of europium is concentrated at first 200 nm near the surface (black line). However, there is also some amount of contamination that penetrates at the depth of 1 μm. It should be noted that contrary to all other elements, europium has not been calibrated properly and the black curve on spectra indicates the raw signal of europium lines.

The regime 4 with 10 passes was applied for the decontamination test. The area of 55×15 mm² was treated by laser (see Figure 45) and GDS analysis of this area has been performed once again (see Figure 47).

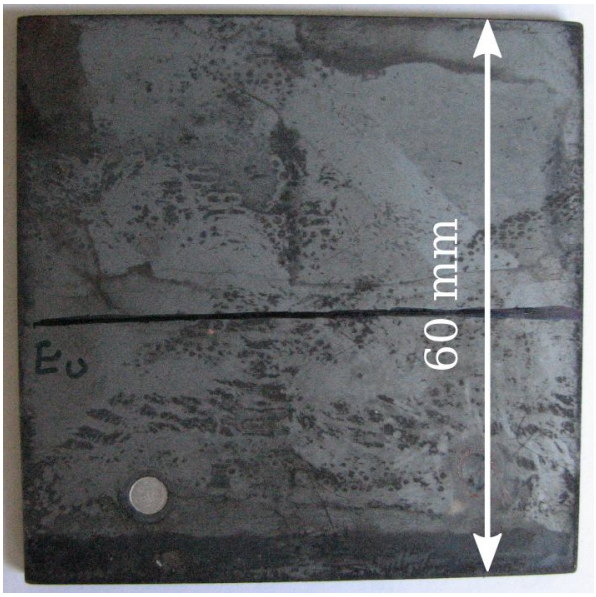

Figure 44: Oxidized SS sample after europium application (bottom zone) and GDS analysis (round spot)

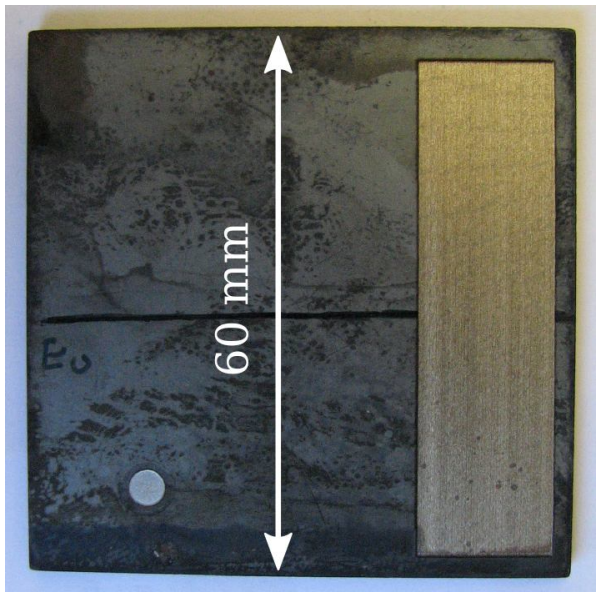

Figure 45: Oxidized SS sample after cleaning by laser (right zone, 16 × 55 mm²)

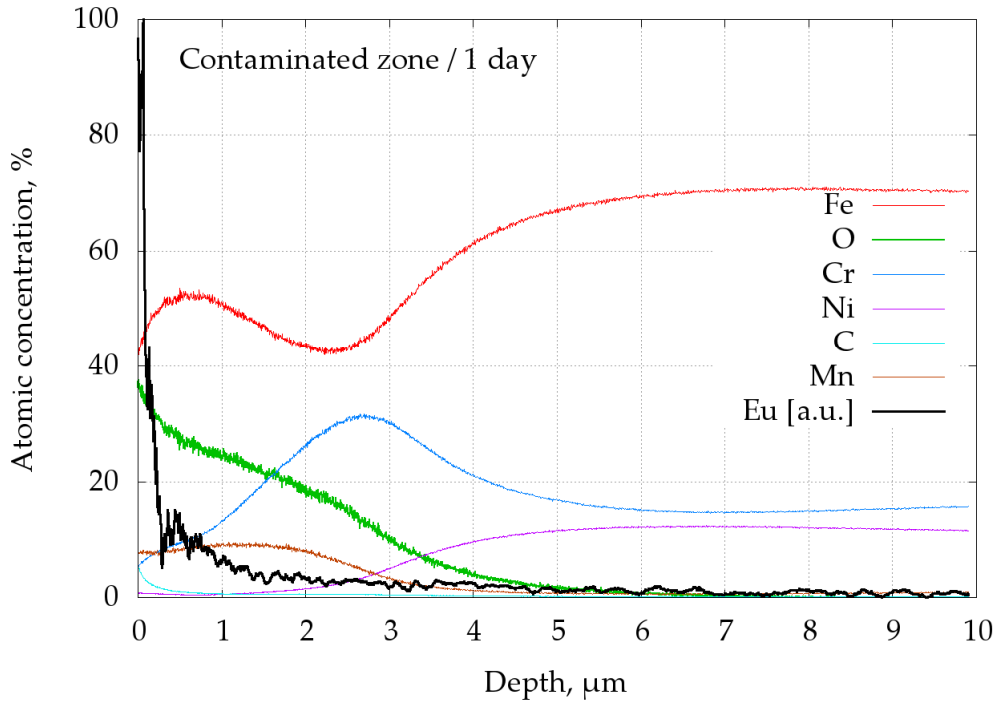

Figure 46: GDS spectrum of the oxidized SS sample contaminated with Eu

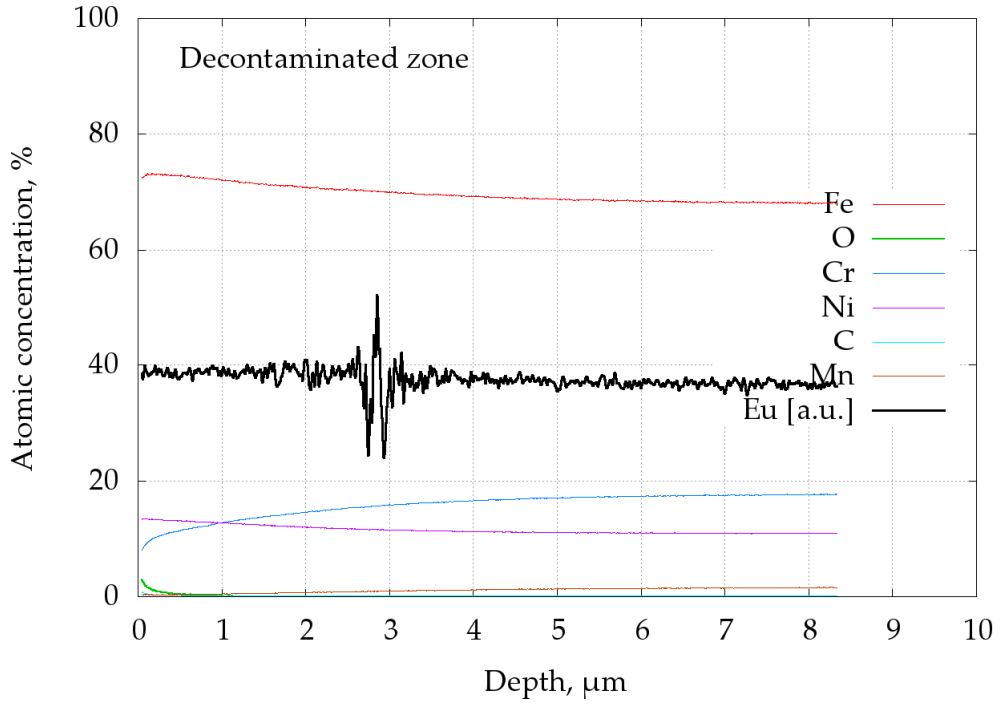

Figure 47: GDS spectrum of the laser cleaned zone of the sample contaminated with Eu

The overall amount of europium was determined with chemical etching method. Before cleaning, it was 32 μg/cm^2 (1.26·10^{17} atom/cm^{-2}), but after cleaning, it

droped down to < 0.1 μg/cm² (this is the method detection limit). Thus, the decontamination factor of more than 320 is reached.

If the same quantity of ^{60}Co was applied to the sample surface, its surface activity would equal to $A = \frac{\ln 2}{T_{1/2}} \frac{m_{Eu} N_a}{\mu_{Eu}} = 5.3$ MBq/cm² before cleaning and to $A <$ 1.7 MBq/cm² after cleaning.

The second test was performed with Na as a contaminant. AISI 304L sample oxidized in furnace was exposed to NaCl solution. The GDS spectrum of contaminated sample is presented on Figure 48. As above with Eu, the most part of Na is concentrated in the first 500 nm near the surface of oxide layer.

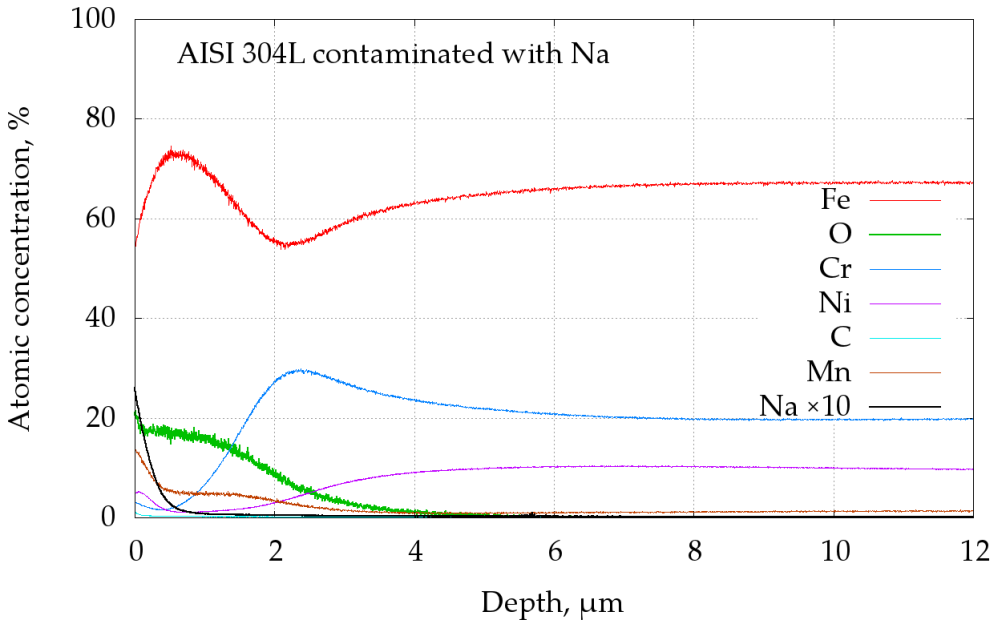

Figure 48: GDS spectrum of AISI 304L sample contaminated with Na

For cleaning tests, the optimal scanning regime 4 was applied. Two zones were cleaned to check how the contamination is removed: with 1 laser pass and with 5 laser passes. The GDS spectra of cleaned zones are presented on Figure 49 and Figure 50. As it can be seen, even after 1 pass, almost all Na is gone, though the oxide layer is still there.

By integration Na signal over the time, we can calculate the quantities proportional to the overall amount of Na in the layer. With this technique, we obtain DF = 78 after 1 laser pass (see Figure 49) and DF ≈ 1500 after 5 passes (see Figure 50).

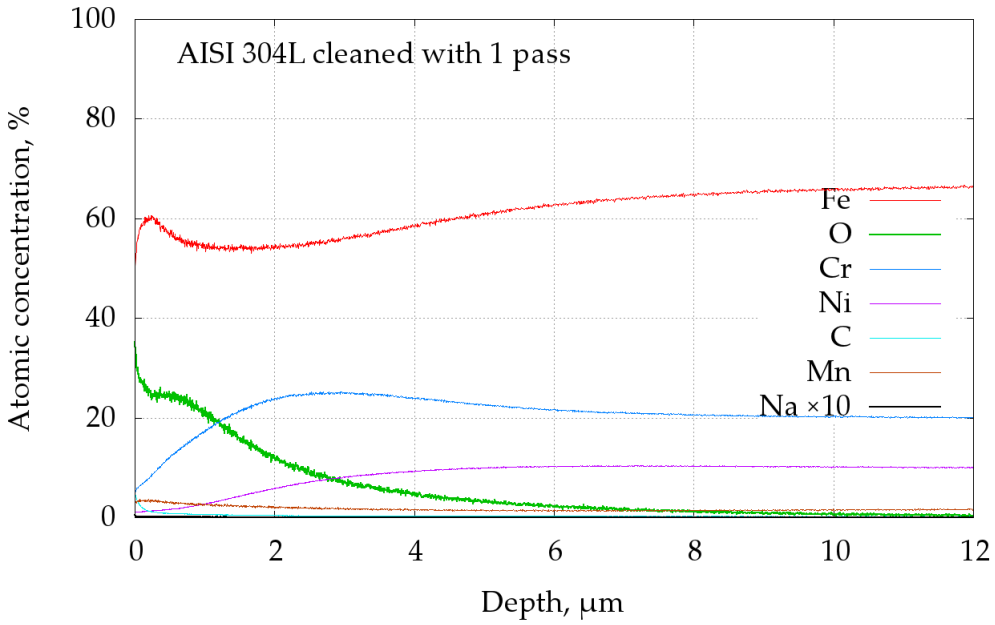

Figure 49: GDS spectrum of 1-pass decontaminated zone of the sample contaminated with Na

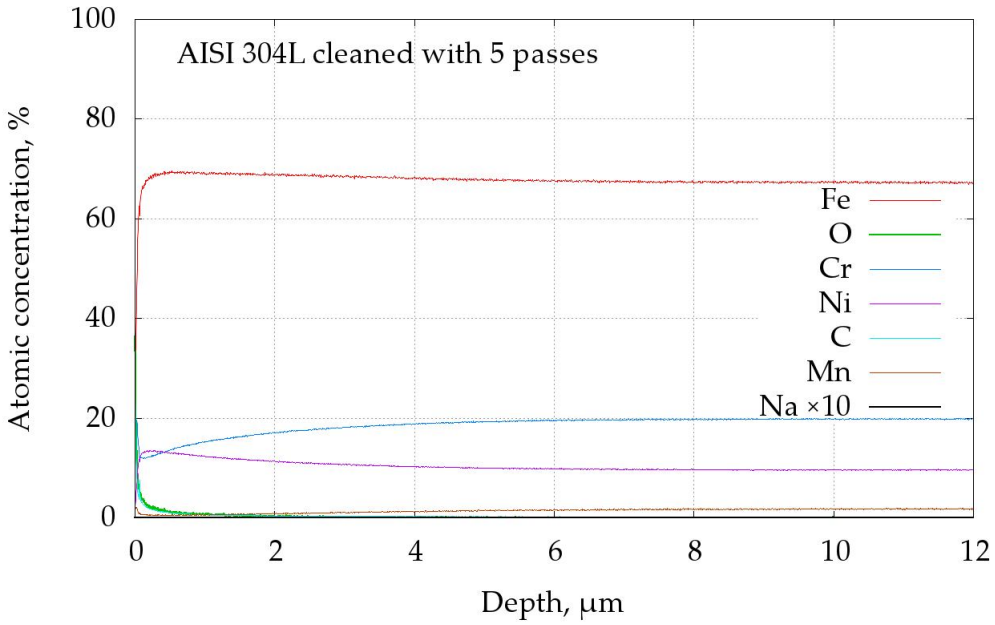

Figure 50: GDS spectrum of 5-passes decontaminated zone of the sample contaminated with Na

4.1.4 Corrosion test

To investigate the influence of laser treatment (decontamination) on corrosion resistance of SS, the corrosion tests were performed for a virgin SS sample and for a sample oxidized in the furnace and decontaminated by laser ablation. Laser cleaning was performed with scanning regime 4 ($\Delta x = 100$ μm, $\Delta y = 25$ μm, $v_x = 2000$ mm/s,

F = 10.5 J/cm²); 10 passes were applied. After cleaning, an additional laser treatment aimed to enhance the corrosion resistance of the sample was applied to the cleaned surface with the following parameters: laser power P = 6 W, fluence F = 3.25 J/cm², v_x = 1000 mm/s, $\Delta x = \Delta y$ = 50 μm. These parameters were chosen on the results from [87].

The results of corrosion test are presented on Figure 51. As it can be seen, the current due to electrochemical reaction on the surface is much larger for cleaned surface than for virgin one. This means that the corrosion resistance is drastically decreased after oxidation and laser cleaning.

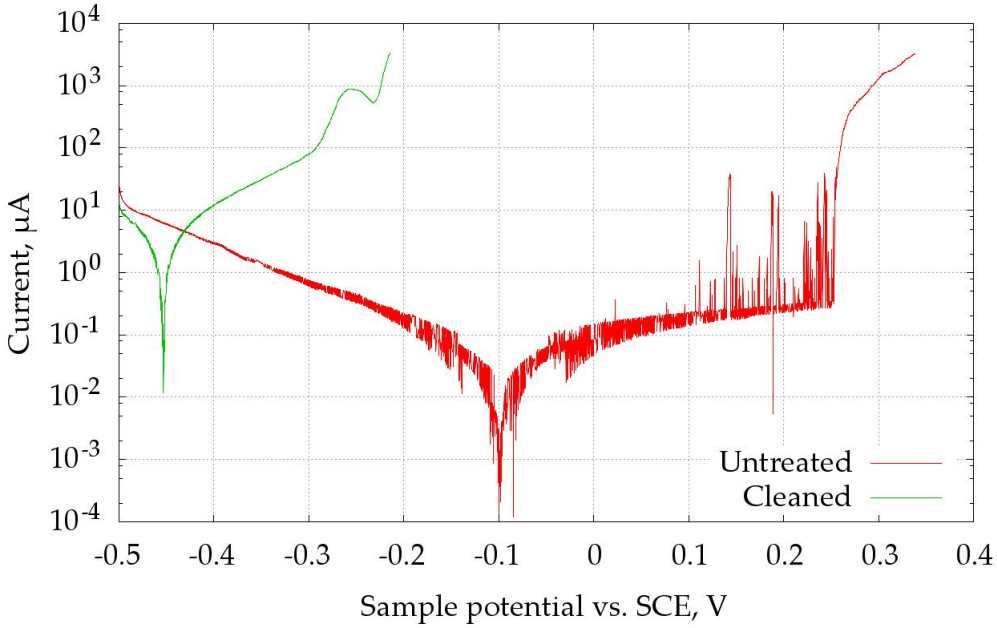

Figure 51: Current-voltage characteristic of the sample after laser cleaning and laser enhancement treatment

To understand the reasons of such degradation, the GDS spectrum of cleaned surface was measured (see Figure 52).

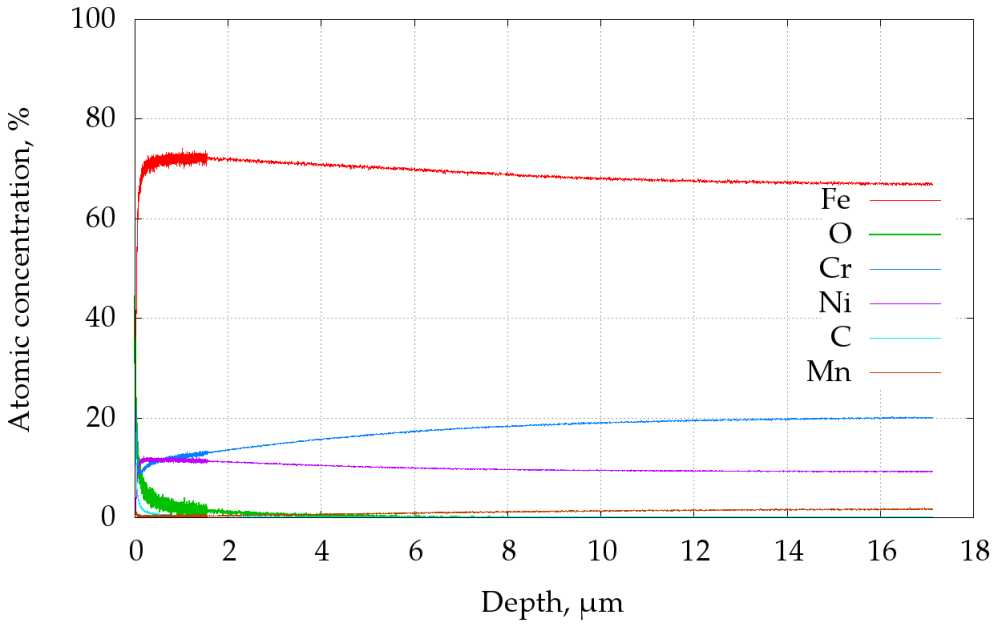

Figure 52: GDS spectrum of the sample after laser cleaning and laser enhancement

The stainless steel AISI 304L normally has ~18% of Cr contents. It plays an important role in formation of a passive film of chromium oxide, which prevents further surface corrosion and blocks corrosion from spreading into the metal internal structure. Passivation only occurs if the proportion of chromium is high enough. After cleaning, the concentration of chromium drops significantly in several micrometers near the surface. Thus, the protective passive film cannot form and the corrosion resistance decreases.

After cleaning, small black points remain on the surface of sample. Measurements of these points carried out with the optical profilometer reveal that they are small dips of about 50 – 100 μm in diameter and ~20 μm in depth. Presumably, the dips contain an oxide. It is likely that they are formed due to oxidation in the furnace. They also can affect negatively the corrosion resistance of the stainless steel surface.

4.1.5 Conclusions

The possibility of laser decontamination of oxidized metallic surfaces by ytterbium fiber laser was shown. For these experiments, the oxidation of stainless steel by laser and in furnace was performed. The artificially oxidized and contaminated with Eu and Na sample were prepared. Decontamination factor (concentration of contaminant before and after cleaning) of 300 for Eu-contaminated sample was obtained after deposition of 372 J/cm^2. For Na-contaminated sample, decontamination factor was DF = 1500 after deposition of 186 J/cm^2. Such

decontamination factors are considered as sufficient to clean radioactive wastes. Laser cleaning productivity of 0.001 m^2/W×hour is demonstrated for Eu-contaminated sample. Thus, with the fiber laser of 1 kW mean power, 1 m^2 of a contaminated surface can be cleaned in 1 hour.

However, it was found that after laser cleaning, the corrosion resistance of stainless steel surface had significantly degraded. This happened because several micrometers in-depth of metal surface had become chromium-depleted due to oxidation and laser cleaning.

4.2 Laser ablation and laser heating of ITER-like samples

During operation of modern fusion devices, tritium (which is the essential component of fusion reaction) becomes trapped on the surface of Plasma Facing Components (PFCs). For safety reasons, the overall quantity of tritium is limited for each component. For the ITER vessel, this limit is 330 g for mobilisable tritium (in deposited layer of PFCs and in dust) [88]. The periodical cleaning of all PFCs is necessary to avoid the excess of the permitted values of tritium quantity. That is why it is of great importance to find an efficient method for PFCs decontamination. One of the alterative supplementary techniques is surface cleaning by laser ablation. This is a non-contact method and it may be used in vacuum or at reduced pressure. It produces small amount of wastes in aerosol/solid state and can be fully automated to reduce personnel exposure.

In this section, we investigate laser ablation and laser heating of ITER-like samples, which resemble PFC surfaces of future ITER installation. ITER-like samples consist of a metal substrate (usually stainless steel or tungsten) and a deposited layer. Deposited layer can contain tungsten, beryllium, hydrogen and carbon in amorphous phase.

In this section, the ablation test of ITER-like samples is described. The ablation threshold fluences and cleaning efficiencies are determined. The laser heating temperatures of ITER-like samples are measured. The comparison of experimentally measured heating temperatures with theoretical ones is performed for laser heating model validation.

4.2.1 Samples

The following ITER-like samples were used in the laser ablation and laser heating experiments (see Figure 53):

- **SS/W/W+DLC(H)**. Tungsten-DLC layer with hydrogen content on the AISI 304 stainless steel substrate with W marker layer of 10 nm thickness. Layer thickness: 1.5 – 2 μm. Substrate thickness: 10 mm. Sample diameter: 45 mm.
- **W/W+αCH**. Sequentially deposited layer composed of tungsten and amorphous carbon. Layer thickness: 1 – 2 μm (depending on the zone). The substrates were 30×30 mm² of 3 mm thickness. The zone with the deposited layer is 25 mm diameter circle. The details of layer deposition are described in [89].

SS/W/W+DLC(H)

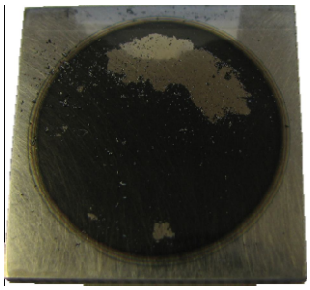

W/W+αCH

Figure 53: Photos of ITER-like samples

To calculate absolute temperature rise due to the known laser impact, one has to know the sample reflectivities at the laser wavelength. We measure samples total reflectivities with the set-up described in section 3.3. The obtained values are presented in Table 8.

Table 8: Reflectivities of the samples measured with the integrating sphere

Sample	Total reflectivity
SS substrate	0.62 ± 0.04
SS/W/W+DLC(H)	0.17 ± 0.03
W substrate	0.58 ± 0.07
W/W+αCH	0.14 ± 0.06

To measure layer thicknesses, SS/W/W+DLC(H) sample with stainless steel substrate were cut (Persi Mecatome T201A) and embedded into a resin (PolyFast, Struers ProntoPress-20). After that, it was mechanically polished with 4000 grit SiC paper (2.5 μm median particle size) and then with polishing cloths (Struers MD-Cloths) and diamond suspension down to 1 μm (Struers DP-Suspension). After

polishing, sample cut was analysed with a Scanning Electron Microscope (JEOL MEB FEG 7000F).

The thickness of the layer on the W/W+αCH sample was measured with both mechanical and optical profilometers using the various zones where the layer was detached from the substrate. It was found that the layer thickness changes over the sample surface from 1 µm at the circumfery of deposited area up to ~2 µm at the centre. The sample surface profile is presented on Figure 54.

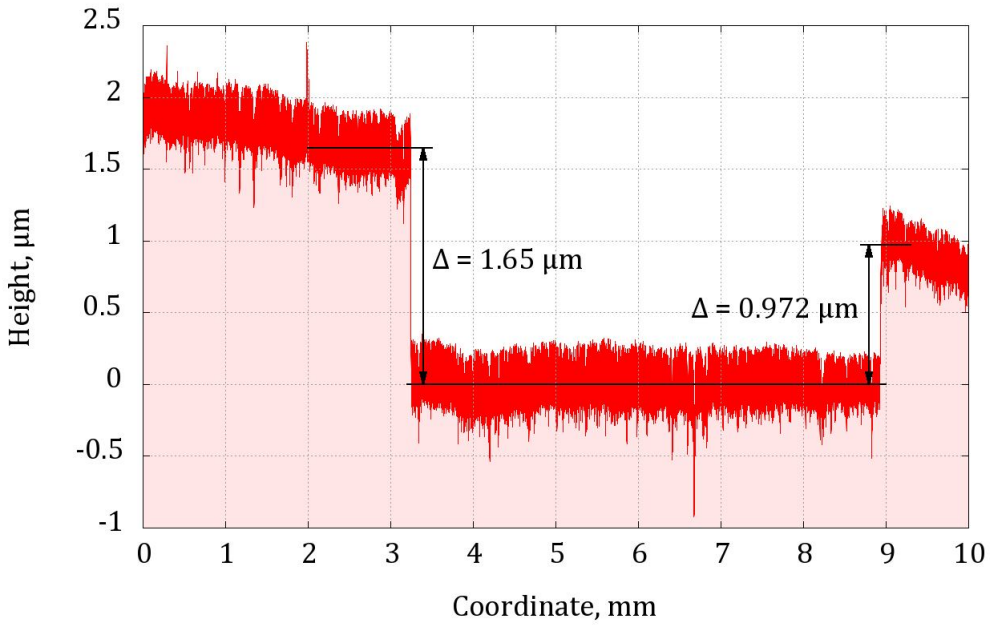

Figure 54: Surface profile of the zone with the detached layer on the W/W+αCH sample. This profile is measured with the mechanical profilometer Mahr.

4.2.2 Ablation tests

Ablation tests were performed using the DetriLaser laser system. The surface of SS/W/W+DLC(H) sample was scanned by the laser beam line by line, where each line corresponds to different laser fluences from 1.7 to 9.7 J/cm^2. Scanning speed was high enough (v = 6000 mm/s) to ensure that each pulse produces well-separated spot on the surface. Profiles of these zones with laser spots measured with optical profilometer are presented on Figure 55. The green line shows normalized laser beam profile.

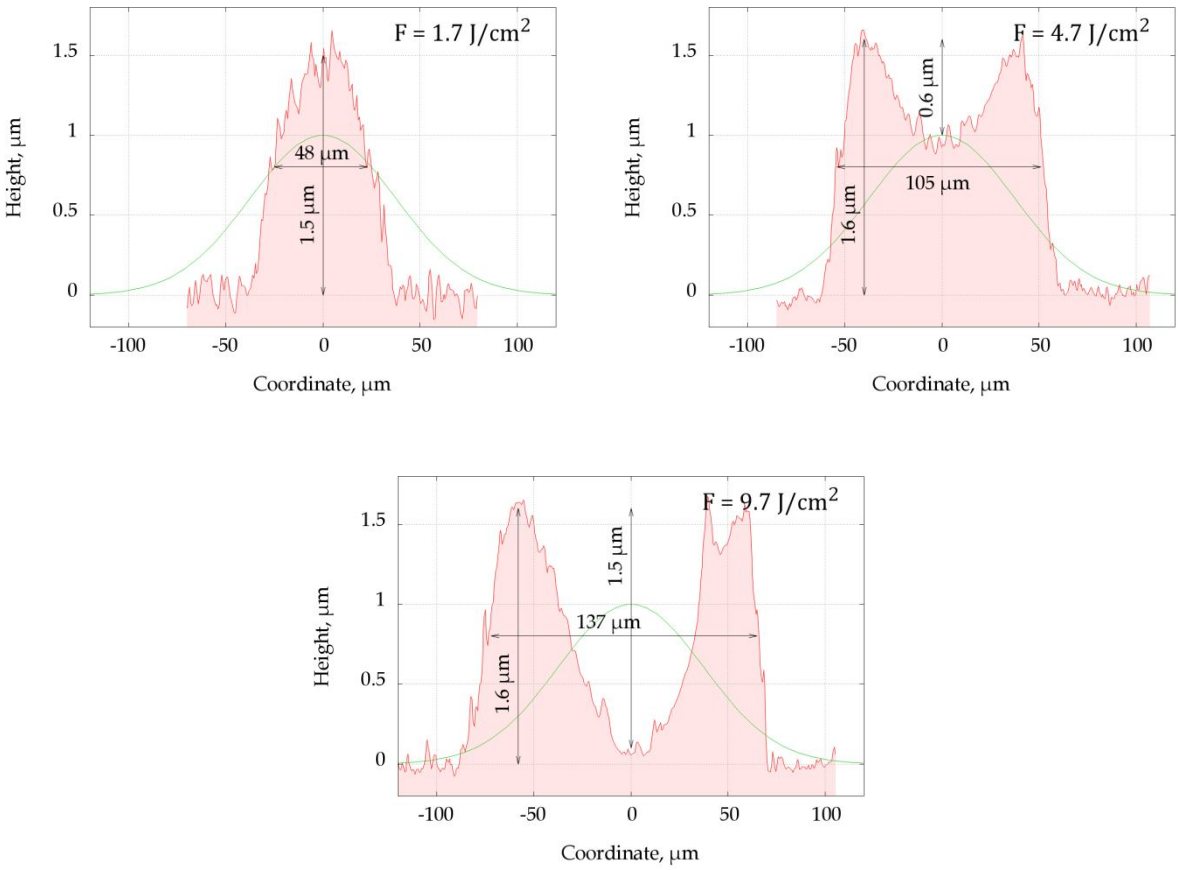

Figure 55: Profiles of craters formed under the action of laser pulses of different fluence

One can see that the bump is always formed on the surface under the action of laser pulse on the deposited layer. This can be attributed to the plastic deformations of the layer due to laser heating. The dependences of bump height and dip depth on the laser fluence are presented on **Figure 56**. With the increase in laser fluence, the bump is widening, but its height remains constant. Also, at the centre of the bump, the dip begins to form for the fluences higher than ~2 J/cm^2. The depth of this dip increases with the increase in laser fluence.

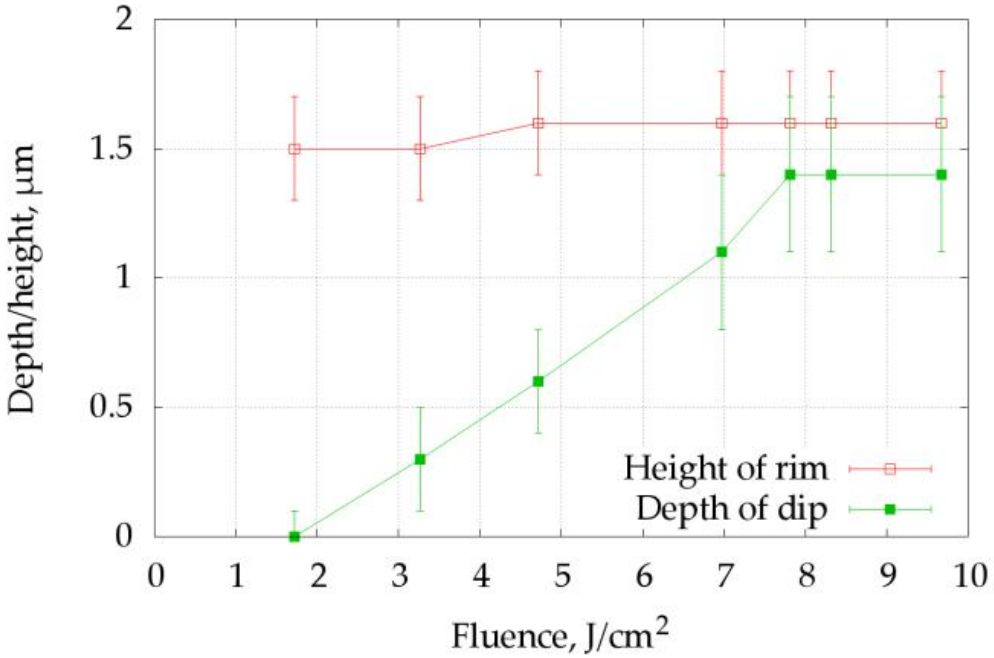

Figure 56: Dependence of bump height and dip depth on the laser fluence for craters formed on the surface of SS/W/W+DLC(H) sample

"Burning paper" method (see section 3.4.1) is used to determine damage and ablation thresholds for SS/W/W+DLC(H) sample. **Figure 57** shows the experimental data on the bump and dip widths together with the fitted theoretical curves. The widths were measured not at the half of the maximum, but rather at the very foot of the bump and at the very beginning of dip, respectively. For SS/W/W+DLC(H) sample, the obtained threshold fluences are

- F_{th} = 1.16 ± 0.10 J/cm² for bump formation;
- F_{th} = 2.3 ± 0.4 J/cm² for dip formation.

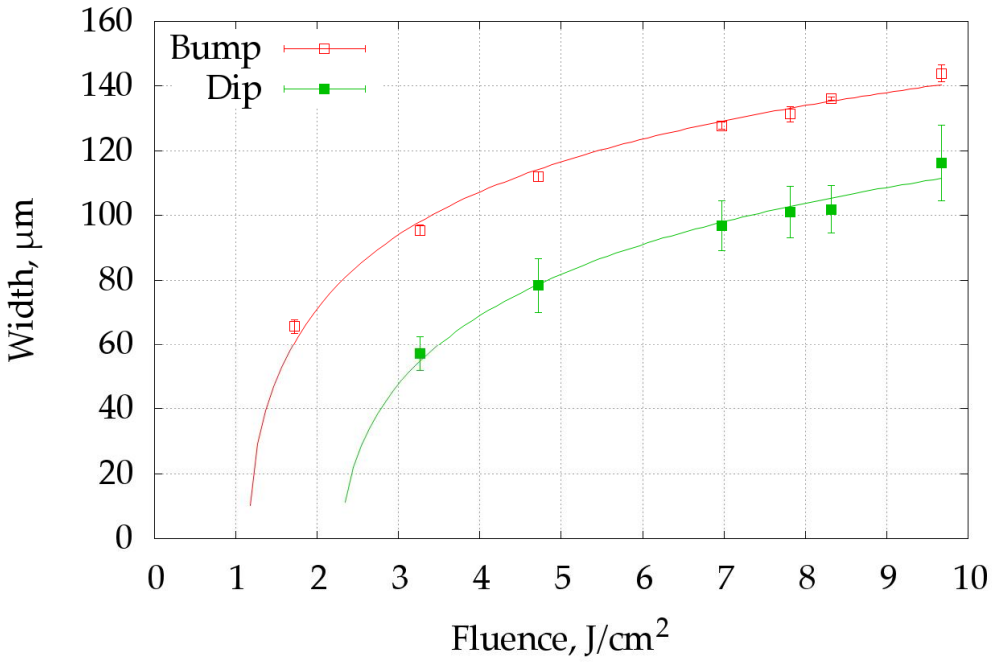

Figure 57: Widths of bump and dip as functions of laser fluence for craters formed on the surface of SS/W/W+DLC(H) sample. The experimental results are indicated by points. Lines show the theoretical curves obtained by fitting dependence (119) to the experimental points.

On Figure 58, photos and profiles of craters formed on the surface of W/W+αCH sample under the action of well-separated laser pulses with fluences F = 10.4 J/cm^2 and F = 1.03 J/cm^2 are presented. The green curve indicates the laser beam profile. It can be seen that at F = 10.4 J/cm^2, the whole layer is removed by a single pulse, whereas at F = 1.03 J/cm^2, only part of the layer is removed. The ablation threshold, i.e. the threshold fluence at which the ablation of the layer begins, is determined by analyzing outer diameters of craters, whereas the threshold of the whole layer removal is determined by analyzing inner diameters. The results of diameters measurements and the curves obtained by fit are presented on Figure 59.

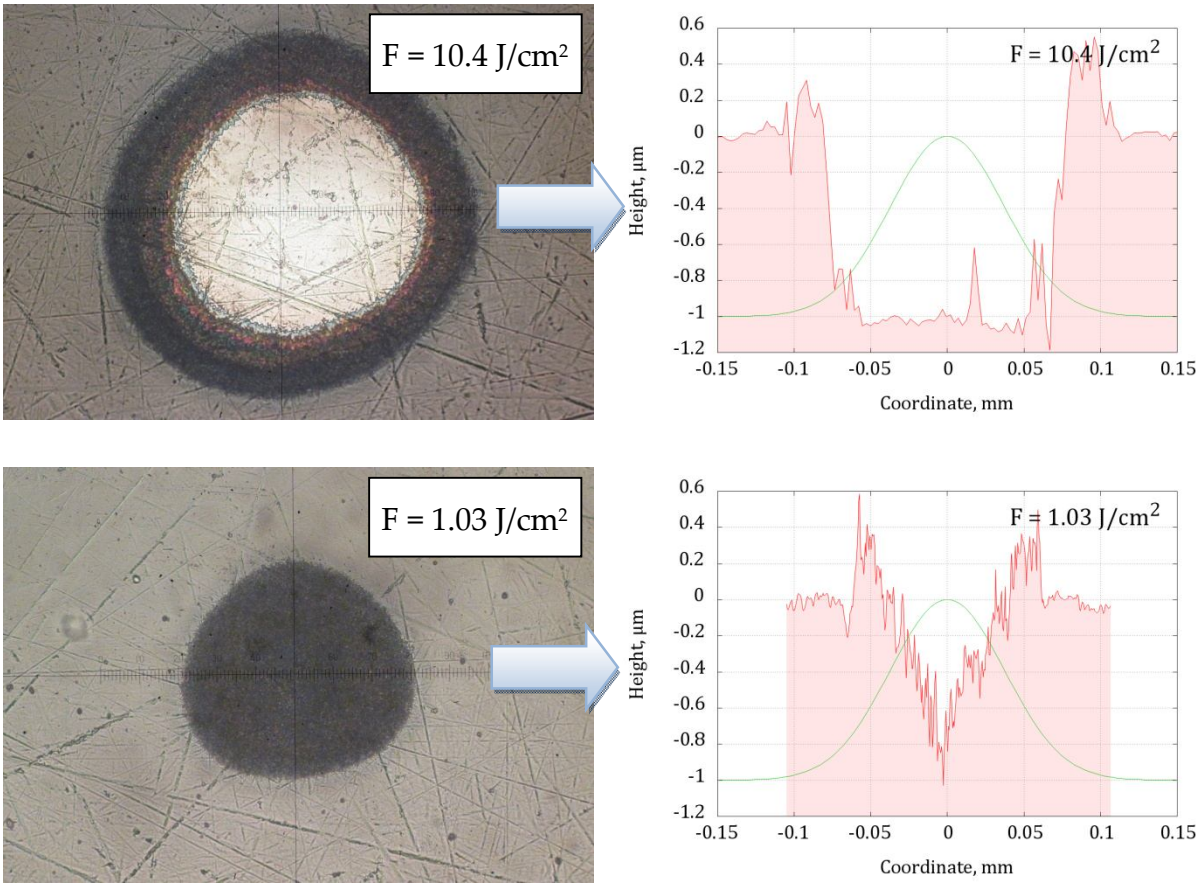

Figure 58: Photos and 1D profiles of craters formed on the surface of W/W+αCH sample under the action of laser pulses with fluence F = 10.4 J/cm² and F = 1.03 J/cm²

The ablation threshold of the layer on W/W+αCH sample is only 0.27 ± 0.03 J/cm². And the laser fluence, at which the complete removal of the deposited layer starts, is 1.33 ± 0.19 J/cm².

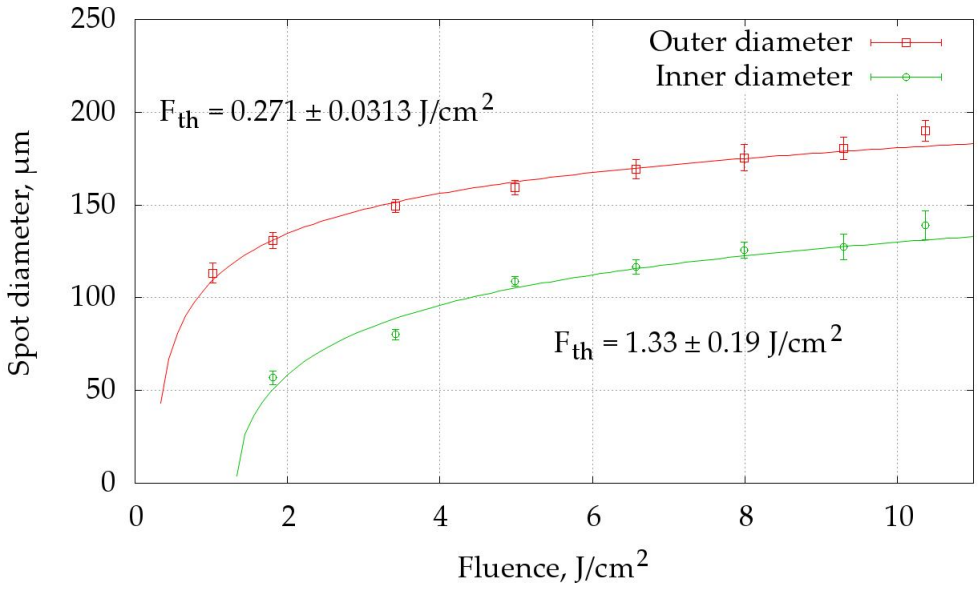

Figure 59: Dependence of the inner and outer crater diameter on the laser fluence for W/W+αCH sample

After determination of threshold fluences, the cleaning tests were performed with W/W+αCH sample. The sample photo after the tests is shown on Figure 60. The applied regimes, measured ablation depths and cleaning productivity are presented in Table 9 for each zone. The cleaning productivity shows how many square meters of the surface under consideration can be cleaned in one hour using a 1 W laser.

For zones 1–5, the sample was placed 10 ± 1 mm behind the focal plane. For this case, the beam radius is 108.6 μm at 1/*e* intensity level. For zones 6-8, the sample was placed in the focal plane.

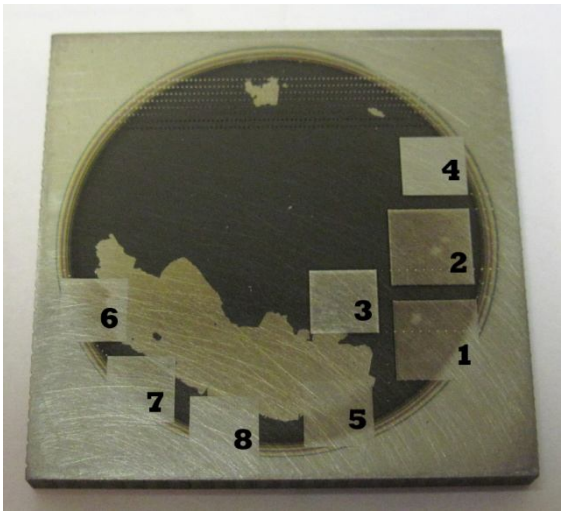

Figure 60: Photo of the sample W/W+αCH

Table 9: Characteristics of cleaned zones

	Regime: Power; Fluence; Step; Passes	Ablation depth	Productivity
Zone 1	5.06 W; 0.68 J/cm² 0.07 mm; 1 pass	1.3927 ± 0.032 µm	0.071 m²/hour/W
Zone 2	8.85 W; 1.2 J/cm² 0.07 mm; 1 pass	1.7025 ± 0.025 µm	0.04 m²/hour/W
Zone 3	14.1 W; 1.9 J/cm² 0.05 mm ; 1 pass	1.8123 ± 0.036 µm	0.013 m²/hour/W
Zone 4	8.85 W; 1.2 J/cm² 0.07 mm; 2 pass	1.4205 ± 0.027 µm	0.02 m²/hour/W
Zone 5	5.06 W; 0.68 J/cm² 0.08 mm; 2 pass	0.881 ± 0.014 µm	0.043 m²/hour/W
Zone 6	8.85 W; 5 J/cm² 0.05 mm; 1 pass	0.887 ± 0.02 µm	0.02 m²/hour/W
Zone 7	5.94 W; 3.4 J/cm² 0.05 mm; 2 passes	0.984 ± 0.019 µm	0.015 m²/hour/W
Zone 8	5.94 W; 3.4 J/cm² 0.025 mm; 2 passes	1.077 ± 0.027 µm	0.004 m²/hour/W

From the sample photo (see **Figure 60**), it is seen that different regimes give different cleaning quality. We cannot determine which part of the layer was removed by each regime because the thickness of layer is not constant (see section 4.2.1 and Figure 54). From the measurement with profilometer, it seems that all regimes remove the layer completely. Even if there are some differences in the cleaned surface level for the zones, they cannot be determined due to the roughness of surface.

Hence, the regime applied for zone 1 (fluence $F = 0.68$ J/cm², scanning step $\Delta x = \Delta y = 70$ µm, 1 pass) is the most productive among the tested regimes. Despite the fact that this fluence is below the threshold for complete layer removal by one pulse, the layer was entirely removed due to pulses overlapping.

4.2.3 Laser heating measurements

Laser heating measurements were performed only with SS/W/W+DLC(H) sample. They are aimed to verify the heating model developed in CEA Saclay [55].

The thermophysical properties of stainless steel substrate can vary in a wide range depending on heat and sample preparation. The properties of the deposited layer are not generally known. To obtain a good correspondence between measured and calculated heating temperatures, it is necessary to determine the thermophysical properties accurately.

Stainless steel substrate. Thermal diffusivity was directly measured by active lock-in pyrometry as $\kappa = 3.6 \cdot 10^{-6}$ m²/s [90]. To determine the thermal conductivity, the laser heating temperatures of stainless steel substrate were measured. In order to remove the layer, the sample was treated with DetriLaser system.

Before heating measurements, the substrate was preheated to the temperature $T_h = 507$ K with electric heater. The emissivity $\varepsilon = 0.26$ was obtained. The obtained heating temperature of SS substrate together with calculated values are presented on Figure 61.

Table 10 presents the parameters of stainless steel, which were applied in calculations. The density and absorption coefficient were taken from [91], [92]. The reflection coefficient was measured with the integrating sphere. The thermal diffusivity was determined by active lock-in pyrometry [90]. The thermal conductivity was determined by fitting of theoretical heating temperatures to the experimental one. The heat capacity was calculated using thermal diffusivity and thermal conductivity.

Table 10: Properties of stainless steel substrate of the sample SS/W/W+DLC(H), which were applied for calculations

Parameter	Symbol	Fitted value
Thermal conductivity	k	17.4 ± 0.1 W/m·K
Density	ρ	8000 kg/m³
Specific heat capacity	c	604 ± 3 J/kg·K
Volumetric heat capacity	ρc	4.8 MJ/m³·K
Thermal diffusivity	κ	$3.6 \cdot 10^{-6}$ m²/s
Absorption coefficient	α	36 μm⁻¹
Reflection coefficient	R	0.62 ± 0.04
Laser beam radius	a	1.8 mm

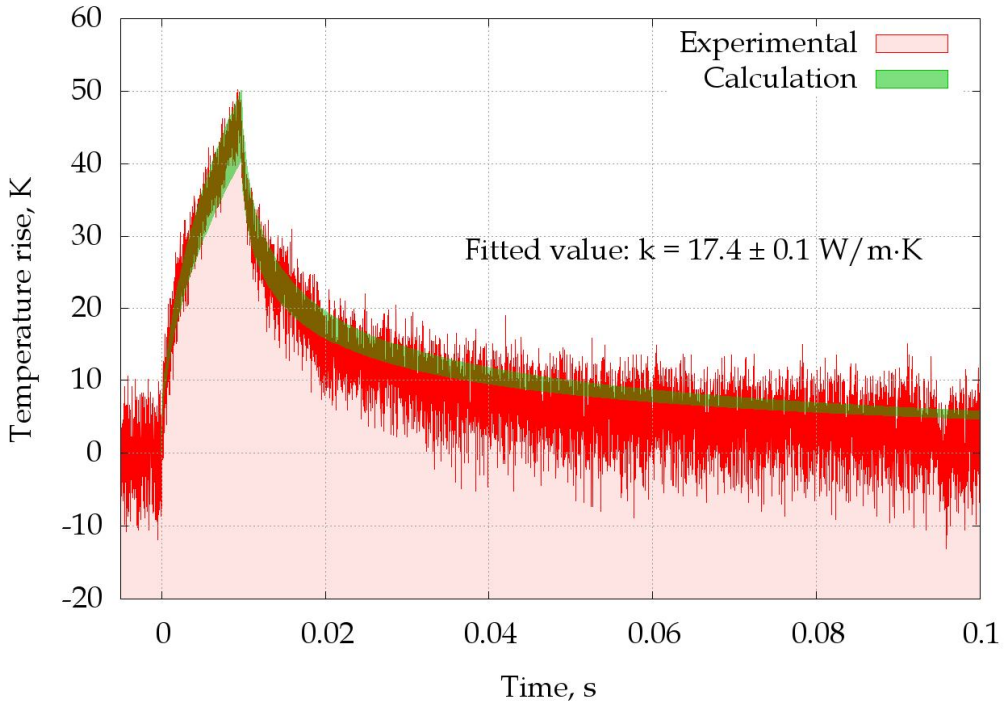

Figure 61: Calculated and experimental heating temperatures for the cleaned part of the sample SS/W/W+DLC(H)

Deposited layer. Before heating measurements, the sample was preheated to the temperature $T_h = 507$ K. The emissivity for the sample SS/W/W+DLC(H) with layer was determined as $\varepsilon = 0.5 \pm 0.1$ using procedure presented in section 3.4.2.

The parameters applied for the calculation of laser heating temperatures for the sample SS/W/W+DLC(H) with the layer are summarized in **Table 11**. The properties of the layer were obtained by active lock-in pyrometry measurements. On **Figure 62**, the measured laser heating temperature and the calculated one are presented. The theoretical and experimental curves conform well.

Table 11: Properties of the layer of the sample SS/W/W+DLC(H), which were applied for calculations

Parameter	Symbol	Lock-in value [90]
Thermal conductivity	k	30 W/m·K
Density	ρ	1000 kg/m^3
Specific heat capacity	c	3000 J/kg·K
Volumetric heat capacity	ρc	3 MJ/m^3·K
Thermal diffusivity	κ	10^{-5} m^2/s
Absorption coefficient	α	11 μm^{-1}
Reflection coefficient	R	0.17
Layer thickness	d	6 μm
Thermal contact	h	3333 kW/m^2·K
Laser beam radius	a	1.8 mm

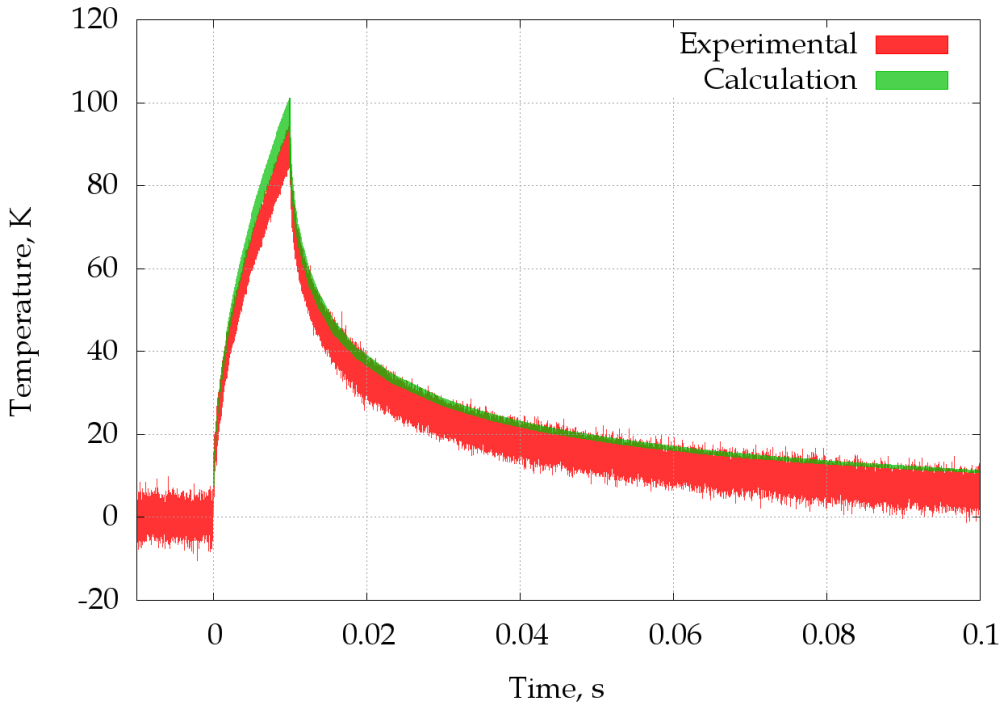

Figure 62: Calculated and experimental heating temperatures for the sample SS/W/W+DLC(H) with layer

It should be also noted that, for such thin layers (~1 μm), with the used pyrometer of 10 μs resolution, we cannot reliably check the layer parameters by comparing experimental and theoretical results on laser heating. This is due to the

fact that at the time of used laser pulses (10 ms), the heat affected depth is >> 1 μm and the heating temperature does not depend strongly on the layer properties; rather, it depends on these of substrate ones. To get a strong dependence on layer parameters, it is necessary to reduce the laser pulse duration down to 1 μs or to apply thicker layers.

4.2.4 Conclusions

For laser ablation of ITER-like surfaces, it was found that the deposited layer containing a significant part of carbon can be removed by the laser without damage of the substrate because of great difference in ablation thresholds for the layer and the substrate. A productivity of 0.071 m^2/hour/W was obtained for the W+αCH layer of 1.4 μm thickness.

It was shown that at low fluences, the carbon-containing layer deforms mechanically because of thermo-mechanical stresses induced in it by rapid laser heating. At higher fluences $F > 2$ J/cm^2, the layer begins to ablate. This effect can be used to remove deposited layer without its destruction.

However, if the layer doesn't contain carbon, but only a metal (tungsten, aluminium) with a low hydrogen/deuterium content, its ablation threshold increases due to higher reflectivity of the layer. Such layers, especially made of tungsten, cannot be removed by laser ablation without substrate damage/ablation. The method of detritiation by laser heating can be applied in this case.

4.3 Mirrors

For laser cleaning of metallic mirrors, one has to ensure the absence of damage of mirror surface during cleaning. This can be achieved by choosing laser fluence below the damage threshold of mirror surface. In this work, we have measured the damage thresholds for several types of mirrors and compared them with the calculated ones.

Knowledge of damage thresholds is necessary to avoid the degradation of substrate during laser cleaning. In Chapter 2, the model allowing damage threshold determination of metal substrate is presented. In this section, the experimental determination of damage thresholds for molybdenum (Mo) and stainless steel AISI 316 (SS) mirrors is described. The comparison between calculated and measured thresholds is discussed. The analysis of damage spots formed under the laser action is presented.

4.3.1 Samples

Two molybdenum and one AISI 316L stainless steel unused mirrors (not exposed to JET plasma) were under our experimental investigations (see Figure 63). The SS mirror and one Mo mirror are of 10 mm × 10 mm × 10 mm dimensions with one optically polished surface (0.02 – 0.06 μm roughness) . The other Mo mirror was a round shape with diameter d = 25 mm and thickness h = 4.7 mm. It was anticipated that the experimental tests would provide the maximum fluence that the mirror surfaces can withstand without reflectivity properties deterioration.

SS mirror
Size: 10 ×10 ×10 mm^3

Cubic Mo mirror
Size: 10 ×10 ×10 mm^3

Round Mo mirror
Diameter d = 25 mm
Thickness h = 4.7 mm

Figure 63: Photos of SS and Mo mirrors

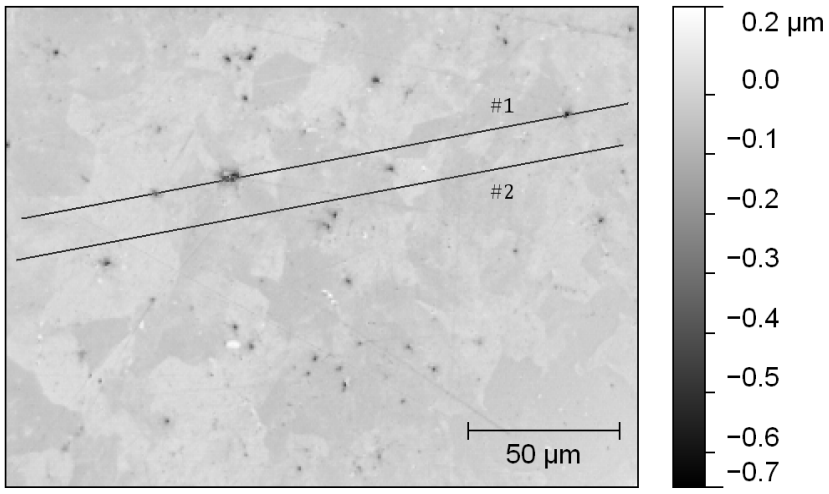

Figure 64: Height map of a 200×150 μm² zone of the round Mo mirror obtained with the optical profilometer MicroXAM 100. Colour indicates the height of surface at the specified point.

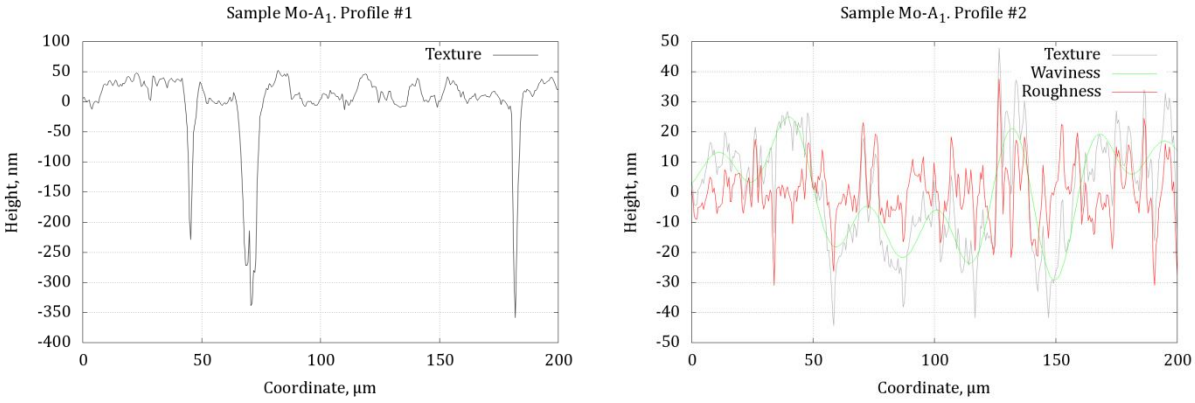

Figure 65: Surface profiles along the lines #1 and #2 on Figure 64

To inspect the surface quality of cubic mirrors, the attempts were made to use mechanical profilometer. But because of inaccurate tuning, the profilometer has made the traces on the certain zone of the surface, and thus its roughness was changed. For the zone with these traces, we obtained R_a = 0.0 5 8 μm for stainless steel mirror. But for the lines between two traces, R_a = 0.0 2 0 ± 0.0 0 1 μm (this value is the average roughness over 15 measurements on 150 μm length). The roughness of molybdenum mirror is R_a = 0.0 5 8 ± 0.0 1 9 μm. The traces from the mechanical profilometer for molybdenum mirror are smaller than for stainless steel, and they have not affected the roughness.

On Figure 64, the measured surface profiles of round Mo mirror are presented. The areal surface roughness S_a of this sample over 2×1.5 mm² zone measured by a fabricator is S_a = 4 – 4.5 nm. The areal surface roughness over 200×150 μm² zone indicated on Figure 64 is S_a = 18.5 nm. It is visible that there are defects on the sample surface (black points). The defects have a form of dips with the depth of 0.4 – 0.9 μm with typical lateral size of 1 – 2 μm.

The profile surface roughness measured on the profile #2, which does not pass through defect points, is R_a = 7.3 nm, while, the profile surface roughness measured on the profile #1 passing through defects is R_a = 31.6 nm (see Figure 65).

SEM image of a zone with surface defect is presented on Figure 66. The presence of defects may affect the damage thresholds of mirrors. The reflectivity of defects is generally lower than that of a smooth surface. Thus, at defects, the damage may occur at lower laser fluence.

Figure 66: SEM image of the zone with surface defects

4.3.2 Reflection coefficient

The total reflection coefficients of the mirrors were measured at 1064 nm and 543.5 nm using integrating sphere (see section 3.3.1). Additionally, the reflection of the back side of the mirror was measured at 1064 nm. The results are presented in Table 12.

Table 12: Full reflection coefficients measured for sample mirrors

	Full reflection coefficient
SS mirror, 1064 nm	0.67 ± 0.01
Cubic Mo mirror, 1064 nm	0.69 ± 0.01
Round Mo mirror, Mirror surface, 1064 nm	0.71 ± 0.04
Round Mo mirror, Mirror surface, 543.5 nm	0.57 ± 0.04
Round Mo mirror, Back side, 1064 nm	0.25 – 0.5 depending on the position

Three separate measurements of the spectral reflection coefficient for round Mo sample were made. The red filling on Figure 67 corresponds to 90% confidence interval of the spectral reflection coefficient for the mirror; the maximal absolute error is 0.008. The blue line indicates the reflection coefficient calculated from the handbook data on refraction index of molybdenum [93].

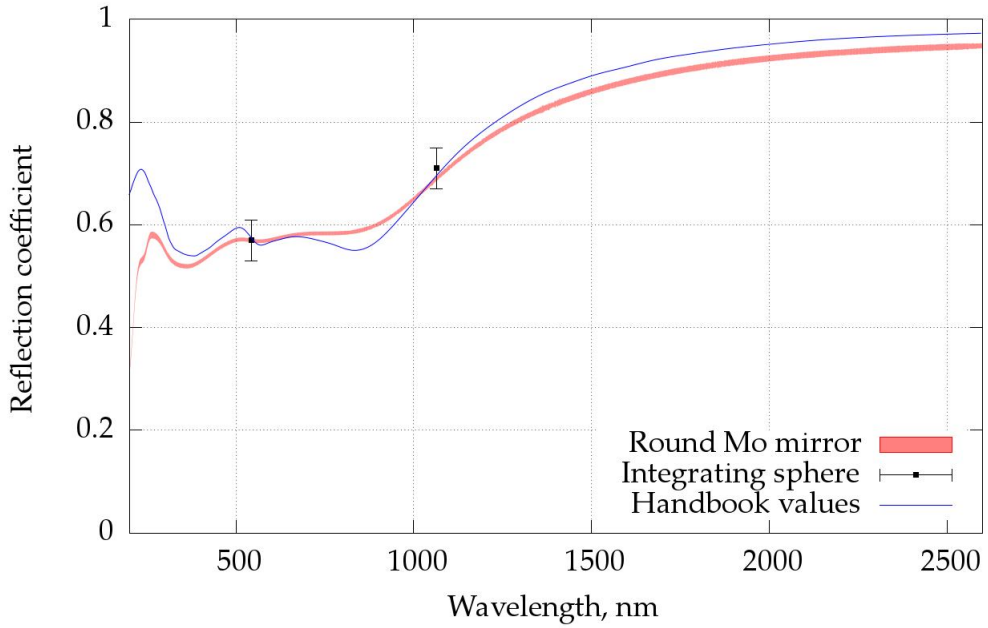

Figure 67: Spectral reflection coefficient of molybdenum. Total reflection coefficient measured with integrating sphere is indicated by points for 532 and 1064 nm.

4.3.3 Damage thresholds measurements

To measure the damage thresholds of cubic SS and Mo mirrors, the following scheme was used. The surface of each mirror was treated by laser by lines. Each line corresponds to different power of laser. Laser beam moves along the line with high speed to ensure that each pulse produces well-separated spots on the surface.

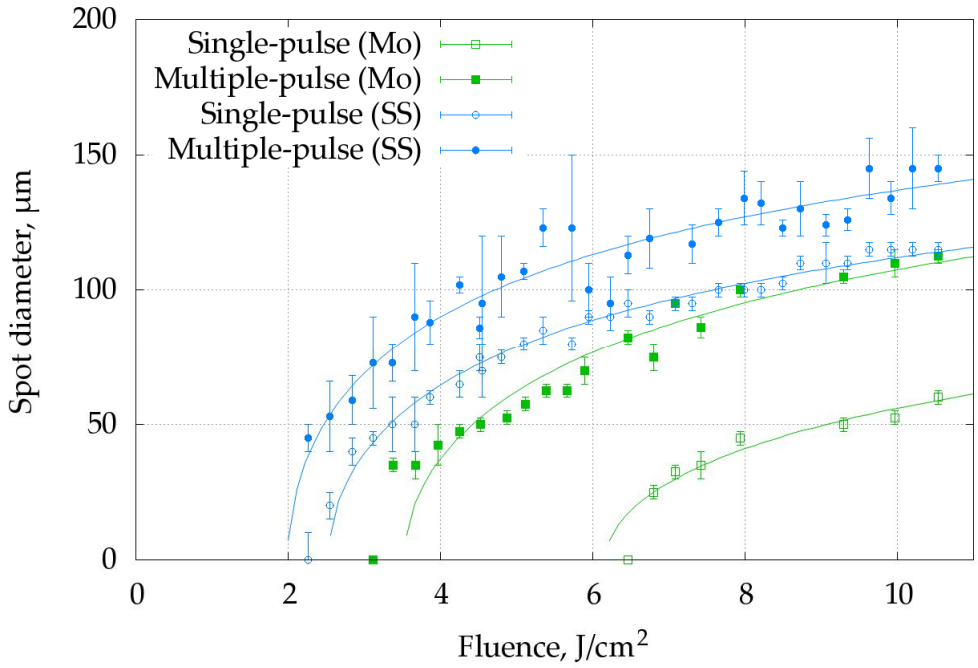

Figure 68: Spot diameter as a function of laser fluence for cubic SS and Mo mirrors

Then, by analyzing these spots with optical microscope, we could plot the spot diameters as a function of laser fluence (see Figure 68). One should note that stop points are the points where the scanning system stops laser beam scanning for about 0.1 to 0.3 second and the mirror receives about 5000 pulses in the same place. So, these spots are larger than single pulse spots.

Using the dependence of damage spot diameter on the laser fluence, the damage thresholds were determined with "burning paper" technique (section 3.4.1). They are presented in Table 13 together with theoretical thresholds calculated in section 2.2.

Table 13: Experimental and theoretical damage thresholds for cubic SS and Mo mirrors

	Molybdenum		**Stainless steel**	
	Theoretical	Experimental	Theoretical	Experimental
Single-pulse	6.67 J/cm²	6.2 ± 1.2 J/cm²	2.53 J/cm²	2.53 ± 0.14 J/cm²
Multiple-pulse	2.56 J/cm²	3.5 ± 0.4 J/cm²	0.7 J/cm²	2.0 ± 0.2 J/cm²

Unknown coefficient A_1 of temperature dependence of absorptance for stainless steel was determined on the basis of our experimental damage threshold. We found the value of coefficient A_1 that gives the maximal temperature on the surface equal to

melting temperature T_m under the action of pulse with fluence $F = E_{th}^{exp}$. For stainless steel, this gives $A_1 = -1.21 \cdot 10^{-4}$. The coefficient is negative (similar to suppositions of earlier investigations, see section 2.1.3).

Recalculating theoretical damage thresholds with help of the expressions (32) and (33) we obtain: $F_{th} = 2.53$ J/cm² for single-pulse threshold and $F_{th} = 0.7$ J/cm² for multi-pulse threshold.

To compare our experimental results with the damage thresholds for molybdenum and stainless steel available in literature, we will use the dependence of threshold fluence F_{th} on the laser pulse duration τ and sample absorptance A_0 that readily follows from (31) (see also [46], [94])

$$F_{th} \sim \sqrt{\tau}/A_0 \tag{124}$$

In [54], the damage threshold $F_{th} = 2.0 \pm 0.4$ J/cm² for polycrystalline molybdenum sample was determined for a Nd:YAG laser with the pulse duration of 12 ns. By using the threshold dependence on τ (124), the threshold value of [54] transforms to $F_{th} = 6.3 \pm 1.3$ J/cm² for pulse duration of 120 ns. This is in good accordance with our single-pulse threshold $F_{Mo} = 6.2 \pm 1.2$ J/cm²

The damage threshold of stainless steel AISI 304 was measured in [94] with CO_2 laser for two different pulse durations of 1.7 ns and 58 ns. By recalculating these results to pulse duration of 120 ns and absorptance of 0.33, we obtain $F_{th} = 2.1 \pm 0.2$ J/cm², which corresponds to our result $F_{SS} = 2.53 \pm 0.14$ J/cm² (see Table 12).

To investigate the influence of successive laser pulses overlapping on the damage threshold and on the surface oxidation, three series of experiments with different scanning speed were performed with round Mo mirror. Three scanning speeds were chosen to obtain different overlapping regimes:

- $v = 5000$ mm/s to obtain well-separated spots
- $v = 200$ mm/s to obtain medium overlapping between successive impacts (displacement between pulses is $\Delta x = 10$ μm)
- $v = 4.65$ mm/s to obtain high overlapping between successive impacts (displacement between pulses is $\Delta x = 0.23$ μm). This is the lowest possible speed.

After the treatment, damage spots and lines (for regimes with overlapping) were analyzed with optical microscope and profilometer. The diameters of damage spots and thicknesses of damage lines (for regimes with overlapping) were measured. They are presented as a function of laser fluence on Figure 69.

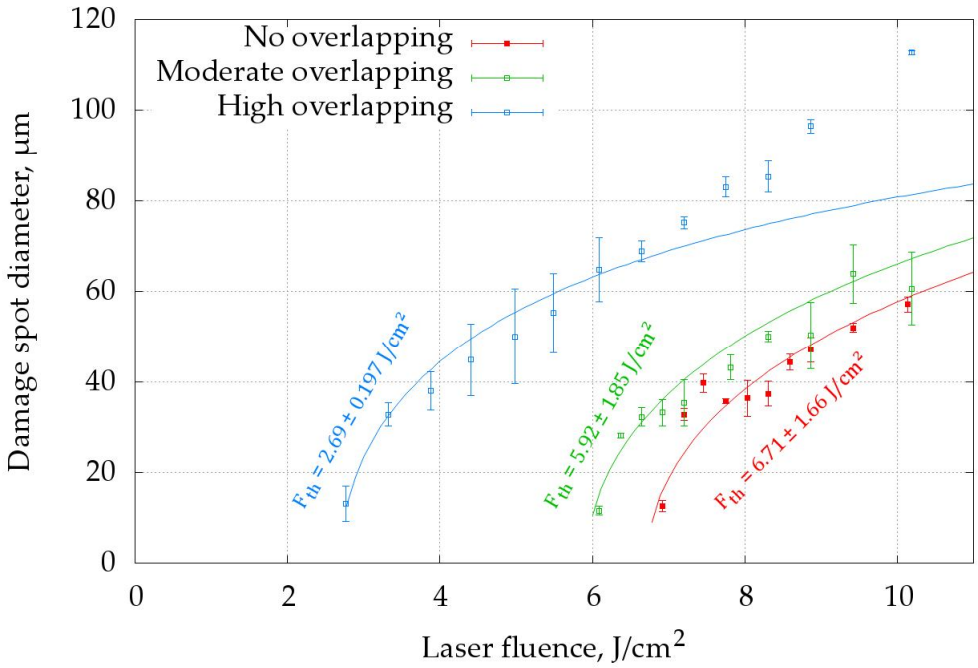

Figure 69: Dependence of the damage zone size on the laser power for different scanning rates. Lines show the theoretical curves obtained by fitting dependence (119) to the experimental points.

Using this dependence, the damage thresholds were determined with "burning paper" technique (section 3.4.1). For high overlapping, the damage lines made with $F > 7$ J/cm² were not taken into account during fitting, because their sizes increase due to surface oxidation (see section 4.3.5). The obtained damage thresholds are presented in **Table 14**.

Table 14: Damage thresholds for three regimes of laser pulses overlapping

	No overlapping	Medium overlapping	High overlapping
Damage threshold	12.1 ± 3.9 W 6.7 ± 1.7 J/cm²	10.7 ± 4.4 W 5.9 ± 1.9 J/cm²	4.9 ± 0.5 W 2.7 ± 0.2 J/cm²

4.3.4 Damage spots profiles

The multi-pulse damage spots formed on cubic mirrors during the damage thresholds determination were analysed with optical profilometer.

Profiles of laser impacts on the SS mirror (see Figure 70) correspond to typical craters formed during laser ablation of metal substrate. These craters are rather deep (9–10 μm in depth) and have a solidified expulsed crown (up to 9 μm in height) along the perimeter. With decrease in laser pulse fluence, the depth of craters

deacreses and after some value, the craters become just altered spots of melted matter.

The spots on the Mo mirror can hardly be referred to as "craters". The spots shown on Figure 71 look like “protuberance” of about 4 – 5 μm in height with a shallow ditch along the perimeter. The spot formed during interaction of one laser pulse with the surface has only shallow ripples.

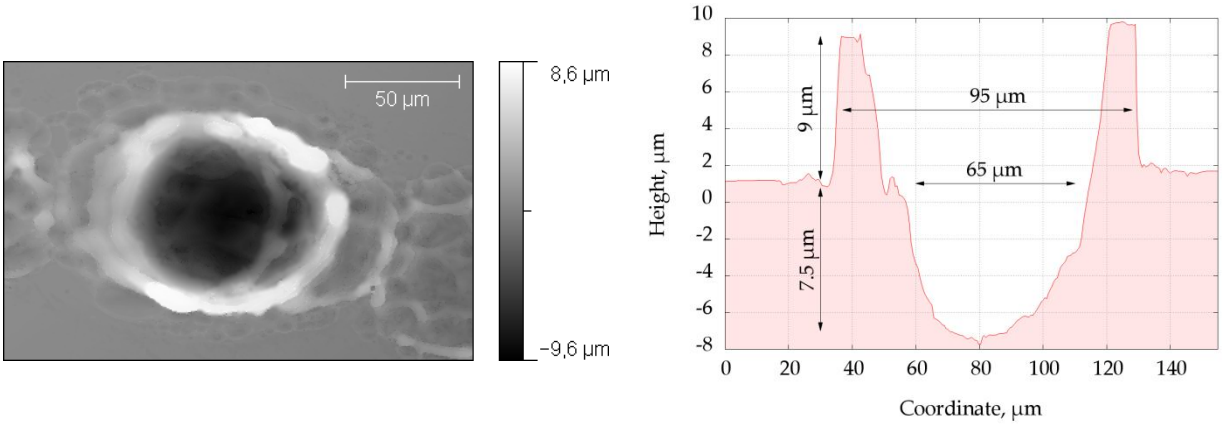

Figure 70: Profile of a crater on the surface of the SS mirror after application of ~5000 shots with E=0.93 mJ, F=10.54 J/cm²

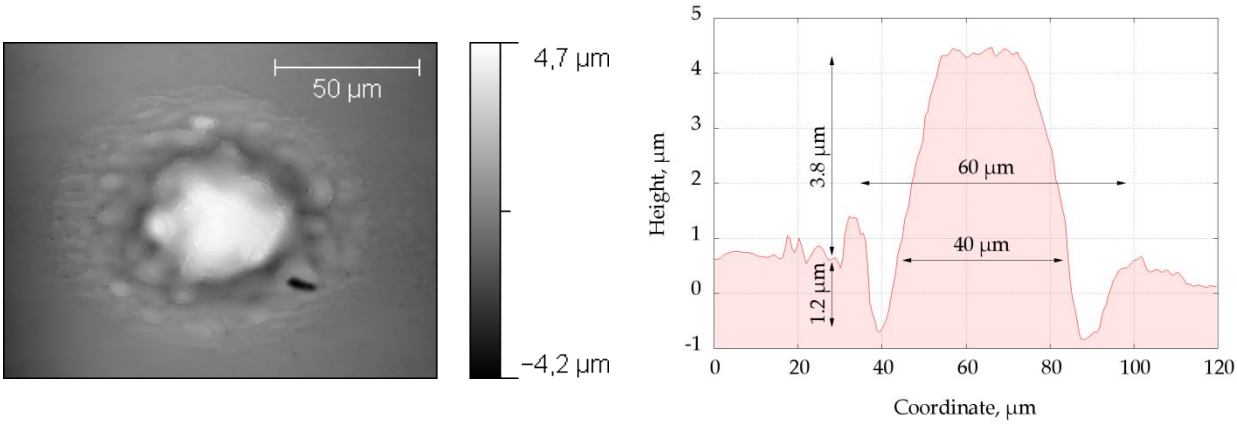

Figure 71: Profile of a crater on the surface of the Mo mirror after application of ~5000 shots with *E*=0.93 mJ, *F*=10.54 J/cm²

4.3.5 Presence of oxidation

We performed a series of measurements of laser impacts by Scanning Electron Microscope (SEM) JEOL JSM-7000F and determination of elemental composition on the surface of the mirrors by using energy dispersive X-ray spectrometer (EDS).

During these measurements, we were interested in whether there is additional oxidation of the surface inside the area of laser impact.

Figures 72 – 74 shows several views of cubic SS sample. The EDS spectra at the indicated points 1 – 4 are shown on Figure 75.

For the overall view on Figure 72, one can see that mirror is of a quite poor quality: there are black strokes with preferentially vertical direction on the surface of mirror. Elemental analysis indicates that these black strokes are the grains of MnS phase on the surface (see Figure 72 and Figure 75, point 3). One can see melted traces of MnS grains on the surface (point 4).

Moreover, one can see that spectra indicate that there is some amount of oxygen on the surface and, thus, there is some oxidation. But as it is very difficult to distinguish O line (0.532 keV) from Cr line (0.57 keV), one can hardly determine the amount of oxygen on the surface.

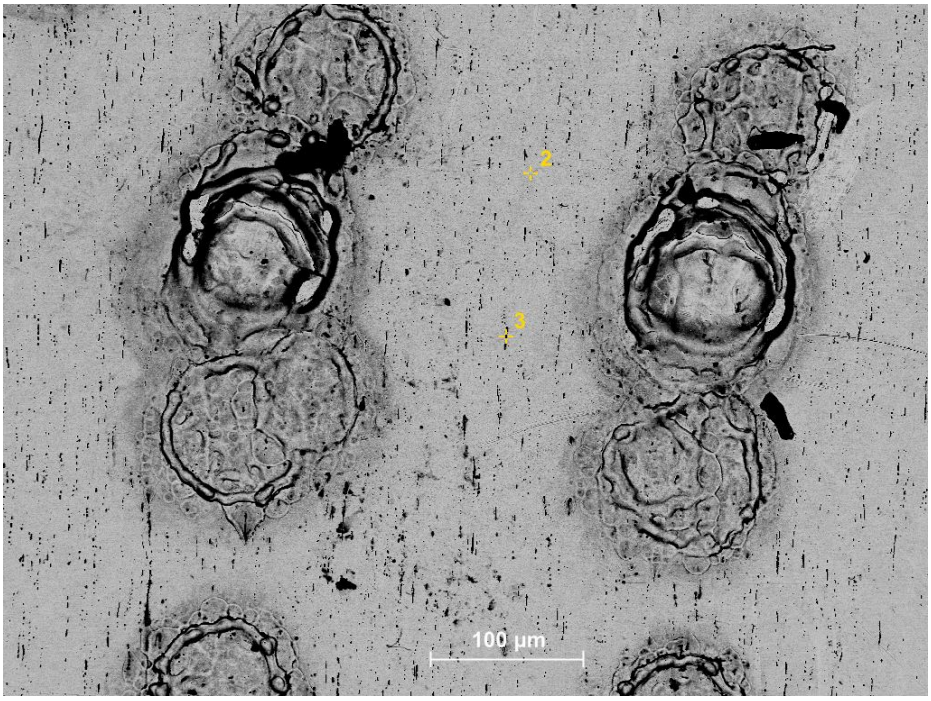

Figure 72: Overall view of impacts of the stainless steel mirror. Measured with SEM. Magnification: 200x.

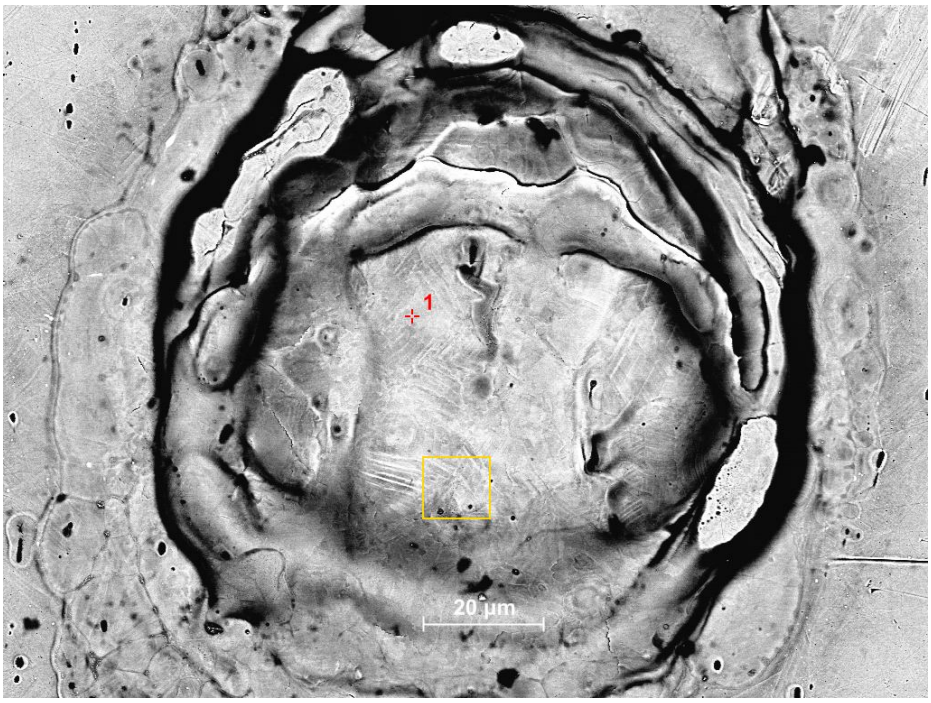

Figure 73: Crater A on the surface of the stainless steel mirror formed after around 5000 pulses of laser working in 18.6 W mode. Measured with SEM, Magnification: 800x. Marked region is shown on Figure 74.

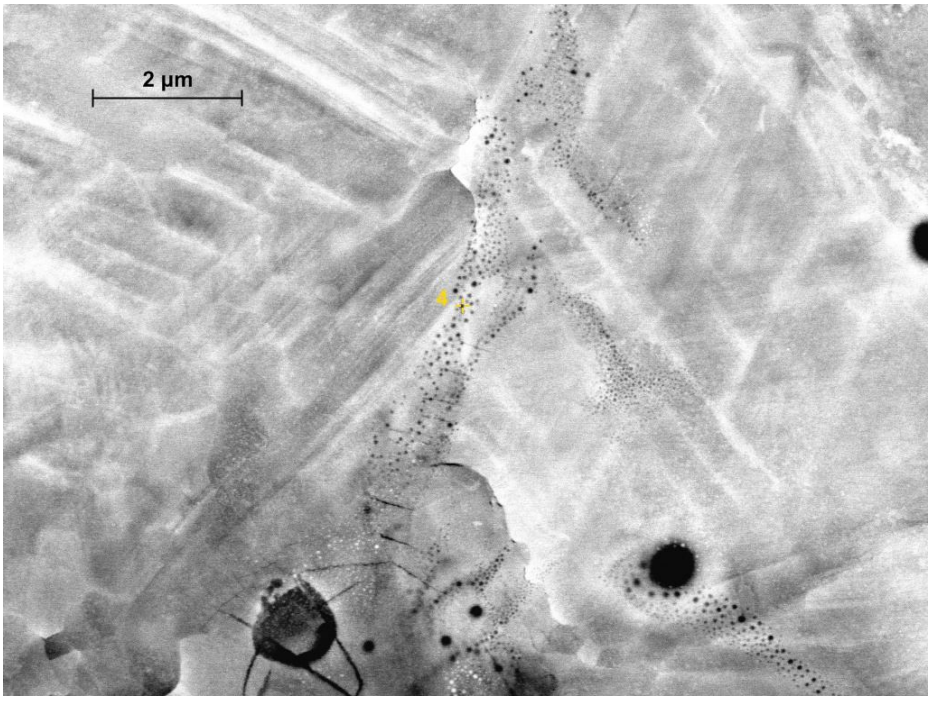

Figure 74: Stainless steel mirror. Close view of the inner part of the crater. Measured with SEM. Magnification: 10000x.

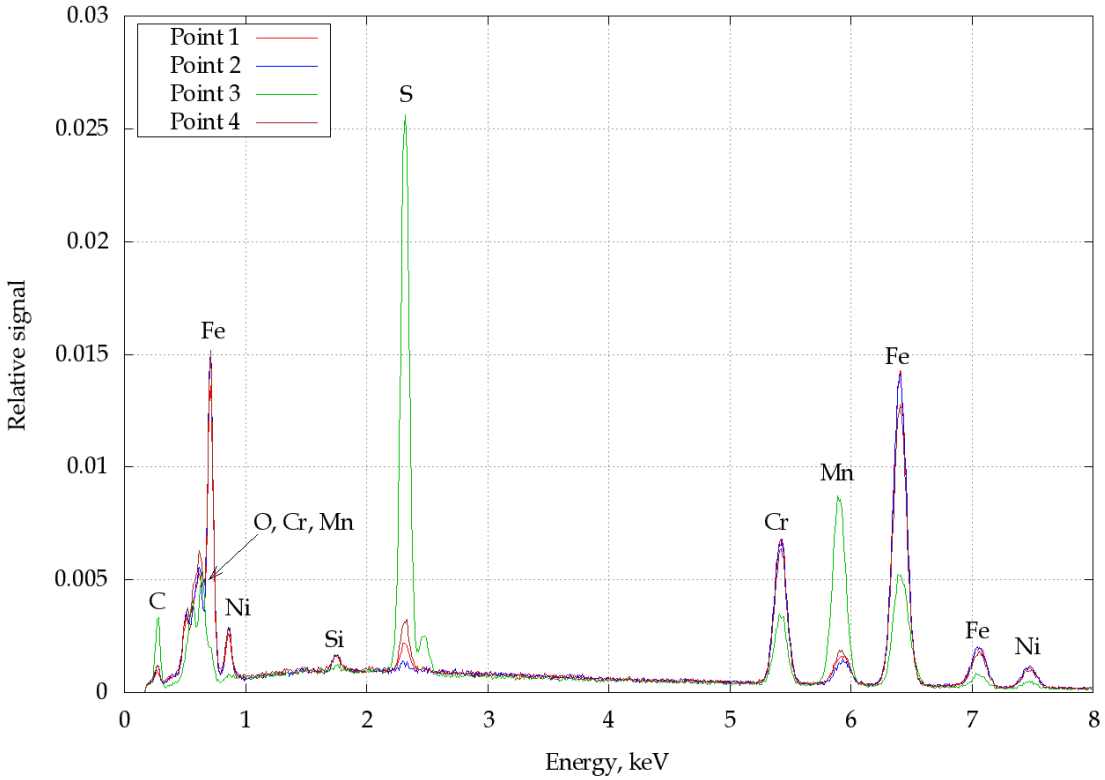

Figure 75: EDS spectra for stainless steel mirror at different points

The studies of Mo mirror oxidation were performed for three laser scanning speeds representing different overlapping between laser pulses in two ambient atmospheres: in air and in Ar. The spots and lines formed on the surface under the laser action were analyzed with SEM and EDS.

It was shown that no additional oxidation can be detected on the surface of Mo mirror after treatment with scanning speeds of v_x = 5000 mm/s (well-separated impacts) and v_x = 200 mm/s (moderate overlapping) in air atmosphere. However, for v_x = 4.65 mm/s scanning speed (high overlapping), damage lines become black and EDS analysis show presence of oxygen on the surface (see **Figure 76**).

The damage tests were repeated in argon atmosphere. For this, the sample was emplaced in a cylindrical cell filled with Ar. The end windows of the cell have dialectic coating of high transmittance at the laser wavelength λ = 1064 nm. The damage line formed due to laser treatment in Ar atmosphere and its EDS spectrum are shown on **Figure 77**. One can see the complete absence of oxidation is this case.

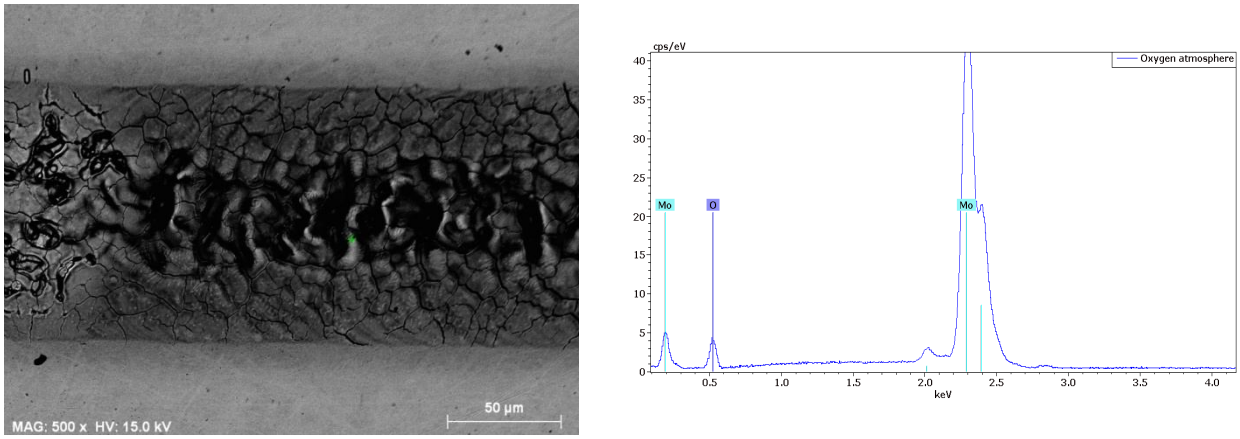

Figure 76: SEM image and EDS spectrum of the line formed on round Mo mirror under the action of laser beam. Scanning speed v = 4.65 mm/s, air.

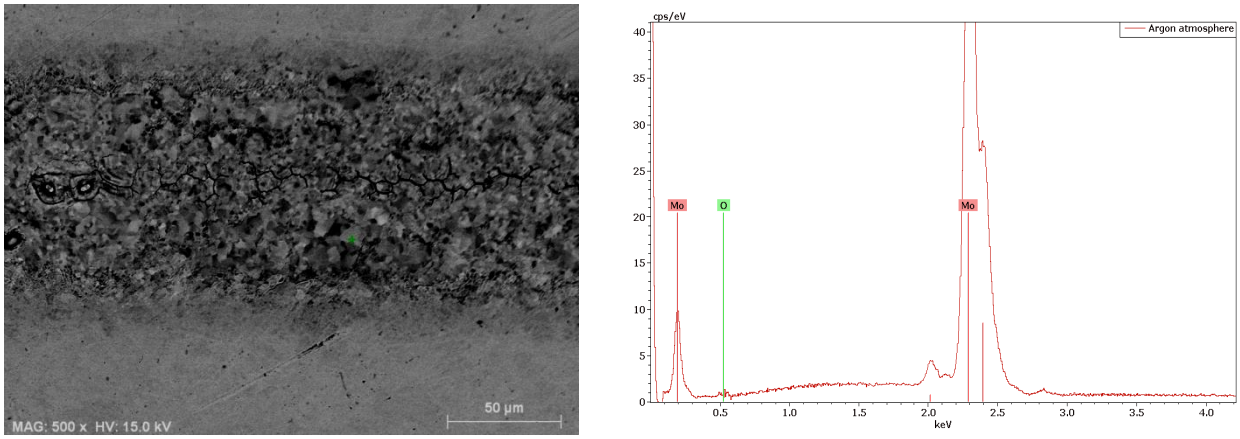

Figure 77: SEM image and EDS spectrum of the line formed on round Mo mirror under the action of laser beam. Scanning speed v = 4.65 mm/s, argon atmosphere.

4.3.6 Laser cleaning test

The carbon layer was deposited on the glossy surface of round Mo mirror using a carbon evaporator (Quorum Technologies Q150R ES). A special screen was placed on a part of mirror to obtain a zone without carbon layer. The average thickness of coating d = 31 ± 1 nm was determined with mechanical profilometer by analyzing the boundary of this zone (see Figure 78). One can see that the coating color is different for different zones of the mirrors surface. This means that the thickness also varies over the sample surface.

The total reflection coefficient of the mirror with carbon layer was found to be R_p = 0.29 ± 0.02 at 1064 nm.

Different cleaning regimes were tested to determine an optimal regime with the best ablation rate, but without mirror damage. In these tests, laser fluence was chosen to be below the damage threshold for mirror surface $F < 7.4$ J/cm². Due to difference in reflection coefficient, the damage threshold for polluted surface is lower than for a virgin one and equals to $F_{th}^{(p)} = \frac{F_{th}^{(0)} R_p}{R_0}$.

The tests reveal formation of defects on the cleaned surface of several micrometers in diameter. It may be associated with polycrystalline nature of the sample. The number of defects increases with laser fluence and with overlapping between laser spots. As a result, an optimal cleaning regime was determined: fluence $F = 7$ J/cm², scanning step $\Delta x = \Delta y = 50$ μm. This regime was applied for mirror cleaning.

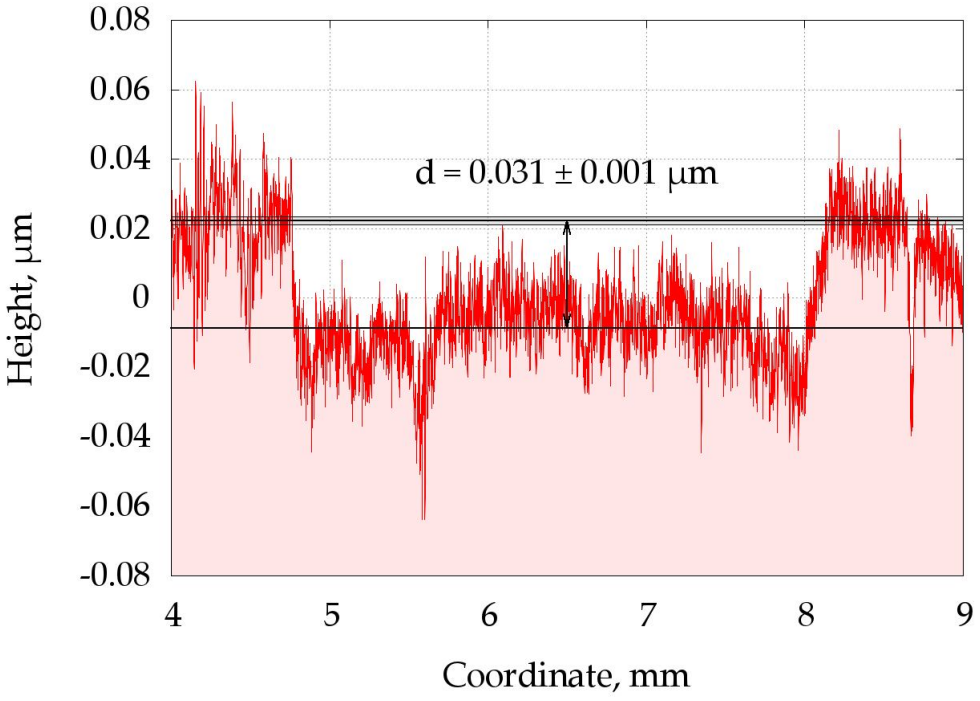

Figure 78: Surface profile of round Mo mirror with a carbon layer. Zone screened from layer deposition.

Figure 79 shows the results of specular spectral reflection coefficient measurements carried out before and after carbon deposition and after laser cleaning. Two green lines indicate two measurements of the mirror with a carbon layer performed in different zones.

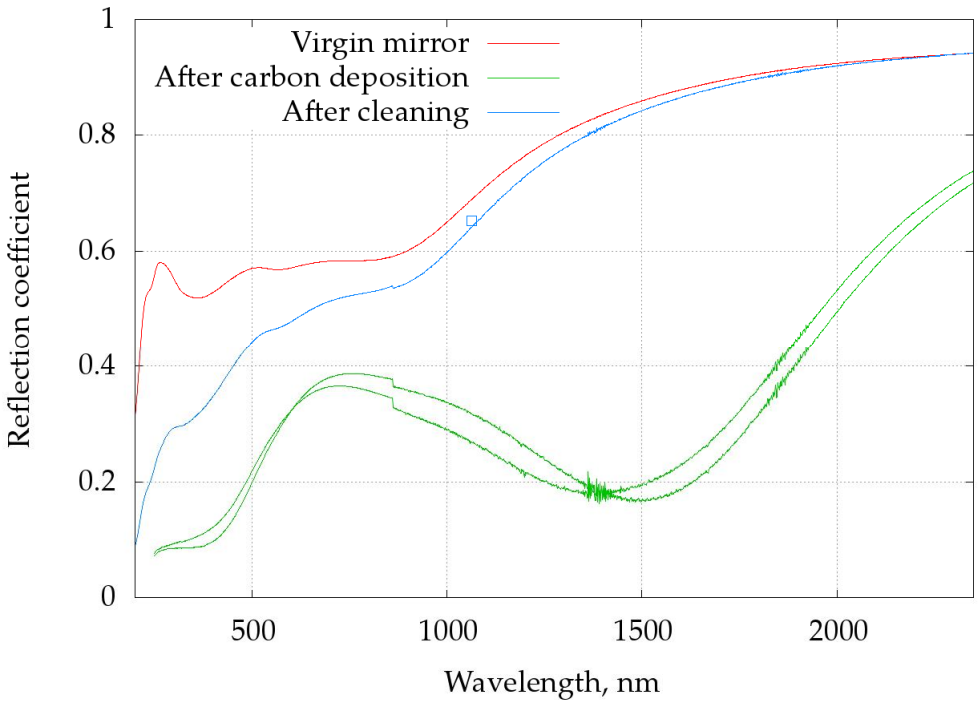

Figure 79: Spectral reflection coefficient of Mo mirror: before carbon deposition (red curve), after carbon deposition (green curves) and after laser cleaning (blue curve). The point indicates the value measured with integration sphere.

The reflectivity of the mirror is restored to more than 90% of its initial value for wavelengths $\lambda > 800$ nm. In the visible spectrum, the restitution is in the range of 60 – 80%.

4.3.7 Conclusions

Single-pulse and multiple-pulses damage thresholds of molybdenum and stainless steel mirrors were determined experimentally. Single-pulse experimental damage thresholds are in good accordance with those available in literature.

The results of experiment were compared with theoretical predictions. It was found that model with changing absorptance gives the correct thresholds for molybdenum. The coefficient of temperature dependence of absorptance for stainless steel (not available in literature) was determined by fitting theoretical single pulse threshold to experimental one.

As it was expected, pulsed laser treatment of stainless steel mirror with maximal laser power (1 mJ, ~11 J/cm^2) results in laser ablation of the sample with formation of characteristic craters.

In contrast, under the action of multiple laser pulses on the surface of molybdenum mirror the structures with the shape of hills are formed. EDS analysis

of the surface didn't reveal any traces of oxidation on these “hills”. Hence, we suppose that these "hills" were formed as a result of thermal stresses accumulation.

The oxidation of the Mo mirror surface was observed in air. Emplacement of the mirror in neutral atmosphere (Ar, He, …) prevents the surface from being oxidized.

Laser cleaning tests performed on the Mo mirror artificially contaminated with carbon show the possibility to clean up the mirror surface with 90% ($\lambda > 800$ nm) and 60 – 80% (visible range) restoration of initial specular reflection coefficient.

Chapter 5. General conclusions

Contents

Metal surface cleaning and decontamination are very important for nuclear and thermonuclear applications. Laser ablation for surface cleaning is a non-contact method which may offer certain advantages for some particular applications in nuclear industry.

Our studies on "Laser decontamination and cleaning of metal surfaces: modelling and experimental studies" were aimed to make particular study on the interaction of coherent laser radiation with very thin (micrometric or sub-micrometric) layers on a solid state (metal) substrate. Experimental and theoretical results were compared to improve and validate the developed models.

The aims of our study were defined as follows:

1. modelling of laser heating of a metal surface with a deposited layer;
2. development and application of experimental equipment for studies on high repetition rate laser surface heating and cleaning by laser ablation;
3. ablation threshold determination for different metal surfaces (oxide layer on stainless steel, ITER-like samples, Mo-mirror);
4. experimental studies on laser ablation efficiency (decontamination factor, ablation rate, metal substrate damaging) for cleaning metal surfaces with a contaminated layer;
5. Tokamak diagnostics mirrors cleaning to recover their initial reflectivity.

Below are the summarised results of our investigations.

5.1 Theoretical results

Our theoretical results may be presented as follows. Theoretical model for determination of the damage threshold of a pure metal substrate was developed and applied. It was supposed that damage occurs at the fluence when the maximal temperature due to laser heating reaches the melting point. The calculations have demonstrated that multi-pulse heat accumulation was not significant and could be neglected. In contrast, the effect of reflectivity change as a function of the surface temperature was significant during laser-substrate interaction. To determine the multiple-pulse damage threshold, the phenomenological theory explained by plastic deformations accumulation was applied. Using the model, damage thresholds for stainless steel, molybdenum, and tungsten were calculated.

Further improvement of the model of laser heating for metal surfaces with a layer was made. As deposited layers of thermonuclear devices and oxide layers formed in nuclear installations are inhomogeneous, laser beam interference and scattering in the layer should be considered. To calculate laser heating temperatures

for complex surfaces with semi-transparent inhomogeneous layers, a theoretical model for light propagation in the layer was proposed, developed and applied. The model is based on four-flux light transfer and takes into account interference, absorption and scattering of the coherent laser light in the layer. The computer code was written, tested and validated by comparing its results with those obtained with the models developed earlier in CEA Saclay, which describe the limiting cases of coherent and 3-flux approximations.

Thus, with this developed model, it becomes possible to calculate the distribution of heat sources and temperatures in-depth of the layer.

5.2 Experimental results

Our experimental results may be presented as follows. Laser ablation as a method for cleaning and nuclear decontamination and also some problems associated with it were under experimental study with different metal samples (stainless steel, ITER-like, Mo-mirrors).

5.2.1 Experimental equipment

Laser ablation was performed with a high repetition rate ytterbium fiber laser (120 ns pulse duration, 20 kHz repetition rate, 1.06 μm wavelength, 1 mJ pulse energy, focused to 100 μm laser spot diameter).

The single-pulse damage thresholds were determined by a "burning paper" technique. The crater profiles and ablation depth during laser cleaning were analysed with mechanical and optical profilometers.

The heating measurements were performed with a 10 ms ytterbium fiber laser and a fast pyrometer (10 μs response time, 1.58 – 2.20 μm spectral sensitivity range). The pyrometer applied for laser heating temperature measurements was calibrated with a black body radiation source. To determine the unknown emissivity of a sample, the appropriate data treatment was applied.

The efficiency and features of laser ablation and cleaning were analysed by measuring surface profiles before and after laser treatment. Two profilometers, an optical one (Phase Shift Technology MicroXAM 100) and a mechanical one (Mahr), were applied. For laser cleaning, the ablated depth was determined as a difference in surface height of the treated area and the untreated one.

To analyse the depth of the formed oxide layer and its elemental in-depth composition, a Glow-Discharge Optical Emission Spectrometer was applied.

5.2.2 Oxidized metal surfaces

Decontamination by laser ablation of oxidized metal surfaces (stainless steel AISI 304L samples) was under study. For these experiments, the oxidation of stainless steel by laser heating with a scanning regime with high overlapping and also in a furnace at 1273 K in air was applied.

Radioactive contamination of the oxide layer was simulated by introducing europium (Eu) and sodium (Na). The decontamination factor (the ratio of the concentrations of contaminant before and after cleaning) of 300 for Eu-contaminated sample was obtained after deposition of 372 J/cm^2. For Na-contaminated sample, the decontamination factor was 1500 after deposition of 186 J/cm^2. Such decontamination factors are considered as sufficient to clean radioactive wastes.

Laser cleaning rate of 0.001 m^2/W×hour was demonstrated.

However, after laser cleaning, the corrosion resistance of stainless steel surface was defined as being significantly degraded. This may be associated with the fact that several micrometers in-depth of the metal surface had become chromium-depleted due to oxidation and laser cleaning.

5.2.3 ITER-like samples

Laser ablation was applied for ITER-like samples (stainless steel or W-substrate with deposited layers of W or diamond-like carbon with hydrogen and deuterium content). Laser cleaning efficiency, plastic deformation and ablation thresholds, fluences and laser heating rates have been determined experimentally. Laser cleaning productivity of 0.07 m^2/W×hour was demonstrated.

At low fluences, the layer with carbon demonstrated mechanical deformations because of thermo-mechanical stresses induced in the layer as a result of its rapid laser heating. At higher fluences, the layer began to ablate. This effect can be used to remove deposited layer without its destruction (evaporation).

For tungsten substrate, it was found that the deposited layer, which contained a significant part of carbon, can be removed by laser ablation without substrate damage because of a great difference in ablation thresholds for the layer and the substrate. However, if the layer was without carbon, but rather with a metal (tungsten, aluminium) with low hydrogen/deuterium content, its ablation threshold increased significantly due to a higher reflectivity of the layer. For such layers (especially made of tungsten), laser ablation resulted in substrate damage. For these cases, detritiation by laser heating may be advised.

5.2.4 Mirrors

In our study on mirror cleaning, restoration of reflection coefficient and damage thresholds for several types of mirrors (molybdenum and stainless steel) have been determined.

The reflectivity of metal mirrors was controlled by a spectrometer. A special accessory to allow measurements of reflection coefficient was used. The spectra obtained with the spectrometer provided data on reflection coefficient restoration in 250-2500 μm wavelength. Along with the spectrometer, which measured only the specular reflection coefficient, a set-up based on integrating sphere was applied to measure the total reflection coefficient of a surface at 543.5 nm and 1064 nm wavelengths.

Cleaning tests were performed with polycrystalline molybdenum mirrors artificially contaminated with a graphite layer. Laser fluence was chosen to be below the damage threshold for mirror surface. The mirror reflectivity was restored to more than 90% of its initial value for wavelengths $\lambda > 800$ nm. In the visible spectrum, the restitution was 60 – 80%.

However, a substrate damage took place in a form of small defects (several micrometers in diameter) which might be attributed to the polycrystalline nature of the sample. Thus, to avoid irreversible damage of the mirror surface, appropriate laser parameters should be chosen for laser cleaning of metal mirrors.

In addition, high overlapping of successive laser pulses has resulted in a long-lasting heating of the same zone, which in its turn resulted in mirror surface oxidation, if the treatment was made in air. With the treatment in neutral atmosphere (Ar, He, …), it is possible to avoid mirror oxidation.

The results of our experimental and theoretical studies on Tokamak diagnostics mirror cleaning have demonstrated that single-pulse and multiple-pulse damage thresholds may be predicted quite accurately if reflectivity changes with temperature and plastic deformation accumulation are taken into account in the model.

Thus, theoretical and experimental studies on laser cleaning of metal surfaces have demonstrated the possibility to clean mirror surfaces without their damage.

5.3 Further studies and perspectives

To complete the results of our study, the scope of possible future investigations may be seen as follows:

- Laser cleaning tests on a monocrystalline molybdenum mirror should be made to elucidate the nature of defects which appear on the mirror after laser cleaning.
- For further improvement of the model of light propagation in an inhomogeneous layer, roughness of boundaries should be taken into account. If the source cannot be regarded as monochromatic, then integration over all wavelengths should be made.
- The effect of decontamination on corrosion resistance is very important for stainless steel substrates. If one knows certain laser cleaning features which would provide corrosion resistance without undesirable deterioration affects, laser cleaning might offer additional advantage for its application. Moreover, the experiments with real oxidized samples are required to study the possibility to avoid undesirable surface changes resulting from the artificial oxidation, which may be too much significant.

5.4 Publications and presentations

Scientifique journals

- A. Widdowson, J.P. Coad, G. de Temmerman, D. Farcage, D. Hole, D. Ivanova, **A. Leontyev**, M. Roedig, M. Rubel, A. Semerok, P.-Y. Thro and JET-EFDA Contributors. Removal of beryllium-containing films deposited in JET from mirror surfaces by laser cleaning. *Journal of Nuclear Materials*. **In press.** doi:10.1016/j.jnucmat.2010.11.076
- **A. Leontyev**, A. Semerok, D. Farcage, P.-Y. Thro, Ch. Grisolia, A. Widdowson, P. Coad, M. Rubel and JET-EFDA contributors. Theoretical and experimental studies on molybdenum and stainless steel mirrors cleaning by high repetition rate laser beam. *Fusion Engineering and Design*. **86** (2011) 1728–1731**.** doi:10.1016/j.fusengdes.2010.12.068

CEA reports

- **A. Leontyev**, A. Semerok, P.-Y. Thro, D. Farcage, C. Blanc, A. Cheniere. Laser Cleaning of JET Diagnostic Mirrors in Beryllium Handling Facility (JET Task: Fusion Technology JW9-FT-3.54). CEA Saclay, 2010, NT DPC/SCP 10-340-A.
- P. A. Kizub, **A. V. Leontyev**. Choice of non-dangerous materials for ITER-like samples. CEA Saclay, 2010, NT DPC/SCP 10-356-A.
- **A. Leontyev**, A. Semerok, P.-Y. Thro, P. Dewalle. Laser ablation test with the ITER-like wall materials, W and CFC (EFDA-JET Task: Fusion Technology JW9-FT-3.53). CEA Saclay, 2010, NT DPC/SCP 10-388-A.
- A. Semerok, **A. Leontyev**, P.-Y. Thro. Laser ablation test with the ITER-like wall materials. (EFDA-JET Task: Fusion Technology JW10-FT-3.56). CEA Saclay, 2011, NT DPC / SCP 11-404 indice A.

Oral presentations

- **A. Leontyev**. Laser decontamination of metal surfaces. *CEA/ROSATOM meeting*, CEA Saclay, 29/06/2009.
- **A. Leontyev**, A. Semerok, P.-Y. Thro. Laser decontamination of metal surfaces. *Seminar in laboratory LAPD at CEA Marcoule*, 25/11/2009.
- **A. Leontyev**, A. Semerok, P.-Y. Thro. Laser ablation for metal surface cleaning. *PhD session of doctoral school « Ondes et Matière »*, University Paris 11, 08/03/2010.
- **A. Leontyev**, D. Melyukov, A. Semerok, P.-Y. Thro. Laser ablation tests with the ITER-like wall materials, W and CFC. *EFDA-JET monitoring meeting*, 07/06/2010.
- A. Semerok, P.-Y. Thro, F. Champonnois, D. Farcage, **A. Leontyev**, C. Grisolia. Laser decontamination and cleaning methods for modern nuclear technologies. *Fundamentals of Laser Assisted Micro- & Nanotechnologies*, St. Petersburg-Pushkin, Russia, July 2010.

Poster presentations

- **A. Leontyev**. Laser decontamination of metallic surfaces. Poster on the *10th Scientific session of DANS*, CEA Saclay, 10/06/2010.
- **A. Leontyev**, A. Semerok, D. Farcage, P.-Y. Thro, C. Grisolia, A. Widdowson, P. Coad, M. Rubel and JET-EFDA contributors. Theoretical and experimental studies on molybdenum and stainless steel mirrors cleaning by high repetition rate laser beam. Poster on the *26th Symposium on Fusion Technology*, Porto, Portugal, September – October 2010.
- **A. Leontyev**, A. Semerok, and P.-Y. Thro. Studies on laser heating and laser ablation of ITER-like surfaces. Poster on the *13th International Workshop on Plasma-Facing Materials and Components for Fusion Applications*, Rosenheim, Germany, May 2011.

Appendixes

Appendix A. Material properties

Molybdenum properties

The principal properties of bulk molybdenum obtained from [91], [95–97] are presented in Table 15.

Table 15: Principal thermophysical and optical parameters of molybdenum

	Notation	Value
Density	ρ	10220 kg/m^3
Specific heat	c	250 J/kg·K
Thermal conductivity	k	138 W/m·K (at 300 K)
Melting temperature	T_m	2890 K
Melting heat	ΔH_{fu}	36 kJ/mol = 375 kJ/kg
Thermal diffusivity	$\kappa = k/\rho$	5.4·10^{-5} m^2/s
Reflectivity	R	0.69 (for λ = 1064 nm at room temperature)
Absorption coefficient	α	55 μm^{-1} (for λ = 1064 nm)

The coefficient of temperature dependence of the absorptance A_1 is obtained from data on temperature dependence of the spectral emissivity [47–49], [91], [98]. The values obtained from different sources can be very different and can even have different signs, but in the majority of cases A_1 is negative. We have chosen the mean value $A_1 = -3.9 \cdot 10^{-5}$ calculated from [47].

Table 16: on the temperature dependence of molybdenum absorptance at 1064 nm

T_{mi}, K	A_{mi}	T_{ma}, K	A_{ma}	A_1	Reference
1500	0.325	2400	0.29	-3.9·10^{-5}	[47]
1298	0.475	1900	0.2	-4.58·10^{-4}	[49]
1000	0.302	2000	0.317	1.5·10^{-5}	[91]

The exponent s of the accumulation in the multi-pulse damage model was found to be $s = 0.88 \pm 0.01$ [53], [54].

Stainless steel 316L properties

In our calculations the following thermophysical parameters of stainless steel AISI 316L were used [91], [99].

Table 17: Principal thermophysical and optical parameters of stainless steel AISI 316L

	Notation	Value
Density	ρ	7990 kg/m^3
Specific heat	c	500 J/kg·K
Thermal conductivity	k	16.4 W/m·K (at 373.15 K) 21.4 W/m·K (at 773.15 K)
Melting temperature	T_m	1658 K
Melting heat	$\Delta H_{f\ u}$	10 kJ/mol
Thermal diffusivity	$\kappa = k/\rho$	$5.36 \cdot 10^{-6}$ m^2/s
Reflectivity	R	0.67 (for λ = 1064 nm)
Absorption coefficient	α	36 μm^{-1} (for λ = 1064 nm)

In our calculations we will use thermal conductivity value k = 21.4 W/m·K as it represents the mean thermal conductivity over the temperature range from room temperature to the melting temperature.

There is no data about exponent of accumulation curve for stainless steel 316L in the literature. But we can estimate it as s = 0.8497 on the basis of classical mechanical-fatigue data which is summarized in Table 18 (for details see [53]).

Table 18: Mechanical fatigue data for stainless steel 316L

Measured exponent	Exponent s	Reference
c = −0.4207	0.88414	[100]
b = −0.212	0.788	[101]
c = −0.38479	0.87696	[102]
Average:	**0.8497**	

Tungten properties

In Table 19, main properties of tungsten, which was used in calculations, are presented. All values in this table correspond to the standard condition for temperature and pressure if opposite isn't stated explicitly. To calculate the average

thermal conductivity up to the melting point, the data from [92] is used (see Figure 81).

The spectral reflection coefficient and spectral absorption coefficient are presented on Figure 80. The temperature dependence of light absorption at 1.064 μm is approximated by linear law: $A(T) = A_0 + A_1 T$, where $A_0 = 1 - R \approx 0.4$ and A_1 can be estimated as $-1.85 \cdot 10^{-5}$ from data on the temperature dependence of spectral emissivity [91].

Table 19: Main properties of tungsten

Property	Symbol	Value
Density	ρ	19350 kg/m^3
Molar mass	μ	183.85 g/mol
Specific heat capacity	c	132 J/kg·K
Thermal conductivity at 273 K	k	174 W/m·K
Average thermal conductivity up to the melting point	k	156 W/m·K
Thermal diffusivity at 273 K	κ	$6.8 \cdot 10^{-5}$ m^2/s
Melting temperature	T_m	3693 K
Reflection coefficient at 1.064 μm	R	0.602
Absorption coefficient at 1.064 μm	α	44 μm^{-1}
Coefficient of temperature dependence of the absorptance	A_1	$-1.85 \cdot 10^{-5}$

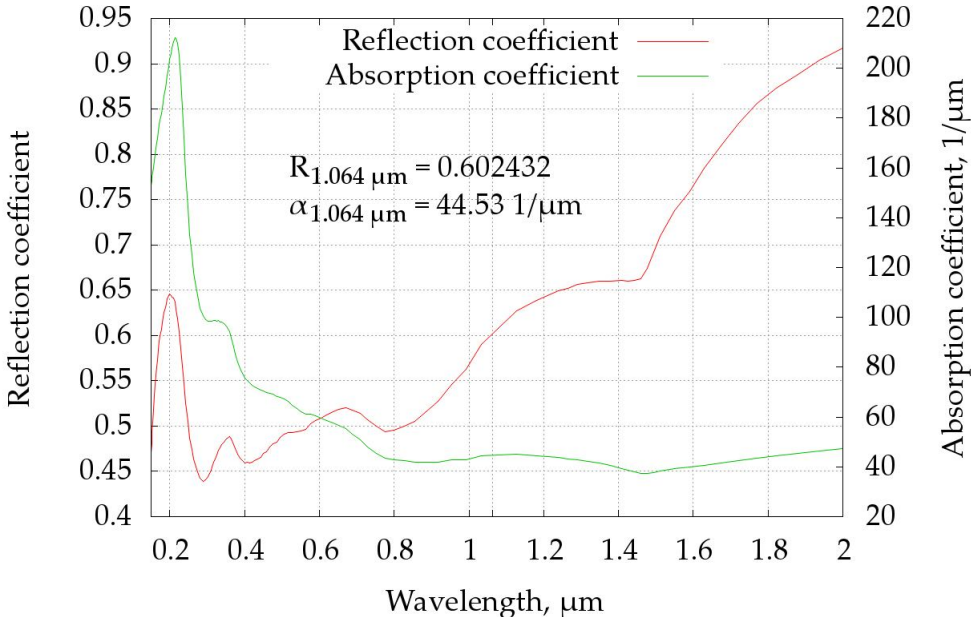

Figure 80: Optical properties of tungsten.

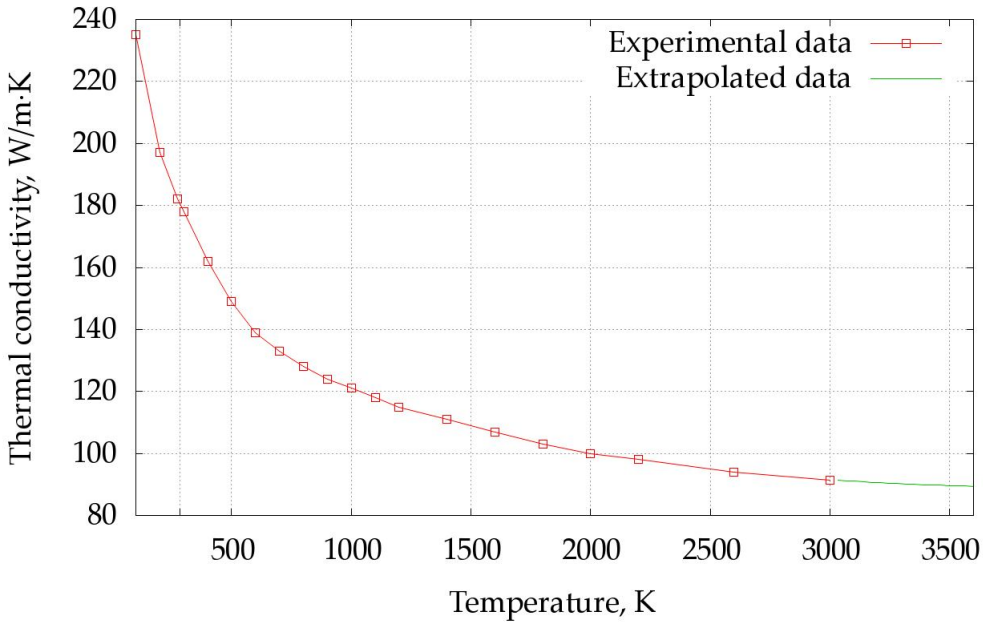

Figure 81: Temperature dependence of the thermal conductivity of tungsten.

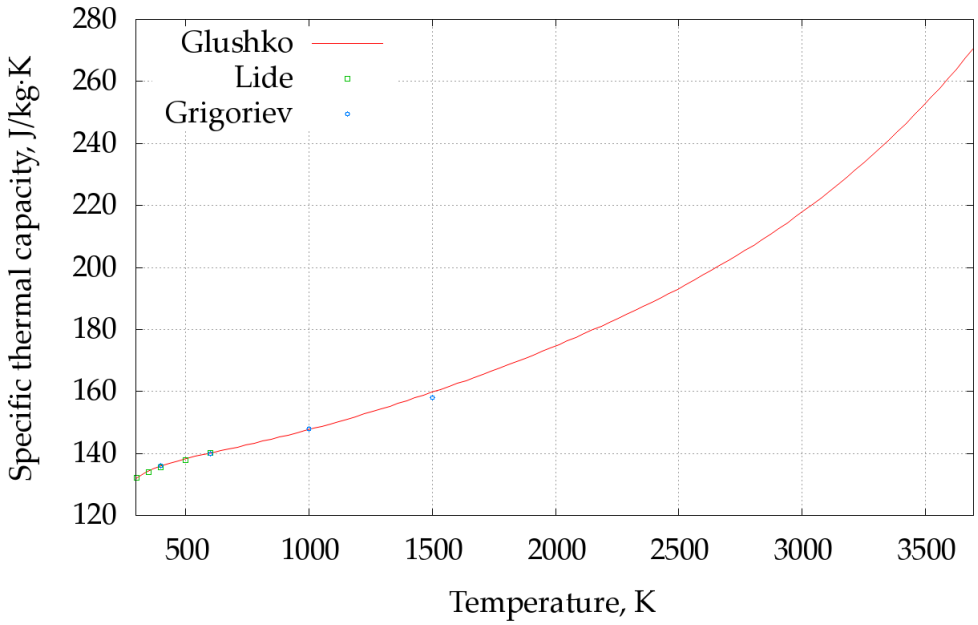

Figure 82: Temperature dependence of the specific heat capacity of tungsten. Sources: [91], [92], [103].

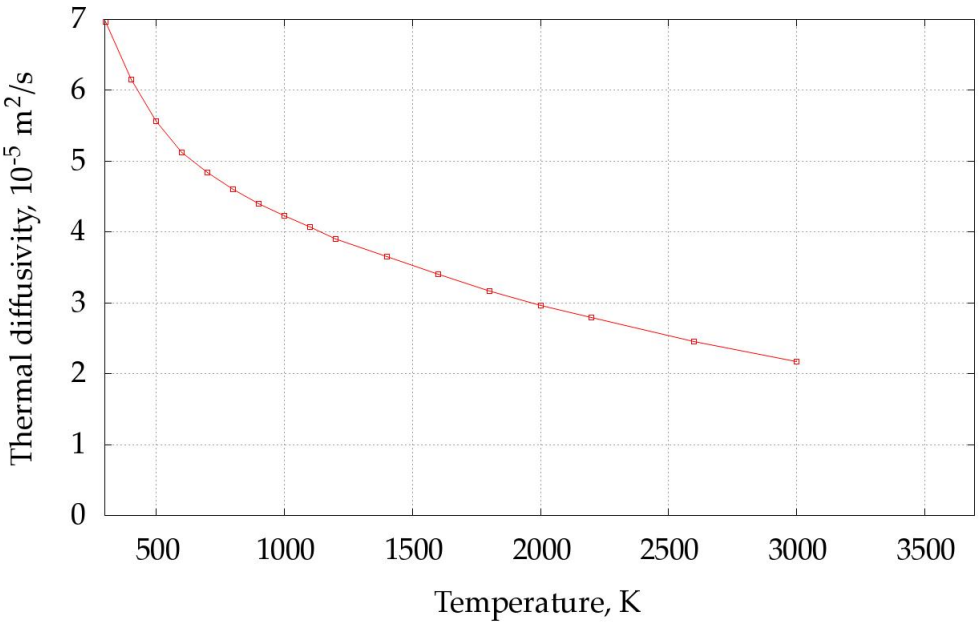

Figure 83: Temperature dependence of the thermal diffusivity of tungsten.

Appendix B. Derivation of boundary problem eigenfunctions

The general solution of the equation (44) can be readily derived as

$$\begin{cases} X_\lambda(\chi) = a(\lambda)\cos(\lambda\chi) + b(\lambda)\sin(\lambda\chi) & \text{for } \chi < \chi_d \\ X_\lambda(\chi) = c(\lambda)\cos(\lambda\chi) + d(\lambda)\sin(\lambda\chi) & \text{for } \chi > \chi_d \end{cases} \tag{125}$$

From the condition (45) it follows that $b(\lambda) = 0$. From conditions (46) and (47) following relations between coefficients can be established

$$\begin{aligned} c(\lambda) &= a(\lambda)\left(\beta \cos^2 \lambda\chi_d + \alpha \sin^2 \lambda\chi_d\right) \\ d(\lambda) &= a(\lambda)(\beta - \alpha)\cos\lambda\chi_d \sin\lambda\chi_d \end{aligned} \tag{126}$$

To find $a(\lambda)$ it is necessary to use orthogonality condition (48)

$$I = \int_0^\infty w(\chi)X_\lambda(\chi)X_{\lambda'}(\chi)d\chi = \underbrace{\int_0^{\chi_d} \alpha\beta X_\lambda(\chi)X_{\lambda'}(\chi)d\chi}_{I_1} + \underbrace{\int_{\chi_d}^\infty X_\lambda(\chi)X_{\lambda'}(\chi)d\chi}_{I_2} \tag{127}$$

$$\begin{aligned} I_1 &= \int_0^{\chi_d} \alpha\beta a(\lambda)a(\lambda')\cos\lambda\chi\cos\lambda'\chi\, d\chi = \\ &= \frac{\alpha\beta a(\lambda)a(\lambda')\left[(\lambda-\lambda')\sin\left((\lambda+\lambda')\chi_d\right) + (\lambda+\lambda')\sin\left((\lambda-\lambda')\chi_d\right)\right]}{2(\lambda-\lambda')(\lambda+\lambda')} \end{aligned} \tag{128}$$

$$\begin{aligned} I_2 &= \int_{\chi_d}^\infty (c(\lambda)\cos\lambda\chi + d(\lambda)\sin\lambda\chi)(c(\lambda')\cos\lambda'\chi + d(\lambda')\sin\lambda'\chi)\, d\chi = \\ &= D(\lambda)D(\lambda')\int_{\chi_d}^\infty (\cos\phi\cos\lambda\chi + \sin\phi\sin\lambda\chi)(\cos\phi'\cos\lambda'\chi + \\ &+ \sin\phi'\sin\lambda'\chi)d\chi = \\ &= D(\lambda)D(\lambda')\int_{\chi_d}^\infty \cos(\lambda\chi - \phi)\cos(\lambda'\chi - \phi')\, d\chi = \\ &= \frac{D(\lambda)D(\lambda')}{2}\int_{\chi_d}^\infty \left[\cos\left((\lambda+\lambda')\chi - (\phi+\phi')\right) + \right. \\ &\left. + \cos\left((\lambda-\lambda')\chi - (\phi-\phi')\right)\right] d\chi \end{aligned} \tag{129}$$

where $D(\lambda) = \sqrt{c^2(\lambda) + d^2(\lambda)}$ or $D(\lambda) = a(\lambda)\sqrt{\alpha^2 \sin^2\lambda\chi_d + \beta^2\cos^2\lambda\chi_d}$ if we apply relations (126) and $\phi = \arctg(c(\lambda)/d(\lambda))$.

$$\begin{aligned} I_2 = \left[\pi\delta(\lambda+\lambda') + \pi\delta(\lambda-\lambda') - \frac{\sin\left((\lambda+\lambda')\chi_d - (\phi+\phi')\right)}{\lambda+\lambda'} - \right. \\ \left. - \frac{\sin\left((\lambda-\lambda')\chi_d - (\phi-\phi')\right)}{\lambda-\lambda'}\right] \cdot \frac{D(\lambda)D(\lambda')}{2} \end{aligned} \tag{130}$$

After heavy simplifications we obtain

$$I = I_1 + I_2 = D(\lambda)D(\lambda')\frac{\pi}{2}\Big(\delta(\lambda + \lambda') + \delta(\lambda - \lambda')\Big)$$

which results in $a(\lambda) = 1/\sqrt{\alpha^2 \sin^2\chi_d + \beta^2 \cos^2\chi_d}$.

References

[1] D. Bodansky, *Nuclear energy: principles, practices, and prospects*, 2nd ed. Springer, 2004.

[2] M. P. Unterweger, D. D. Hoppes, F. J. Schima, and J. S. Coursey, "Radionuclide half-life measurements," 2003. [Online]. Available: http://www.nist.gov/pml/data/halflife.cfm.

[3] S. Ono, M. Haginuma, M. Kumagai, M. Kitamura, K. Tachibana, and K. Ishigure, "Distribution of cobalt in surface oxide film of type 304 stainless steel exposed to high-temperature water. Quantitative analysis by glow discharge optical emission spectrometry," *Journal of Nuclear Science and Technology*, vol. 32, no. 2, pp. 125–132, 1995.

[4] K. Varga, G. Hirschberg, Z. Németh, G. Myburg, J. Schunk, and P. Tilky, "Accumulation of radioactive corrosion products on steel surfaces of VVER-type nuclear reactors. Part II. 60Co," *Journal of Nuclear Materials*, vol. 298, no. 3, pp. 231–238, 2001.

[5] K. Varga et al., "Comprehensive investigation of the corrosion state of the heat exchanger tubes of steam generators. Part I. General corrosion state and morphology," *Journal of Nuclear Materials*, vol. 348, no. 1–2, pp. 181–190, 2006.

[6] Z. Homonnay et al., "Comprehensive investigation of the corrosion state of the heat exchanger tubes of steam generators. Part II. Chemical composition and structure of tube surfaces," *Journal of Nuclear Materials*, vol. 348, no. 1–2, pp. 191–204, 2006.

[7] J. Severa and J. Bár, *Handbook of radioactive contamination and decontamination*. Elsevier, 1991.

[8] Y. Takeda, T. Shoji, M. Bojinov, P. Kinnunen, and T. Saario, "In situ and ex situ characterisation of oxide films formed on strained stainless steel surfaces in high-temperature water," *Applied Surface Science*, vol. 252, no. 24, pp. 8580–8588, 2006.

[9] V. Malinovschi, C. Ducu, N. Aldea, and M. Fulger, "Study of carbon steel corrosion layer by X-ray diffraction and absorption methods," *Journal of Nuclear Materials*, vol. 352, no. 1–3, pp. 107–115, 2006.

[10] C. Dame, C. Fritz, O. Pitois, and S. Faure, "Relations between physicochemical properties and instability of decontamination foams," *Colloids and Surfaces A: Physicochemical and Engineering Aspects*, vol. 263, no. 1-3, pp. 210-218, Jan. 2005.

[11] C. Dame, "Étude des relations entre la stabilité des mousses de décontamination nucléaire et leurs propriétés physico-chimiques," Université des sciences et techniaues, Aix-Marseille III, 2006.

[12] Y. Kameo, M. Nakashima, and T. Hirabayashi, "New laser decontamination technique for radioactively contaminated metal surfaces using acid-bearing sodium silicate gel," *Journal of Nuclear Science and Technology*, vol. 41, no. 9, pp. 919–924, 2004.

[13] "Decontamination techniques used in decommissioning activities," OECD/NEA, 1707, 1999.

[14] D. Bäuerle, *Laser processing and chemistry*, 3rd ed. Springer, 2000.

[15] D. A. Cremers and L. J. Radziemski, *Handbook of laser-induced breakdown spectroscopy*. The Atrium, Southern Gate, Chichester, West Sussex PO19 8SQ, England: John Wiley & Sons, 2006.

[16] X. Mao and R. E. Russo, "Observation of plasma shielding by measuring transmitted

and reflected laser pulse temporal profiles," *Applied Physics A: Materials Science & Processing*, vol. 64, no. 1, pp. 1-6, Dec. 1996.

[17] N. M. Bulgakova and A. V. Bulgakov, "Pulsed laser ablation of solids: transition from normal vaporization to phase explosion," *Applied Physics A: Materials Science & Processing*, vol. 73, no. 2, pp. 199–208, 2001.

[18] M. L. Sentis, P. Delaporte, W. Marine, and O. Uteza, "Surface oxide removal by a XeCl laser for decontamination," *Quantum Electronics*, vol. 30, no. 6, pp. 495–500, 2000.

[19] B. Rémy, "Bilan des essais de qualification en inactif du bras de décontamination par laser excimère," DPE/SPEA/SPS, CEA, Note technique 96-010, Juin 1996.

[20] M. C. Edelson, H.-M. Pang, and R. L. Ferguson, "A laser-based solution to industrial decontamination problems," in *Proceedings of ICALEO '95 conference*, San Diego, 1995, vol. 80, pp. 768–777.

[21] R. L. Ferguson, M. C. Edelson, and H.-M. Pang, "Laser ablation system, and method of decontaminating surfaces," U.S. Patent 578080614-Jul-1998.

[22] A. Dupont, "Ablation de couches superficielles de matériaux métalliques par rayonnement laser impulsionnel," L'Universite d'Aix-Marseille II, 1994.

[23] A. Dupont, P. Caminat, P. Bournot, and J. P. Gauchon, "Enhancement of material ablation using 248, 308, 532, 1064 nm laser pulse with a water film on the treated surface," *Journal of Applied Physics*, vol. 78, no. 3, pp. 2022–2028, 1995.

[24] A. C. Tam, H. K. Park, and C. P. Grigoropoulos, "Laser cleaning of surface contaminants," *Applied Surface Science*, vol. 127–129, pp. 721–725, 1998.

[25] R. Fabbro, J. Fournier, P. Ballard, D. Devaux, and J. Virmont, "Physical study of laser-produced plasma in confined geometry," *Journal of Applied Physics*, vol. 68, no. 2, pp. 775–784, 1990.

[26] D. Devaux, R. Fabbro, L. Tollier, and E. Bartnicki, "Generation of shock waves by laser-induced plasma in confined geometry," *Journal of Applied Physics*, vol. 74, no. 4, pp. 2268–2273, 1993.

[27] L. Berthe, R. Fabbro, P. Peyre, L. Tollier, and E. Bartnicki, "Shock waves from a water-confined laser-generated plasma," *Journal of Applied Physics*, vol. 82, no. 6, pp. 2826–2832, 1997.

[28] L. Berthe, R. Fabbro, P. Peyre, and E. Bartnicki, "Wavelength dependent of laser shock-wave generation in the water-confinement regime," *Journal of Applied Physics*, vol. 85, no. 11, pp. 7552–7555, 1999.

[29] H. W. Kang and A. J. Welch, "Effect of liquid thickness on laser ablation efficiency," *Journal of Applied Physics*, vol. 101, no. 8, p. 083101, 2007.

[30] A. Kruusing, "Underwater and water-assisted laser processing: Part 1 — General features, steam cleaning and shock processing," *Optics and Lasers in Engineering*, vol. 41, no. 2, pp. 307–327, 2004.

[31] A. Kruusing, "Underwater and water-assisted laser processing: Part 2 — Etching, cutting and rarely used methods," *Optics and Lasers in Engineering*, vol. 41, no. 2, pp. 329–352, 2004.

[32] M. L. Sentis, P. Delaporte, W. Marine, and O. Uteza, "Excimer laser decontamination," in *International conference on atomic and molecular pulsed lasers III*, Tomsk, Russia, 2000, vol. 4071, pp. 196–208.

[33] P. Delaporte et al., "Radioactive oxide removal by XeCl laser," *Applied Surface Science*, vol. 197–198, pp. 826–830, 2002.

[34] P. Delaporte et al., “Dry excimer laser cleaning applied to nuclear decontamination,” *Applied Surface Science*, vol. 208–209, pp. 298–305, 2003.

[35] V. F. Sheremetov, V. P. Polivko, and et al., “Experimental investigation on feasibility in deactivation of radioactive contaminated metal surfaces by laser radiation,” in *XI Conference on Laser Optics*, St-Petersberg, 2003.

[36] V. F. Sheremetov et al., “Experimental investigations of the possibility of laser decontamination of contaminated metal surfaces emerged in a liquid,” *Laser-Inform*, no. 9, pp. 8–12, 2004.

[37] E. M. Glagovky et al., “Experimental investigations of the possibility of laser decontamination of contaminated metal surfaces,” *Laser-Inform*, vol. 9–10 (240–241), pp. 5–8, 2002.

[38] V. P. Veiko, E. A. Shakhno, V. N. Smirnov, G. D. Nikishin, and S. P. Rho, “Laser ablation and local deposition: physical mechanisms and application for decontamination of radioactive surfaces,” *Journal of the Korean Physical Society*, vol. 51, no. 1, pp. 345–351, 2007.

[39] D. E. Roberts and T. S. Modise, “Laser removal of loose uranium compound contamination from metal surfaces,” *Applied Surface Science*, vol. 253, no. 12, pp. 5258–5267, 2007.

[40] H. J. Won, C. J. Jeong, J. K. Moon, and C. H. Jung, “Feasibility tests of laser decontamination techniques on the metal specimens,” in *The Autumn Meeting of Korea Radioactive Waste Society*, Busan, Korea, 2007, vol. 5, pp. 21–22.

[41] S. Fomichev, A. Semerok, J.-M. Weulersse, and F. Brygo, “Modelling of complex surface heating by continuous and pulsed lasers,” DPC/SCP/LILM, CEA Saclay, NT 05-109-A, Jan. 2005.

[42] H. S. Carslaw and J. C. Jaeger, *Conduction of heat in solids*, 2nd ed. Oxford University Press, 1986.

[43] M. Vicanek, A. Rosch, F. Piron, and G. Simon, “Thermal deformation of a solid surface under laser irradiation,” *Applied Physics A: Solids and Surfaces*, vol. 59, no. 4, pp. 407–412, 1994.

[44] V. V. Apollonov, A. I. Barchukov, N. V. Karlov, A. M. Prokhorov, and É. M. Shefter, “Thermal action of high-power laser radiation on the surface of a solid,” *Soviet Journal of Quantum Electronics*, vol. 5, no. 2, pp. 216–221, 1975.

[45] I. N. Bronshtein, K. A. Semendyayev, G. Musiol, and H. Muehlig, *Handbook of mathematics*, 5th ed. Springer, 2007.

[46] M. Sparks and J. Loh, “Temperature dependence of absorptance in laser damage of metallic mirrors: I. Melting,” *Journal of the Optical Society of America*, vol. 69, no. 6, pp. 847–858, 1979.

[47] B. T. Barnes, “Optical constants of incandescent refractory metals,” *Journal of the Optical Society of America*, vol. 56, no. 11, pp. 1546–1549, 1966.

[48] C. Ronchi, J. P. Hiernaut, and G. J. Hyland, “Emissivity X points in solid and liquid refractory transition metals,” *Metrologia*, vol. 29, no. 4, p. 261, 1992.

[49] P. Herve and A. Sadou, “Determination of the complex index of refractory metals at high temperatures: Application to the determination of thermo-optical properties,” *Infrared Physics & Technology*, vol. 51, no. 3, pp. 249–255, 2008.

[50] C. S. Lee, N. Koumvakalis, and M. Bass, “A theoretical model for multiple-pulse laser-induced damage to metal mirrors,” *Journal of Applied Physics*, vol. 54, no. 10, pp. 5727–5731, 1983.

[51] Y. Jee, M. F. Becker, and R. M. Walser, "Laser-induced damage on single-crystal metal surfaces," *Journal of the Optical Society of America B*, vol. 5, no. 3, pp. 648–659, 1988.

[52] H. M. Musal, "Thermomechanical stress degradation of metal mirror surfaces under pulsed-laser irradiation," in *Laser Induced Damage in Optical Materials*, 1979, vol. 568, pp. 159–173.

[53] M. F. Becker, C. Ma, and R. M. Walser, "Predicting multipulse laser-induced failure for molybdenum metal mirrors," *Applied Optics*, vol. 30, no. 36, pp. 5239–5246, 1991.

[54] A. Gorshkov, I. Bel'bas, V. Sannikov, and K. Vukolov, "Frequency laser damage of Mo mirrors," *Fusion Engineering and Design*, vol. 66–68, pp. 865–869, 2003.

[55] A. Semerok, S. V. Fomichev, J.-M. Weulersse, F. Brygo, P.-Y. Thro, and C. Grisolia, "Heating and ablation of tokamak graphite by pulsed nanosecond Nd-YAG lasers," *Journal of Applied Physics*, vol. 101, no. 8, p. 084916, 2007.

[56] S. Fomichev and A. Semerok, "Étude des processus thermiques survenant lors de la microanalyse des surfaces par la méthode Raman," CEA, DPC/SCPA, NT 02-053, Dec. 2002.

[57] A. D. Polyanin, *Handbook of linear partial differential equations for engineers and scientists*. Chapman & Hall/CRC, 2001.

[58] A. D. Polyanin and V. F. Zaitsev, *Handbook of nonlinear partial differential equations*. Chapman & Hall/CRC, 2003.

[59] A. D. Polyanin and V. F. Zaitsev, *Handbook of exact solutions for ordinary differential equations*, 2nd ed. Chapman & Hall/CRC, 2002.

[60] A. Ishimaru, "Wave propagation and scattering in random media and rough surfaces," *Proceedings of the IEEE*, vol. 79, no. 10, pp. 1359–1366, 1991.

[61] B. Maheu, J. N. Letoulouzan, and G. Gouesbet, "Four-flux models to solve the scattering transfer equation in terms of Lorenz-Mie parameters," *Applied Optics*, vol. 23, no. 19, pp. 3353–3362, 1984.

[62] P. S. Mudgett and L. W. Richards, "Multiple scattering calculations for technology," *Applied Optics*, vol. 10, no. 7, pp. 1485–1502, 1971.

[63] W. E. Vargas, "Generalized four-flux radiative transfer model," *Applied Optics*, vol. 37, no. 13, pp. 2615–2623, 1998.

[64] F. Brygo, "Étude de l'interaction laser-matière appliquée à la décontamination de peinture," Université de Bourgogne, 2005.

[65] F. Brygo, A. Semerok, J.-M. Weulersse, P.-Y. Thro, and R. Oltra, "Laser ablation of a turbid medium: Modeling and experimental results," *Journal of Applied Physics*, vol. 100, no. 3, p. 033106, 2006.

[66] L. D. Landau, E. M. Lifshitz, and L. P. Pitaevskii, *Electrodynamics of continuous media*, 2nd ed., vol. 8. Butterworth-Heinemann, 1984.

[67] J. J. Monzón and L. L. Sánchez-Soto, "On the definition of absorption for a Fabry-Perot interferometer," *Pure and Applied Optics: Journal of the European Optical Society Part A*, vol. 1, no. 4, pp. 219–226, 1992.

[68] V. V. Sobolev, *A treatise on radiative transfer*. Princeton: D. Van Nostrand Company, 1963.

[69] G. Kortüm, *Reflectance spectroscopy*. New York: Springer, 1969.

[70] M. Galassi, *GNU Scientific Library*. 2010.

[71] E. Hairer, S. P. Nørsett, and G. Wanner, *Solving ordinary differential equations I:*

Nonstiff problems, 2nd ed., vol. 1, 2 vols. Springer, 2008.

[72] M. A. Dupertuis, M. Proctor, and B. Acklin, "Generalization of complex Snell-Descartes and Fresnel laws," *Journal of the Optical Society of America A*, vol. 11, no. 3, pp. 1159–1166, 1994.

[73] H. Maezawa and H. Miyauchi, "Rigorous expressions for the Fresnel equations at interfaces between absorbing media," *Journal of the Optical Society of America A*, vol. 26, no. 2, pp. 330–336, 2009.

[74] A. Gershun, "Fresnel reflection of diffusely incident light," *Journal of the Optical Society of America*, vol. 35, no. 2, pp. 162–163, 1945.

[75] J. W. T. Walsh, "The reflection factor of a polished glass surface for diffused light," *Illumination Research Technical paper*, vol. 2, p. 10, 1926.

[76] J. W. Ryde, "The scattering of light by turbid media. Part I," *Proceedings of the Royal Society of London. Series A*, vol. 131, no. 817, pp. 451–464, 1931.

[77] S. Q. Duntley, "The optical properties of diffusing materials," *Journal of the Optical Society of America*, vol. 32, no. 2, p. 61, Feb. 1942.

[78] W. A. Allen, "Transmission of isotropic light across a dielectric surface in two and three dimensions," *Journal of the Optical Society of America*, vol. 63, no. 6, pp. 664–666, 1973.

[79] F. Stern, "Transmission of isotropic radiation across an interface between two dielectrics," *Applied Optics*, vol. 3, no. 1, pp. 111–113, 1964.

[80] M. Born and E. Wolf, *Principles of optics*, 7th ed. Cambridge University Press, 1999.

[81] G. Hernandez, "Fabry-Perot with an absorbing etalon cavity," *Applied Optics*, vol. 25, no. 18, pp. 3062–3067, 1985.

[82] A. B. Murphy, "Modified Kubelka–Munk model for calculation of the reflectance of coatings with optically-rough surfaces," *Journal of Physics D: Applied Physics*, vol. 39, no. 16, pp. 3571–3581, 2006.

[83] P. Hariharan, *Optical interferometry*, 2nd ed. San Diego, USA: Academic Press, 2003.

[84] D. Nečas and P. Klapetek, *Gwyddion*. 2011.

[85] J. M. Liu, "Simple technique for measurements of pulsed Gaussian-beam spot sizes," *Optics Letters*, vol. 7, no. 5, pp. 196-198, 1982.

[86] E. Hecht, *Optics*, 4th ed. Addison Wesley, 2002.

[87] W. Pacquentin, "Contribution à l'étude des propriétés physico-chimiques des surfaces modifiées par traitement laser. Application à l'amélioration de la résistance à la corrosion localisée des aciers inoxydables," Ph.D. thesis, Université de Bourgogne, 2011.

[88] D. Murdoch, I.-R. Cristescu, and R. Lässer, "Strategy for determination of ITER in-vessel tritium inventory," *Fusion Engineering and Design*, vol. 75–79, pp. 667–671, 2005.

[89] T. Acsente et al., "Properties of composite a-C:H/metal layers deposited by combined RF PECVD/magnetron sputtering techniques," *Thin Solid Films*, vol. 519, no. 12, pp. 4054-4058, Apr. 2011.

[90] D. Melyukov, C. Sortais, A. Semerok, P.-Y. Thro, and X. Courtois, "Lock-in laser pyrometry for surface characterisation," DPC/SCP/LILM, CEA Saclay, NT 10-386-A, 2010.

[91] I. S. Grigoriev and E. S. Meilikhov, Eds., *Physical quantities: Handbook*. Moscow: Energoatomizdat, 1991.

[92] D. R. Lide, Ed., *Handbook of chemistry and physics*, 90th ed. CRC Press / Taylor & Francis, 2010.

[93] E. D. Palik, Ed., *Handbook of optical constants of solids*, vol. 1. Academic Press, 1985.

[94] J. F. Figueira and S. J. Thomas, "Damage thresholds at metal surfaces for short pulse IR lasers," *IEEE Journal of Quantum Electronics*, vol. 18, no. 9, pp. 1381–1386, 1982.

[95] B. W. Veal and A. P. Paulikas, "Optical properties of molybdenum. I. Experiment and Kramers-Kronig analysis," *Physical Review B*, vol. 10, no. 4, pp. 1280–1289, 1974.

[96] K. A. Kress and G. J. Lapeyre, "Optical properties of molybdenum and ruthenium," *Journal of the Optical Society of America*, vol. 60, no. 12, pp. 1681–1684, 1970.

[97] R. S. Patil, M. D. Uplane, and P. S. Patil, "Structural and optical properties of electrodeposited molybdenum oxide thin films," *Applied Surface Science*, vol. 252, no. 23, pp. 8050–8056, 2006.

[98] C. Cagran, G. Pottlacher, M. Rink, and W. Bauer, "Spectral emissivities and emissivity X-points of pure molybdenum and tungsten," *International Journal of Thermophysics*, vol. 26, no. 4, pp. 1001–1015, 2005.

[99] B. Karlsson and C. G. Ribbing, "Optical constants and spectral selectivity of stainless steel and its oxides," *Journal of Applied Physics*, vol. 53, no. 9, pp. 6340–6346, 1982.

[100] Y. B. Unigovski, G. Lothongkum, E. M. Gutman, D. Alush, and R. Cohen, "Low-cycle fatigue behavior of 316L-type stainless steel in chloride solutions," *Corrosion Science*, vol. 51, no. 12, pp. 3014 - 3020, 2009.

[101] E. S. Puchi-Cabrera, M. H. Staia, C. Tovar, and E. A. Ochoa-Pérez, "High cycle fatigue behavior of 316L stainless steel," *International Journal of Fatigue*, vol. 30, no. 12, pp. 2140 - 2146, 2008.

[102] A. Dutta, S. Dhar, and S. K. Acharyya, "Material characterization of SS 316 in low-cycle fatigue loading," *Journal of Materials Science*, vol. 45, no. 7, pp. 1782–1789, 2010.

[103] V. P. Glushko, Ed., *Thermodinamical properties of individual substances*, 3rd ed., vol. 4, 4 vols. Moscow: Nauka, 1982.